Reconstruction of electromagnetic fields with Quasinormal Modes : a numerical approach

Alexandre Gras

THÈSE PRÉSENTÉE

POUR OBTENIR LE GRADE DE

DOCTEUR

DE L'UNIVERSITÉ DE BORDEAUX

ECOLE DOCTORALE SCIENCES PHYSIQUES ET DE L'INGÉNIEUR

Nanophysique, Intéraction matière-rayonnement, Simulation numérique

Par **Alexandre Gras**

Reconstruction of Electromagnetic Fields with Quasinormal Modes: A Numerical Approach

Sous la direction de : **Philippe Lalanne**
Co-directrice : **Hélène Barucq**
Co-encadrant : **Marc Duruflé**

Date de soutenance: Mardi 29 mars 2021
Membres du jury :

M. Xavier Letartre	Directeur de Recherche	Université de Lyon	Rapporteur
M. Emmanuel Centeno	Professeur	Université Clermont Auvergne	Rapporteur
M. André Nicolet	Professeur	Université Aix-Marseille	Président
Mme. Émilie Sakat	Chargée de Recherche	Université Paris-Saclay	Examinatrice
M. Jérôme Cayssol	Professeur	Université de Bordeaux	Examinateur
M. Philippe Lalanne	Directeur de Recherche	LP2N/CNRS	Directeur
M. Marc Duruflé	Maitre de Conférence	INRIA Bordaeux Sud-Ouest	Invité

Abstract

The response of open optical resonators to excitation can be expressed as a superposition of their intrinsic resonances, their quasinormal modes (QNM), which are loaded by the driving field and decay exponentially in time due to power leakage or absorption. Quasinormal modes are the eigensolutions of the time-harmonic Maxwell's equations et complex eigenfrequencies and allow more physical insight to be brought into the analysis of resonator dynamics. However, due to the complexity in modeling the open resonators and computing their modes, numerical tools such as linear eigenmode solvers are frequently called upon. The numerical discretization of the problem and some of the methods used to satisfy boundary conditions manifest themselves in the form of numerical modes that bear no physical meaning but complete the QNM basis and allow it to converge if many modes are included in the expansion. We also verify that the multiple formulas that exist for the auxiliary-field formulation of the QNM expansion have a similar origin and produce the same results. We compute the modes of periodic resonator structures to reconstruct the spectra on a wide spectrum of frequencies. We try to make the expansion converge with the least amount of modes by finding a way to classify them then explore the dependence of the modes on numerical parameters. Finally, we devised a way to obtain convergent results with few modes by interpolating from a few real frequency computations.

La réponse des résonateurs optiques ouverts suite à leur excitation peut se décrire par la superposition de leurs résonances intrinsèques, leurs modes quasinormaux (QNM), qui sont excités par un champ incident et qui s'atténuent exponentiellement dans le temps à cause de fuites d'énergie et l'absorption. Les QNMs sont les vecteurs propres des équations de Maxwell harmoniques et permettent d'obtenir plus d'informations sur la dynamique du résonateur. Cependant, la complexité de la modélisation des résonateurs et du calcul des modes amènent à l'utilisation d'outils numériques pour résoudre ces systèmes équations linéaires afin de trouver les modes. La discrétisation du problème et certaines méthodes utilisées pour vérifier les conditions d'onde sortantes se manifestent à travers des modes numériques qui complètent la base des QNMs et qui permettent à la superposition de modes de converger si un grand nombre de modes, physiques et numériques, sont pris en compte. Nous vérifions que les formules qui existent pour la méthode des champs auxiliaires appliquée aux QNMs ont une origine commune et produisent des résultats similaires. Nous calculons les modes de structures périodiques afin de reconstruire le champs sur un spectre fréquentiel large. Nous essayons de faire converger la superposition des QNMs en trouvant un moyen de classifier les modes et explorons ensuite la dépendance des modes à certains paramètres numériques. Nous faisons converger la reconstruction modale du champ avec peu de modes en interpolant.

Declarations

This work was funded by the Agence de l'Innovation de Défense (DGA), the Agence Nationale de la Recherche (ANR) project **Résonance** (ANR-16-CE24-0013), and the Institut national de recherche en informatique et en automatique (INRIA).

Ces travaux de thèse ont été financés par l'Agence de l'Innovation de Défense (DGA), le projet de l'Agence Nationale de Recherche (ANR) **Résonance** (ANR-16-CE24-0013), et l'institut national de recherche en informatique et en automatique (INRIA).

Contents

Chapter 1

Introduction

Light has long since fascinated mankind. From the past devout worship of the sun to the presence of light in religious iconography, light and its sources have been given a divine and mysterious aura throughout the eras. As scientists began to unearth the nature of light, from its wave characteristics hinted by interference phenomena to later discovering its particular make-up, man has harnessed it to better his life. The advances made in the 19th and 20th century have brought light-harnessing appliances to the streets to our homes, and nowadays to our pockets for our better comfort. Like it shines the way forward on the roads on an obscure night, our increased understanding and control of optics has paved the way for many essential innovations in the 20th century. And in a most unexpected twist, the control of light can be achieved at scales far smaller than the deities it inspired.

Optical micro- and nanoresonators have provided this control over the interaction between light and matter. Their proliferation during the past few decades is due to the development of bottom-up [1, 2] and top-down [3, 4] nanofabrication techniques and technologies, permitting the construction of structures of varying shapes, materials, and sizes [5, 6, 7]. Optical resonators play centerpiece roles in many blossoming fields in nanophotonics, such as optical sensing [8, 9], metamaterials[10, 11] and integrated photonic circuits [12, 13]. Nanophotonics has flourished with these items, which have allowed the manipulation and greater understanding of light at the nanometric scales [14]. Examples of different fabricated micro- and nano-sized optical resonators are displayed in Fig. 1.1.

1.1 Photonic Resonators

Optical resonators are structures whose optical responses are exalted at certain frequencies of light. Emitters placed around or inside these structures see their emission increase greatly due to the confinement of light in space and across time. The Purcell Factor [15] is one phenomenon that causes the spontaneous emission rate of an emitter in the cavity to be enhanced. The value of the enhancement is largely dependent on the ability of the resonator to store energy while leaking as little as possible and its ability to confine light to very small volumes. This is usually quantified by the ratio Q/V, where Q is the quality factor of the resonator at its resonance frequency, and V the mode volume.

The quality factor Q of a resonator characterizes a resonator's bandwidth relative to its resonance frequency. It describes a resonator's ability to store energy relative to how much energy it leaks over time. These characteristics of optical resonators are also found in other domains, such as acoustics. A tuning fork will usually ring out with a clear note for several seconds after receiving a single strike. This takes the form of damped oscillation at a single frequency, the note of the tuning fork, usually between 100 Hz and 4 kHz. Upon absorbing the energy from the strike, it releases that energy by vibrating, at first widely because different high-frequency vibrations are overlapping, until the dominant oscillation remains and the energy leaks out through this particular mode of acoustic vibration. The fork will oscillate at this frequency Q times before most of the energy is depleted, that duration corresponding to the mode's lifetime τ. The value of Q can possibly reach a couple thousand depending on the fabrication and the material the tuning fork is made from. For a resonator mainly oscillating at the angular frequency Ω, the quality factor can be defined as follows with energy considerations:

$$Q = \Omega \frac{\tau}{2\pi}. \tag{1.1}$$

The mode volume V describes the spatial distribution of the energy the system has received and released. It is a measure of the confinement of the energy, a quantification of the physical volume within which the energy is mostly directed, where the oscillations are the strongest. In the case of the tuning fork, it would correspond to the area in space where a microphone would pick up the most signal, where the air that creates the sound gets displaced with the most intensity, relative to how the signal is distributed by the fork over all of space. This would be near the tips of the tuning fork, far from the base where the acoustic signal is weaker.

These properties of resonant systems give an idea about their characteristics and how they can be used. In the case of the tuning fork, it gives us insight on where to strike it to get the loudest sound, how long the ringing will last, and where one should place their ear to listen to the sound. The same principles apply to devices made out of optical resonators. The quality factor being a measure of the dissipation of energy, low-Q devices could be used for their small response times, because the amplitude of the field would drastically decrease after a few oscillations. Resonators with small mode volumes V means that the field is focused in small areas meaning that a well-constructed optical resonator could be used to detect small objects. The exploitation of these properties allows for myriad applications.

When the frequency of the excitation matches up with the resonant frequency of the resonator, the amplitude of the oscillations of the electric field increases dramatically. In that instance, the energy that the resonator has taken is mostly released in a single mode of oscillation. These modes are intrinsic to the resonator, and play an essential role in the resonator response dynamics. The design of devices around the compatibility of a light source with specific modes is an effective design philosophy for resonator applications.

And similarly to a tuning fork, the shape of optical resonators and the materials that compose them determine their resonant performance. From this, two clear paradigms appear, for one, cavities made of low-loss materials that are able

to store light efficiently, and plasmonic materials made of absorbing materials but which are able to confine light in small volumes. Examples of the two types of resonances are shown in Fig. 1.2.

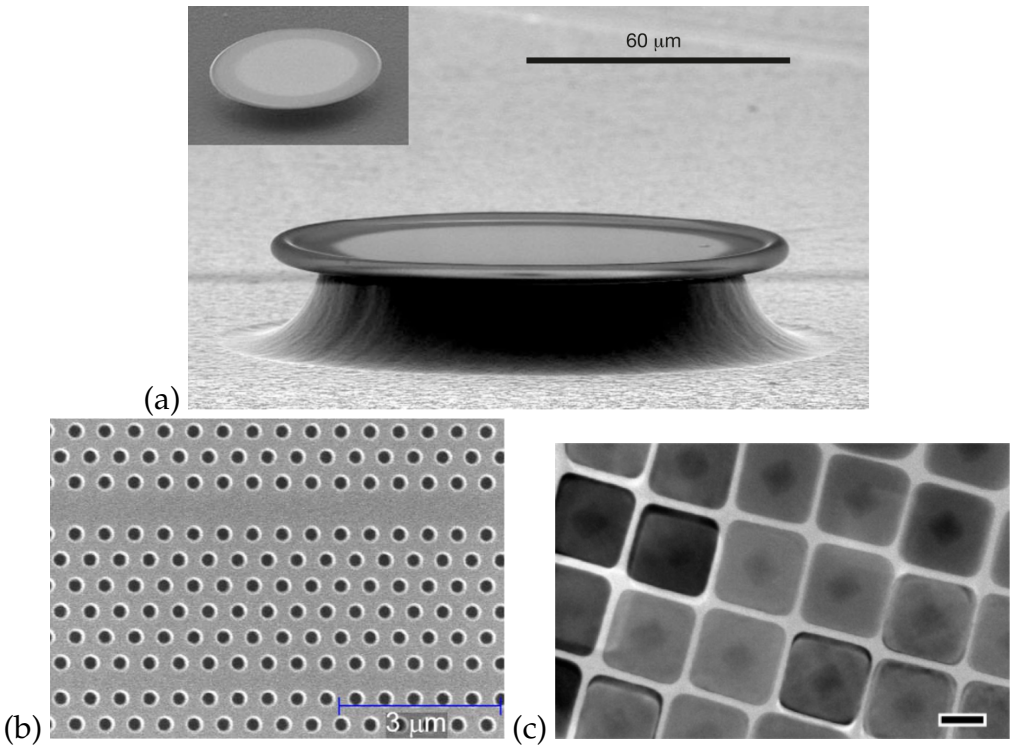

Figure 1.1: (a) SEM image of a silica microdisk. Reprinted with permission from Springer Nature "Ultra-high-Q toroid microcavity on a chip" by D. K. Armani et al [5], © Springer 2003. (b) SEM image of a Photonic Crystal waveguide. Reprinted with permission from [6], © The Optical Society. (c) TEM image of 35 nm size nanocubes. The scale bar is 20 nm. Reprinted with permission from [7]. © American Chemical Society 2014 .

1.1.1 Dielectric Cavities

A subset of optical micro-resonators are cavities made of materials with very low levels of absorption within a frequency range. These dielectric materials have very little dissipation causing the quality factors of these cavities to be relatively high (ranging from 10^3 to 10^9). In these cavities, the light usually bounces back and forth from one end of the cavity to the other. The resonance condition is met when a whole number of oscillations occur between both edges of the cavity. This means that the field is confined in a volume usually in the order of several to hundreds of λ^3. A simple example of this is the Fabry-Pérot cavity, made of two parallel reflecting interfaces. This cavity has been used in many devices like interferometers and early laser technology. Other types of cavities have been used for diverse purposes. Microdisk-type or toroid-type cavities like the one pictured in Fig. 1.1a have been used for sensing applications [16, 17] due to their incredibly sharp resonant peaks which causes great sensitivity to local permittivity perturbations depending on the mode, which can be enhanced when a mode is excited under specific conditions [17]. The drawback of this incredible

sensitivity is the difficulty to finely tune the cavity resonance to a specific wavelength, due to extreme sensitivity to fluctuations [18]. In these micro-disk cavities, the light circulates on the outer border of the disk due to total internal reflection at the interface with air. These types of oscillations are called whispering-gallery modes, explaining the sensitivity of the microdisks to perturbation places in these areas. Photonic crystal cavities as pictured in Fig. 1.1b are created when "defects" are introduced in otherwise periodic structures like photonic crystal waveguides. These types of resonators also make great for great sensors due to their high-Q resonances [19] and also have seen use in slow light experiments [20].

In most of these devices, the field oscillates with great amplitude within the cavity, and coupling an emitter to a cavity mode by placing it in the "hot spots" inside the cavity leads to an increase in the spontaneous emission rate of the emitter. The interaction between the cavity mode and the emitter can be harnessed to control the emission of the atom, leading to practical applications, like quantum information processing [21]. Accurately computing the characteristics of the modes of the cavity, such as their lifetimes, their resonant frequency, and their field, are essential to the design of devices using cavities. This allows the choice and placement of the emitter to be optimized to the qualities of the cavity. The properties of the cavity modes are thus of great interest.

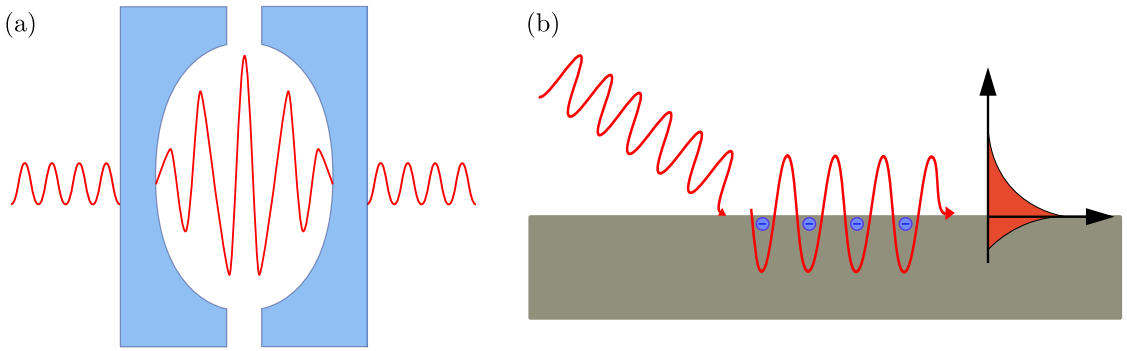

Figure 1.2: (a) Cavity type resonator where the field oscillates back and forth and is localized inside the cavity and leaks very little to the outside. (b) The incident wave creates an oscillation of electrons and an electromagnetic field at the surface of a metal-dielectric interface, the surface plasmon. The incident field can couple very efficiently with the surface plasmon at particular frequencies.

1.1.2 Plasmonic Resonators

Plasmonic resonators are made of metals, whose electromagnetic radiation is dependent on the behavior of the free conduction electrons on the surface of the metal [22]. The collective oscillations of electrons at the surface of the metal due to the excitation from a driving field induces the hybridization of light and electron oscillation into what is called a "surface plasmon polariton".The resulting electromagnetic field is heavily confined to the surface of the metal, at subwavelength depths below the diffraction limit ($l < \lambda/2\pi$). While plasmonic modes are tightly confined at the surfaces of the metal, which then leads into a small mode volume for plasmonic resonators $V \sim 10^{-4}\lambda^3$, due to the absorption from

their material properties, the quality factor of plasmonic resonators is rather low $Q \sim 20$. Plasmonic modes are confined to the metal-air interface, their observation in the far field requires the use of near-field probes to convert the evanescent field to one that propagates away from the plasmonic resonator [22]. This is usually done with the use of prisms [23] or gratings [24]. Plasmonic nanoparticles have also proliferated due to the discoveries related to their fabrication.

Plasmonic nanoparticles have many applications. Biosensing is a domain in which they are present [25, 23], finding practical use in sensing applications such as pregnancy tests [26] and some cancer therapies [27]. Ensembles of plasmonic nanoparticles also make for practical optical antennas because their arrangement can be tailored to obtain specific anisotropic light scattering patterns [28]. Plasmonic particles are used in metamaterials due to their interesting optical properties [10].

Devices using plasmonic particles are able to confine light precisely but in turn, suffer detrimental dissipative loss and due to the low Qs, the spectral resonances are wide and may overlap. However, due to the high dissipation, the response time of plasmonic resonators to a pulse for example is near instantaneous, in the range of tens of femtoseconds [29] when excited with femtosecond pulses. This is in clear contrast to dielectric resonators where the light is preserved inside the cavity in much longer time scales.

Finding the characteristics of the modes of plasmonic structures, such as their lifetime and the field distribution, is key to building efficient devices. Finding how the resonators scatter light into space can influence design decisions on optical devices, like how much energy is lost from leakage or absorption depending on the type of excitation, and how to maximize the coupling of one resonator's modes from a particular source.

1.1.3 Resonator Analysis

We can approximate the resonance frequency and the field of the modes of a resonator by analyzing its spectral response to an excitation. We will assume the $\exp(-i\omega t)$ convention for time-harmonic fields for this chapter. This conventtion will change during the thesis The resonator, described by the permittivity distribution $\varepsilon(\mathbf{r}, \omega)$, is placed within a background medium $\varepsilon_b(r, \omega)$, where ω is the angular frequency of the excitation. A driving field $[\mathbf{E}_d(\mathbf{r}, \omega), \mathbf{H}_d(\mathbf{r}, \omega)]$, satisfying the curl Maxwell's equations in the background medium acts as an excitation interacting with the resonator. In the scattering formulation, we can write the time-harmonic Maxwell's equations for the field scattered by the resonator:

$$\begin{cases} \nabla \times \mathbf{H}_s(\mathbf{r}, \omega) + i\omega\varepsilon(\mathbf{r}, \omega)\mathbf{E}_s(\mathbf{r}, \omega) = i\omega(\varepsilon(\mathbf{r}, \omega) - \varepsilon_b)\mathbf{E}_d(\mathbf{r}, \omega), \\ \nabla \times \mathbf{E}_s(\mathbf{r}, \omega) - i\omega\mu\mathbf{H}_s(\mathbf{r}, \omega) = 0, \\ + \text{outgoing-wave boundary conditions}, \end{cases} \tag{1.2}$$

where the source term is localized in the region in space where $(\varepsilon(\mathbf{r}, \omega) - \varepsilon_b)$ is non-null, which usually corresponds to the resonator's location. The outgoing-wave conditions mean that we consider the domain to be open, allowing the resonator's scattered field to leak into free space where $|\mathbf{r}| \to \infty$. Depending on the characteristics of the driving field, the spectral response of the resonator $f(\omega)$

may present resonant peaks, as pictured in the top panel of Fig. 1.3, indicating the excitation of the modes of the resonator. The resonant linewidth $\Delta\omega$ of the peaks are inversely proportional to the mode's lifetime and the resonant frequency Ω corresponds to the frequency for which the response $f(\omega)$ peaks. The field corresponding to the mode would be somewhat approximated by the value of the scattered field at the frequency Ω, if we were to consider that, at resonance, the scattered field is mostly represented by the resonant mode.

In order to find the resonant frequency and the field of the mode, numerical tools to solve Maxwell's equations and compute the scattered field at real frequencies can be used. Most of these tools require the definition of the frequency and polarization of the driving field $\mathbf{E}_d(\mathbf{r}, \omega)$ that will excite the resonator, in order to compute the scattered field which, at resonance, should be expectedly quite similar to the mode in question. However, resolving a spectrally narrow resonant peak would require scanning the frequency spectrum with a very small frequency step, which would require many computations. Unearthing the spectral properties of a resonator over a wide spectral range would require a great number of computations. Additionally, a given polarization of the driving field might not excite a particular mode of interest so the computations might need to be repeated for different polarizations. Finding modes using real frequency computations of the scattered field is thus numerically intensive due to the number of computations needed in order to discern modes on a wide frequency spectrum.

If the resonator response is truly driven by modes, the need for a rigorous formalism which accurately computes and reconstructs the scattering of waves by a resonator via modal contributions becomes essential. In that sense, we need a formalism that directly allows access to the modes of the system and that would compute them directly, without considering any sort of external excitation, since they are intrinsic to the resonator's structure.

The scattered field formulation of Maxwell's equations in Eq. 1.2 is an eigenvalue problem at the frequency ω with a source term. Solving the equations without the source term thus would yield the eigenvectors and eigenvalues of the scattering problem, the modes of the system. This is the principle behind the quasinormal mode (QNM) formalism.

1.2 Quasinormal mode expansion

1.2.1 Definition

Quasinormal modes are the eigenmodes $[\widetilde{\mathbf{E}}_m(\mathbf{r}), \widetilde{\mathbf{H}}_m(\mathbf{r})]$ of the time-harmonic Maxwell's equations of the homogeneous problem associated to Eq. 1.2. They are source-free solutions of Maxwell's equations for the permittivity distribution of the resonator $\varepsilon(\mathbf{r}, \omega)$, at the eigenfrequency $\widetilde{\omega}_m$:

$$\begin{cases} \nabla \times \widetilde{\mathbf{H}}_m(\mathbf{r}) + i\widetilde{\omega}_m \varepsilon(\mathbf{r}, \widetilde{\omega}_m)\widetilde{\mathbf{E}}_m(\mathbf{r}) = 0, \\ \nabla \times \widetilde{\mathbf{E}}_m(\mathbf{r}) - i\widetilde{\omega}_m \mu \widetilde{\mathbf{H}}_m(\mathbf{r}) = 0, \\ + \text{outgoing-wave boundary conditions.} \end{cases} \tag{1.3}$$

The eigenfrequency $\widetilde{\omega}_m = \Omega_m - i\Gamma_m/2$ is complex-valued, the imaginary part Γ_m accounting for the losses via absorption as well as the leakage of the energy

into the free space. The real part of the eigenfrequency corresponds to the resonant frequency while the imaginary part corresponds to the spectral linewidth of the mode, which is related to the mode's temporal lifetime $\tau = \frac{1}{2\mathrm{Im}(\widetilde{\omega}_m)}$. The choice in convention for time-harmonic fields changes the sign of the imaginary part of the eigenfrequency since it always corresponds to the losses incurred over time. Inversely, while the QNM is bound to exponentially decrease with time, the consequence of that is the exponential growth of QNMs in space as $|\mathbf{r}| \to \infty$. Indeed, the spherical outgoing-wave propagating in the far field has the form $\exp[-i\widetilde{\omega}_m(t - r/c)]$, where c is the speed of light. This has led to a difficulty of properly computing and normalizing QNMs, since the computational domain is supposed to be open. This prevents the modes from being normalized like in Hermitian physics, by integrating the mode's electromagnetic energy $\varepsilon \left|\widetilde{E}_m\right|^2 + \mu \left|\widetilde{H}_m\right|$ over a infinitely large domain, since $\left|\widetilde{E}_m(\mathbf{r})\right|$ diverges at $|\mathbf{r}| \to \infty$.

However, by solving Eq. 1.3 for the modes directly, we are able to discern the characteristics of the modes without considering any excitation. The modes are intrinsic to the resonator. Resonator characteristics can be rewritten using the QNM formalism, such as the quality factor. The quality factor of the m^{th} mode of the resonator can be rewritten using its eigenfrequency [14]:

$$Q_m = -\frac{\mathrm{Re}(\widetilde{\omega}_m)}{2\mathrm{Im}(\widetilde{\omega}_m)}. \tag{1.4}$$

The minus sign is due to the $\exp(-i\omega t)$ and the factor two is due to the difference between amplitude and intensity decays. Computing the QNMs directly has major advantages. For one, the spectral properties of the resonator are laid bare: for each resonant peak that one might find in the spectral response $f(\omega)$ as in the top panel of Fig. 1.3, a corresponding mode can be placed in the complex frequency plane. Since we are directly computing the modes, the resonances are accessed without consideration for any kind of excitation impinging upon the resonator.

The modes, once computed, can then be normalized and the scattered field can be expanded on the QNM basis.

1.2.2 Expansion of the scattered field

If the modes are properly normalized, the resonator response or the scattered field of the system can then be described as the superposition of the excited modes:

$$\mathbf{E}_s(\mathbf{r}, \omega) = \sum_m \alpha_m(\omega)\widetilde{\mathbf{E}}_m(\mathbf{r}), \tag{1.5}$$

where α_m is the excitation coefficient of the mode, describing the mode's level of excitation from the driving field. The QNM is a pole of the Maxwell's equations operator described in Eq. 1.2, the resonator response diverges when the complex excitation frequency approaches a mode's complex-valued eigenfrequency $\widetilde{\omega}_m$. The QNMs form a basis, one that can be proven to be orthogonal under certain conditions [14], using the Lorentz Reciprocity theorem [30] for example. For a basic one-dimensional cavity, the expansion has been analytically proven to

be complete inside the cavity, meaning that if we include all potentially existing modes, the expansion will yield an exact reconstruction of the scattered field [31] in the cavity region. This property has also been proven to apply to spheres in three dimensions [31]. For other geometries, including practical more complex ones, the property of completeness has not yet been proven [14] in the case of the continuous physical problem described in Eq. 1.2.

However, this does not mean that the expansion can not be used to accurately approximate the scattered field or the resonator response for these geometries. While the modes of more complicated structures cannot be expressed analytically, they can be computed through numerical methods and the field can be reconstructed, in and out of the resonator domain. With these numerical methods and tools come limitations in the ways we can model these open resonators. The numerical discretization of the continuous eigenvalue problem of Eq. 1.3 directly impacts the computation of modes as well as the reconstruction. The accuracy of the computed modes is affected by the quality of the numerical mesh used to model the resonator. The numerical techniques to model the physics, like the boundary conditions, also alter the modes that are computed by a solver. All these factors influence the quality of the modal reconstruction of the field.

The subject of this work is to gauge how accurately the scattered field can be approximated numerically using the modal expansion, and to determine what can affect the modal reconstruction of the field.

1.2.3 Context and aim of the present work

In this work, the modes will be computed numerically and the scattered field will be reconstructed using a finite number of modes. The continuous operator described in Eq. 1.2 and Eq. 1.3 is originally defined for an unbound space. It is replaced with a discretized operator, a finite-dimensional matrix, defined on a finite mapped space, with new permittivity and permeability distributions to account for the truncation of the computation domain while satisfying the outgoing-wave boundary condition using numerical tools [14]. One of these tools is the use of Perfectly Matched Layers (PMLs) that perform a complex coordinate transform of space as to simulate that the domain extends to infinity. Along with discretization, this causes only a subset of the infinite QNM sets to be accurately approximated and this subset is completed with another finite but substantial set of numerical modes often referred to as PML modes [14, 32, 33, 30, 34, 35], as they originate from the finite-discretized space bounded by PMLs. This method allows the use of the QNM expansion within the spectral range of interest while using modes that are resonant which allows the analysis of resonators with arbitrary shapes, dispersive materials [36, 33, 30, 34, 35], within complex environments [30, 35]. Owing to the finite-dimensional discretized operator, completeness of the scattered-field expansion of Eq. 1.5 is valid everywhere in the computational domain [30].

In the literature, the modal expansion of the field has operated under two paradigms to reconstruct physical quantities. The first in which the expansion is used with few modes, usually under 10, with each mode corresponding to a resonance of the reconstructed quantity [37, 38, 39, 40, 41, 42, 43]. In these cases, QNMs reconstruct the resonant lineshapes with a seemingly "good agreement"

[44, 45] with a computation performed with another method. However, out of the resonant peaks, the agreement between the reference computation and the QNM reconstruction is lessened out of resonance [40].

With the development in the recent years of solvers that find a great number of modes, compared to pole-searching methods [46], or FTDT methods [39], the second paradigm consists in using a great number of modes in the expansion, usually more than a hundred. These tools either employ eigenvalue solvers that use auxiliary fields [30, 47, 42, 48] or nonlinear eigenvalue solvers [34, 49]. It is usually with the exploitation of these tools that the computation of purely numerical modes (sometimes referred to as PML modes) becomes possible. With the use of hundreds of modes and a wide eigenvalue spectrum [30, 34, 50], the convergence is attained to varying degrees of accuracy. In the supplementary information of [30], which could be considered to be at the state of the art, the error of the reconstruction of the extinction cross-section over a large spectrum for complex-shaped, dispersive resonators seems to trend to $10/M^2$, where M is the number of modes in the expansion as shown in the figures SI.5, SI.6 and SI.7. This reconstruction uses both physical modes and numerical PML modes in the expansion. This shows that the field inside the resonator has been reconstructed accurately using both subsets of modes . This convergence speed has been observed in other works on spherical resonators [51].

This present work follows these lines and aims to show what could influence the numerical reconstruction of the field and physical quantities using the modal expansion for different geometries. In that sense, we can rewrite Eq. 1.5 to better represent the numerical reality of the problem:

$$\mathbf{E}_s(\mathbf{r},\omega) \approx \sum_{m}^{M} \alpha_m(\omega)\widetilde{\mathbf{E}}_m(\mathbf{r}). \tag{1.6}$$

The numerical aspect of this work means that we are limited by the computational power of our tools and thus we can only use a finite number M of modes to approximate the value of the field.

In this work, we quantify the impact of different types of modes on the reconstruction of a physical quantity and attempt to gauge how important PML modes are to the reconstruction of the field. We define criteria based on the modes' fields in order to sort the modes out and find the path to a convergent result with the smallest number M of modes in the expansion.

1.3 Outline

Each chapter will explore the viability of the QNM basis in describing the scattered field as a superposition of a finite number of modes.

Chapter 2 will first and foremost introduce the QNM formalism and explore the case study of the Fabry-Pérot cavity, an important example due to the simplicity of structure, allowing for core properties to be demonstrated and its modes to be computed analytically. The cavity will then be simulated with finite elements and we will reconstruct the scattered field with the numerically computed modes.

In Chapter 3, we will consider the case of a resonator whose permittivity is described by an N-pole Lorentz function of the frequency. We propose a gen-

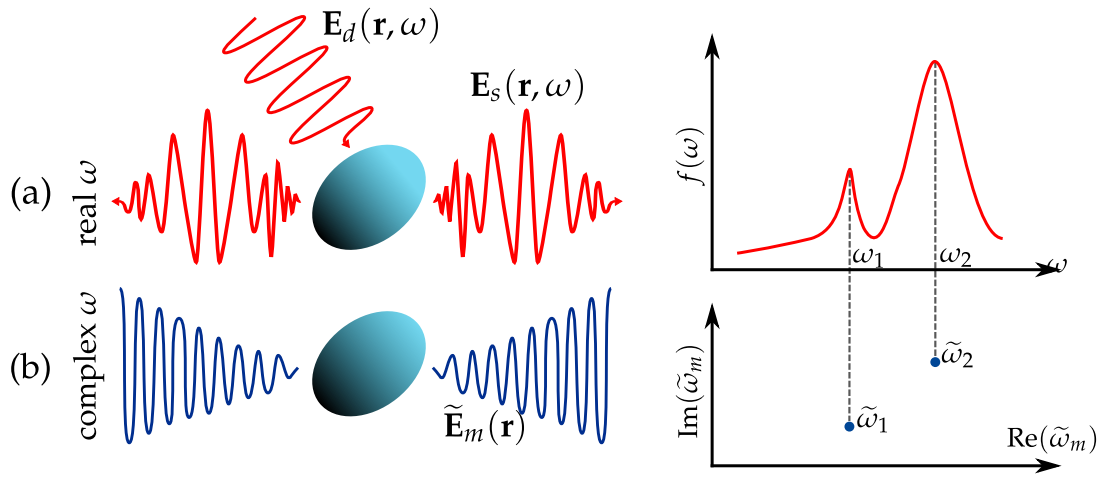

Figure 1.3: Concept of QNM to describe light interaction with resonant systems. (a) Real frequency domain: an incident field $\mathbf{E}_b(\mathbf{r},\omega)$ at real frequency impinges upon an electromagnetic resonator which produces a scattered field $\mathbf{E}_s(\mathbf{r},\omega)$. The spectrum of the optical response, a quantity $f(\omega)$ which could be a scattering or absorption cross section, the Purcell Factor, among other quantities. $f(\omega)$ presents peaks or resonances that may overlap. (b) Complex frequency domain : The electromagnetic resonator possesses several leaky resonances, or Quasinormal modes, each of them being described by an electric field distribution $\widetilde{\mathbf{E}}_m(\mathbf{r})$ and a complex frequency $\widetilde{\omega}_m$ (blue dots), which are the eigenmodes and eigenvalues of the source-free Maxwell's equations with outgoing-wave boundary conditions. The field distribution $\widetilde{\mathbf{E}}_m(\mathbf{r})$ diverges exponentially at $|\mathbf{r}| \to \infty$. Adapted from [14].

eral formalism, based on auxiliary fields, which explains that there is an infinity of mathematically-sound possible formulas for the excitation coefficient α_m. Numerical results validate the different formulas and compare their accuracy, showing that when a great number of QNMs and other numerical modes are included in the expansion, the expansion converges.

Chapter 4's focus will be how the modes of one-dimensional or two-dimensional structures are computed and how the computation of QNMs is affected by the periodicity. We present a comprehensive theory of grating anomalies and develop a formalism to expand the field scattered by metallic or dielectric gratings into the QNM basis, giving insight into the spectral properties of gratings. We once again show that a combination of QNMs and numerical modes is necessary in order to converge towards the correct value of the reflectance of the grating.

Chapter 5 seeks to highlight some of the numerical problems that arise when reconstructing the scattered field with the modal expansion. We aim to show that both numerical and natural physical modes are affected by the numerical parameters of the simulations such as the properties of the perfectly matched layers used to satisfy the outgoing wave boundary condition and the finesse of the mesh. At the end, we try to sort the modes according to their possible impact on the spectra and try to gauge the convergence speed of the expansion.

Chapter 6 aims to only include the physical quasinormal modes in the expansion while accurately reconstructing the spectra by employing a numerical

method to replace the contribution from non-physical modes. If quasinormal modes contain the main, resonant variations of the field, then the remaining non-resonant contribution after the few QNMs are included in the expansion should be a smooth function spanning the whole spectra. This smooth non-resonant contribution could be accurately interpolated from a small finite number of real frequency simulations. We implement this interpolation scheme as a substitute for the computation of numerical modes which bear no physical meaning.

Chapter 2

The Quasinormal mode expansion

Resonators are structures whose responses are exalted at certain frequencies. They oscillate with greater amplitude when the excitation is done at resonant frequencies. These resonators exist in many forms, be they mechanic in the case of a spring harmonic resonator, or electromagnetic in the case RLC circuit. In optics, these resonators enhance and localize the impinging light in different ways. In the case of photonic cavities, the light is confined and the field is exalted inside the resonator due to the repeat oscillations back and forth of the light inside the cavity. In the case of plasmonic resonators, the light is confined at the surface of the plasmonic material, like gold or metal, due to the oscillation of electrons caused by the incident light [22]. These devices come in many shapes and forms [52, 53, 12, 54, 55, 56] and are instrumental in the control of light at the nanoscale.

The energy the resonator receives is then scattered into free space or absorbed by the resonator. The main conduit for this release of the incoming energy are the modes of the system. Depending on the shape and frequency of the exciting wave, the energy is loaded into the resonator and dispersed into the different modes of the system. In this chapter, we define the electromagnetic modes of open, absorbing and dispersive systems, a system is said to be closed if the fields are confined to a finite region in space, like an enclosed cavity. An open cavity, however, is not confined and leaks the energy to the whole universe. We call those systems non-Hermitian. The modes of the non-Hermitian systems are called Quasinormal modes (QNMs). They are the eigensolutions of Maxwell's wave equation which satisfy the outgoing wave boundary conditions. We will first present the quasinormal mode formalism, and its implications. We will then present the 1D case of an Fabry-Pérot cavity, analytically and numerically. The performance of the numerical simulation in computing the modes will then be compared to analytical results and the modal expansion's accuracy with a finite number of modes will be evaluated. This chapter serves to provide a overview of the accuracy of the modal expansion using a numerical eigenmode solver to compute the modes. These tools are necessary to compute the modes of more complex resonator geometries with more complicated material make-up.

2.1 Quasinormal Mode Expansion

The scattering problem is the following. A scatterer defined by the permittivity distribution $\varepsilon(\mathbf{r}, \omega)$ is illuminated by a driving field $[\mathbf{E}_d(\mathbf{r}, \omega), \mathbf{H}_d(\mathbf{r}, \omega)]$ at the fre-

quency ω, creating a scattered field $[\mathbf{E}_s(\mathbf{r},\omega), \mathbf{H}_s(\mathbf{r},\omega)]$ that satisfies the scattered formulation of Maxwell's equations:

$$\begin{cases} \nabla \times \mathbf{H}_s(\mathbf{r},\omega) + i\omega\varepsilon(\mathbf{r},\omega)\mathbf{E}_s(\mathbf{r},\omega) &= i\omega(\varepsilon(\mathbf{r},\omega) - \varepsilon_b)\mathbf{E}_d(\mathbf{r},\omega) \\ \nabla \times \mathbf{E}_s(\mathbf{r},\omega) - i\omega\mu\mathbf{H}_s(\mathbf{r},\omega) &= i\omega(\mu - \mu_b)\mathbf{H}_d(\mathbf{r},\omega) \\ + \text{outgoing wave condition,} \end{cases} \tag{2.1}$$

where $\varepsilon_b(\mathbf{r},\omega)$ and $\mu_b(\mathbf{r},\omega)$ are the permittivity and permeability distributions for the background medium in which the driving field satisfies Maxwell's equation. In this problem we solve for the scattered field $\mathbf{\Psi}_s(\mathbf{r},\omega) = [\mathbf{E}_s(\mathbf{r},\omega), \mathbf{H}_s(\mathbf{r},\omega)]$ with a source $\mathbf{S}(\mathbf{r},\omega) = [\omega(\mu - \mu_b)\mathbf{H}_d(\mathbf{r},\omega), \omega(\varepsilon - \varepsilon_b)\mathbf{E}_b(\mathbf{r},\omega)]$:

$$\widehat{\mathbf{H}}(\mathbf{r},\omega)\mathbf{\Psi}_s(\mathbf{r},\omega) = \omega\mathbf{\Psi}_s(\mathbf{r},\omega) + \mathbf{S}(\mathbf{r},\omega), \text{ with } \widehat{\mathbf{H}}(\mathbf{r},\omega) = \begin{bmatrix} 0 & i\varepsilon^{-1}(\mathbf{r},\omega)\nabla\times \\ -i\mu^{-1}\nabla\times & 0 \end{bmatrix}. \tag{2.2}$$

To numerically solve this problem, with finite elements methods, we construct the matrices $\widehat{\mathbf{H}}(\mathbf{r},\omega)$, and $\mathbf{S}(\mathbf{r},\omega)$, and taking Eq. 2.2, we can find the problem's unknown $\mathbf{\Psi}_s$ at the frequency ω by performing the following matrix inversion:

$$\mathbf{\Psi}_s(\mathbf{r},\omega) = (\widehat{\mathbf{H}}(\mathbf{r},\omega) - \omega\widehat{\mathbf{I}})^{-1}\mathbf{S}(\mathbf{r},\omega), \tag{2.3}$$

where $\widehat{\mathbf{I}}$ is the identity matrix. For every value of the frequency ω, the inverse of the matrix $(\widehat{\mathbf{H}}(\mathbf{r},\omega) - \omega\widehat{\mathbf{I}})$ has to be recomputed. If $\widehat{\mathbf{H}}$ does not depend on ω, then the eigenvectors of $\widehat{\mathbf{H}}$ are the poles of the Maxwell operator.

Modal processes, on the other hand seek to solve the eigenvalue problem of equation 2.2 by using the spectral theorem and finding the eigenvectors and eigenvalues of the matrix $(\widehat{\mathbf{H}}(\mathbf{r},\omega))$. The quasinormal modes of the structure are the eigen modes $\widetilde{\mathbf{\Psi}}_m(\mathbf{r}) = [\widetilde{\mathbf{E}}_m(\mathbf{r}), \widetilde{\mathbf{H}}_m(\mathbf{r})]$ of the source-free Maxwell's equations at the complex frequency $\widetilde{\omega}_m$:

$$\begin{cases} \nabla \times \widetilde{\mathbf{H}}_m(\mathbf{r}) + i\widetilde{\omega}_m\varepsilon(\mathbf{r},\widetilde{\omega}_m)\widetilde{\mathbf{E}}_m(\mathbf{r}) &= 0 \\ \nabla \times \widetilde{\mathbf{E}}_m(\mathbf{r}) - i\widetilde{\omega}_m\mu\widetilde{\mathbf{H}}_m(\mathbf{r}) &= 0 \\ + \text{outgoing wave condition,} \end{cases} \tag{2.4}$$

The real part of the complex frequency $\widetilde{\omega}_m$ denotes the resonant frequency while the imaginary denotes the spectral width of the resonance and is inversely proportional to the temporal lifetime of the mode. We can rewrite Eq. 2.4 as the following eigenproblem:

$$\widehat{\mathbf{H}}(\mathbf{r},\widetilde{\omega}_m)\widetilde{\mathbf{\Psi}}_m(\mathbf{r}) = \widetilde{\omega}_m\widetilde{\mathbf{\Psi}}_m(\mathbf{r}). \tag{2.5}$$

If $\widehat{\mathbf{H}}$ is frequency-dependent, then Eq. 2.5 is a non-linear eigenvalue problem and the set of eigenvectors does not necessarily form an orthogonal basis. If $\widehat{\mathbf{H}}$ does not depend on ω, then Eq. 2.5 describes a linear-eigenvalue problem. For non-dispersive materials, this means that the orthogonality of the QNM basis can be shown using the Lorentz Reciprocity theorem [37]. For dispersive materials, the dispersion relation has to be taken into account in order for the orthogonality to be valid [30]. This means that the operator $\widehat{\mathbf{H}}$ is diagonalizable, and that the scattered field can be written as a sum of the eigen modes:

$$\mathbf{\Psi}_s(\mathbf{r},\omega) = \sum_m \alpha_m(\omega)\widetilde{\mathbf{\Psi}}_m(\mathbf{r}), \tag{2.6}$$

where α_m, the excitation coefficient, is a scalar that can be computed analytically. The eigenvectors $\widetilde{\mathbf{\Psi}}_m$ are intrinsic to the resonator and do not depend on the wave exciting the system. This means that once these modes are computed, the scattered field can be reconstructed from the superposition of these modes. However, the derivation of analytical formulas for the excitation coefficient requires the modes to be properly normalized. The imaginary part of the QNM frequency corresponds to the temporal decay of the mode, which conversely translates into a divergence in space as the distance from the resonator $|\mathbf{r}| \to \infty$, meaning that the integrated energy of a QNM in the entire space is infinite and thus standard energy normalizations are not applicable. If the system is modeled using finite elements, the system cannot be infinitely large and the computational domain needs to be finite while still allowing the boundary conditions to be fulfilled at $|\mathbf{r}| \to \infty$. One of the solutions to that problem is to use Perfectly Matched Layers to satisfy the out-going wave conditions. Perfectly Matched Layers induce a complex coordinate transform in space allowing the outgoing wave conditions to be satisfied with a finite computation domain. The normalization coefficient of the QNMs has the following expression:

$$\int_\Omega \frac{\partial(\widetilde{\omega}_m \varepsilon(\widetilde{\omega}_m))}{\partial \widetilde{\omega}_m} \widetilde{\mathbf{E}}_m \cdot \widetilde{\mathbf{E}}_m - \frac{\partial(\widetilde{\omega}_m \mu(\widetilde{\omega}_m))}{\partial \widetilde{\omega}_m} \widetilde{\mathbf{H}}_m \cdot \widetilde{\mathbf{H}}_m d\mathbf{r}, \tag{2.7}$$

where Ω is the entire computational domain. This formula was demonstrated using the Lorentz reciprocity theorem to be independent of PML thickness in [37].

Due to the discretization of the Maxwell operator into a finite-dimension matrix, the diagonalization of the operator becomes easier to achieve. However, the discretization affects the QNMs $\widetilde{\mathbf{\Psi}}_m$ that the solver is able to compute, depending on the detail of discretization, such as the size of the mesh elements in the case of a finite element model or the boundary conditions that are applied. The QNMs are thus computed with a certain degree of accuracy, with discrepancies on the field and eigenvalue because of the discretization. In general, the mode solver can resolve QNMs correctly within a finite frequency range whose size varies with the quality of the mesh. However, other numerical modes are computed instead of the QNMs that were not resolved. These modes are usually referred to as PML modes [32] due to their noticeable dependence, compared to QNMs, on the properties of these layers used to satisfy boundary conditions. Numerical modal expansions thus feature two sets of modes, the QNMs which correspond to observable, physical resonances, and PML or numerical modes, a side effect of the discretization and numerical tools.

2.2 Fabry-Pérot Cavity

In this section, we will present a one-dimensional dielectric resonator case, the Fabry-Pérot cavity. This example is quite significant because the QNMs can be computed analytically and second it has been mathematically shown that the expansion is complete inside the resonator by Leung and al. [31] in the early landscape of QNM literature. This section will first give the analytical formulas for the resonances of the Fabry-Pérot cavity and then demonstrate the property of com-

pleteness that shows that, inside the cavity, the modal expansion can reconstruct the field exactly if all the modes are included. We will then numerically compute the modes of the cavity with finite elements, and attempt to reconstruct the field. This section aims to illustrate the consequences of the numerical implementation of mode computation and of the modal expansion on this example where the eigenfields and eigenfrequencies are analytically known and PML modes are irrelevant.

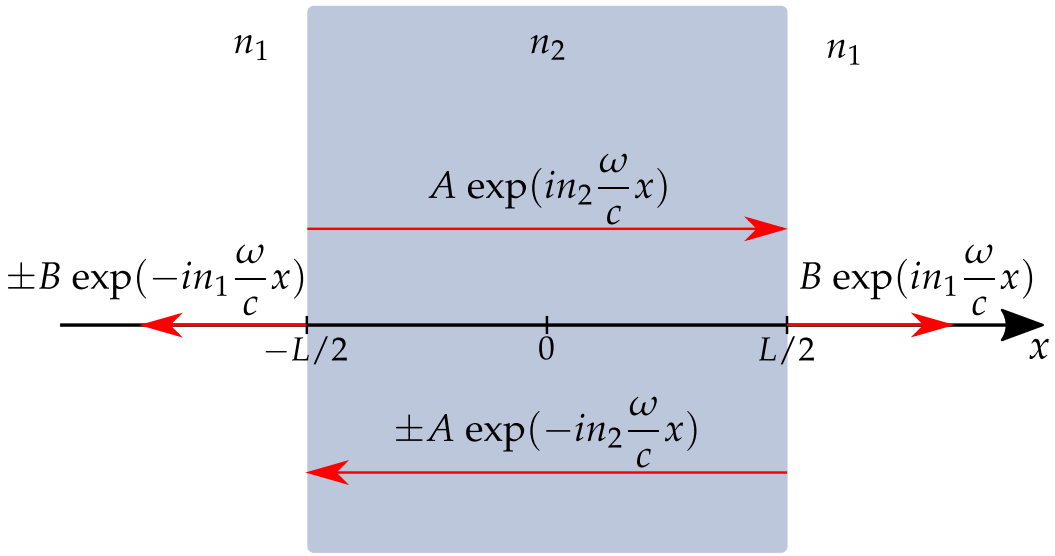

Figure 2.1: Schematic of the modes Fabry-Pérot cavity of size L and of the quasi-normal modes of the cavity. Adapted from [14].

The Fabry-Pérot cavity is made of two parallel reflecting surfaces between which waves are reflected back in forth. A schematic of a Fabry-Pérot cavity made of a dielectric slab of width L as pictured in Fig. 2.1.

2.2.1 Analytical Eigenmodes

In the case of a singular slab of thickness L of non-dispersive refractive index n_2 placed in a homogeneous background medium n_1. The eigenmodes are created by plane waves traveling back and forth between the two interfaces as drawn on Fig. 2.1. The interfaces have reflection and transmission coefficients $r = \frac{n_2 - n_1}{n_2 + n_1}$ and $t = \frac{2n_1}{n_2 + n_1}$. We consider for the rest of the chapter the $\exp(-i\omega t)$ convention for time-harmonic fields. The field at frequency ω in the absence of the driving field can be written as as the superposition of two counter-propagating

plane waves inside the cavity and two outgoing plane waves outside:

$$\mathbf{E}(x) = \begin{cases} A\exp(in_2\frac{\omega}{c}x) \pm A\exp(-in_2\frac{\omega}{c}x) & for\ |x| < \frac{L}{2} \\ B\exp(in_1\frac{\omega}{c}x) & for\ x > \frac{L}{2} \\ \pm B\exp(-in_1\frac{\omega}{c}x) & for\ x > \frac{-L}{2} \end{cases} . \tag{2.8}$$

Both symmetric and anti-symmetric modes can exist inside the cavity, represented by the plus/minus sign. The amplitude B of the outgoing plane waves is related to the amplitude A by $B\exp\left(in_1\frac{\omega}{c}\frac{L}{2}\right) = At\exp\left(in_2\frac{\omega}{c}\frac{L}{2}\right)$. In order for a wave of frequency $\widetilde{\omega}_m$ to resonate inside the cavity, the field amplitude A should be recovered from one back and forth trip inside the resonator, so after two reflections off of the interfaces: $A = Ar^2\exp\left(2i\frac{\widetilde{\omega}_m}{c}n_2L\right)$. We can thus find the expression of the eigenfrequency:

$$\widetilde{\omega}_m = m\pi\frac{nL}{c} + i\ln(r). \tag{2.9}$$

The expression for the eigenfrequency in Eq. 2.9 outlines how the modes are placed in the complex plane. The real parts of the modes' eigenfrequencies are evenly spaced and the integer m represents the total number of complete oscillations the plane wave makes in the cavity. The eigenfrequencies' imaginary parts are the same for all of these resonant modes and is given by the value of the reflection coefficient r, which shows a direct relationship between the cavity's leakage and the eigenfrequency's imaginary part.

2.2.2 Completeness inside the resonator

Leung and al.'s 1994 paper [31] demonstrates many important results in the case of one-dimensional leaky optical cavities. They define the cavity as a discontinuity in the refractive index. The quasinormal mode expansion is shown to be complete inside the cavity, meaning that if all the modes are included in the expansion, then the field can accurately be reconstructed. They also demonstrate the orthogonality of the modes. These demonstrations are done analytically for these types of non-Hermitian systems. In Chapter 3, we verify these properties numerically using matrices with finite sizes. The core of these demonstrations revolves around the use of the Green's function and the residue theorem. The Green function of a wave equation is the solution of the wave equation for a point source, which can be used to define the solution due to a general source using the superposition of multiple point sources. Finding an expression to the Green's function is akin to expressing the field. We will give a simplified general overview of the demonstration here. A more complete demonstration, heavily inspired by [31] is shown in Appendix A, which covers the 1D Fabry-Pérot example. The scalar Green's function in this one-dimensional case in the time harmonic domain is described as:

$$(-\frac{\omega^2}{c^2}\rho - \frac{\partial^2}{\partial x^2})\widetilde{G}(x,y;\omega) = \delta(x-y), \tag{2.10}$$

where y is a position in space, δ is the Dirac function and $\rho(x) = n(x)^2$, where $n(x)$ is the refractive index. The quasinormal modes are here the poles of the Green's function in the complex plane, $\lim_{\omega \to \widetilde{\omega}_m} \left| \widetilde{G}(x, y; \omega) \right| = +\infty$.

The Green's function in time-domain $G(x, y, t)$ can be obtained by performing an inverse Fourier Transform:

$$G(x, y, t) = \frac{1}{2\pi} \int_{-\infty}^{+\infty} \widetilde{G}(x, y, \omega) e^{-i\omega t} dt. \tag{2.11}$$

This integral can be evaluated using the residue theorem and the analytical continuation of the Green's function in the complex plane. Let us consider the half-circle shaped integration contour $\mathcal{C} = [-\omega_c, \omega_c] \cup \{\omega_c e^{i\theta}, \theta \in [-\pi, 0]\}$, with $\omega_c \to +\infty$.

We denote the residue around the pole $\widetilde{\omega}_m$ as R_m. We then apply the residue theorem for this contour, giving us:

$$\int_{\mathcal{C}} \widetilde{G}(x, y, \omega) e^{-i\omega t} dt = 2i\pi \sum_{\widetilde{\omega}_m \in \mathcal{C}} R_m e^{-\widetilde{\omega}_m t}. \tag{2.12}$$

If there are no branch cuts in the area of the complex plane enclosed by the contour, and if

$$\lim_{|\mathrm{Im}(\omega)| \to +\infty} \widetilde{G}(x, y, \omega) = 0, \tag{2.13}$$

we can show, using the residue theorem, for $\omega_c \to \infty$, that the Green's function can be expressed as a sum of the residues of the resonances comprised within the contour, as show in Fig. 2.2 :

$$G(x, y, t) = -i \sum_m R_m e^{-i\widetilde{\omega}_m t}. \tag{2.14}$$

The temporal Green's function satisfies the initial condition:

$$\rho(x) \frac{\partial G}{\partial t}(x, y, t = 0^+) = \delta(x - y). \tag{2.15}$$

Using Eq. 2.14 and 2.15, we obtain the relation proving completeness:

$$-\rho(x) \sum_m R_m e^{-i\widetilde{\omega}_m t} = \delta(x - y), \tag{2.16}$$

showing that the field can be written as a sum of the resonant contributions, the quasinormal modes of the structure defined by the permittivity distribution $\rho(x)$, which make the field diverge when evaluated at their eigenfrequency. In [31], it is shown for the Fabry-Pérot cavity that the completeness is only verified inside the resonator. This demonstration is shown in Appendix A.

The completeness relation means that the field can be reconstructed using the modal expansion, provided that all the QNMs are included in the expansion. For the case of a one-dimensional cavity, this is shown to be true only inside the cavity. In the case of structures whose modes can be expressed analytically, then infinite sum theorems might be able to be used to prove this. However, these examples are few and for the complex shapes that resonators might take,

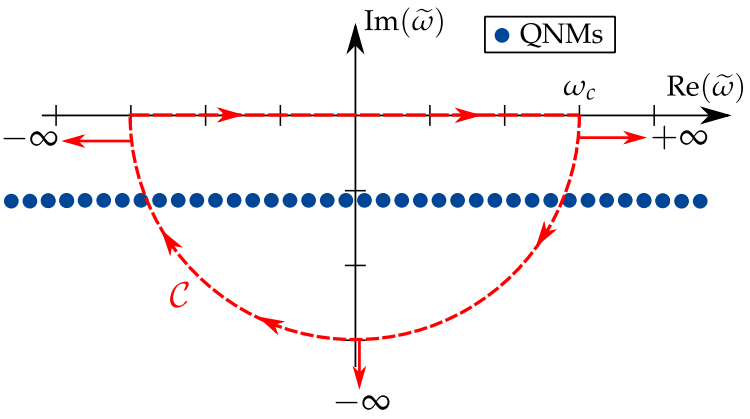

Figure 2.2: Integration contour for the residue theorem. The quasinormal modes, the poles of the Green's function are then all inside the contour, when the radius of this one is stretched to infinity.

numerical tools are used to compute the modes and field. In the next section, we will use a Finite Element software to compute the modes of the Fabry-Pérot cavity and reconstruct the scattered field with the computed QNMs.

2.2.3 Numerical experiment

The aim of this section is to test the ability of a finite element solver in computing the modes of a Fabry-Pérot. We are thus comparing numerically computed modes with ones that can be computed analytically. The scattered field of the cavity after illumination by a plane wave will be evaluated with the modal expansion using the numerically computed QNM modes. We consider the Fabry-Pérot cavity described in section 2.2 and model it in the finite element solver Montjoie [48] with $n_1 = 1$, $n_2 = \sqrt{3}$, and $L = 2$. The simulation uses reduced units of distance with the celerity $c = 1$ and normalizing lengths by $l = 1000\,\text{nm}$, frequencies are normalized by $\omega_{norm} = 2\pi \times 3\,10^{14}\ \text{rad} \cdot \text{s}^{-1}$. The simulation domain is bounded instead of infinite. To satisfy boundary conditions to compute the modes, we either apply Absorbing boundary conditions at $|x| = b = 2$, which are exact in 1D. The mesh is regularly meshed with a step h. With these reduced units, the exact eigenfrequency of the m^{th} QNM is given by the following formula:

$$\widetilde{\omega}_{m,exact} = m\frac{\pi}{2n_2} - i\frac{1}{2n_2}\ln\left(\frac{n_2+n_1}{n_2-n_1}\right). \tag{2.17}$$

In Fig. 2.3, we plot the eigenfrequencies $\widetilde{\omega}_{m,num}$ found by the solver, instead of having them line up horizontally in the complex plane like we would expect according to Eq. 2.9, only QNMs up to a certain real frequency are computed correctly, while other modes appear due to other elements such as the boundary conditions used to verify the outgoing wave condition. The accuracy with which we compute a mode's eigenfrequency and eventually their eigenfield is heavily dependent on the finesse of the mesh in this instance. We plot in Fig. 2.3b, the

error on the eigenfrequency for different values of the mesh step h:

$$\Delta\widetilde{\omega}_m = |\widetilde{\omega}_{m,exact} - \widetilde{\omega}_{m,num}|. \tag{2.18}$$

This error is computed by comparing the analytical eigenfrequency with the nearest numerically-computed eigenfrequency. We see that the finer the mesh, the more precise the eigenfrequency estimation made by the solver. The same holds true for the eigenfields, as pictured on Fig. 2.4a. The error on the eigenvalue is given by:

$$\Delta\widetilde{E}_m = \frac{\left|\left|\widetilde{E}_m^{exact}(x) - \widetilde{E}_m^{QNM}(x)\right|\right|_x}{\left|\left|\widetilde{E}_m^{QNM}(x)\right|\right|_x}. \tag{2.19}$$

We compute this error by comparing a numerically-computed QNM and an analytically-obtained QNM with similar to near-identical eigenfrequencies.

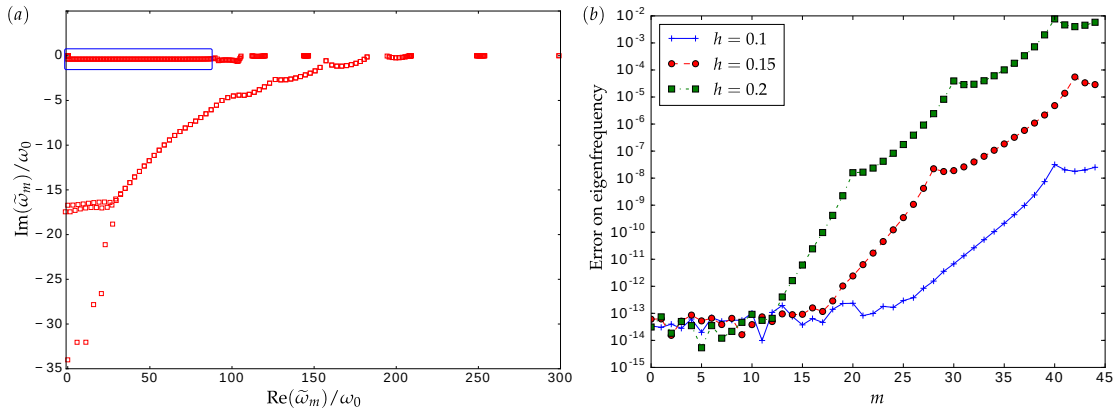

Figure 2.3: (a) Complex mode spectra for the Fabry-Pérot cavity computed with finite elements for $h = 0.1$. The analytical eigenfrequencies (QNMs) are computed correctly by the finite element solver until a threshold. We draw a blue rectangle over the correctly computed QNM eigenfrequencies. (b) Error on the computed eigenfrequency of the QNMs.

The computation of the eigenfrequency and eigenfield of a QNM is more precise as the mesh step h is smaller. The highest frequency QNM that can be resolved is dependent on the finesse of the mesh. However, the finer the mesh, the longer the computation time, and the higher the risk of reaching the computational limits of the solver and machine, which could realistically become an issue on more complex structures with more degrees of freedom.

We are able to determine which modes are QNM and which modes are numerical due to the formula in 2.9. We only use the QNMs to reconstruct the field. We plot the error on the reconstruction inside the cavity over the spectra in Fig. 2.4b for different values of the mesh step h. The error is defined as :

$$\Delta E_s(\omega) = \frac{||E_{s,exact}(x,\omega) - E_{s,QNM}(x,\omega)||_x}{||E_{s,exact}(x,\omega)||_x}, \tag{2.20}$$

and we see on Fig. 2.4b that the error falls as the mesh step decreases. Since only the 45 first QNMs are included in the expansion, the fastest oscillating mode oscillates at $\mathrm{Re}(\widetilde{\omega}_{45}) \approx 40.8$, more than 20 times the maximum excitation frequency

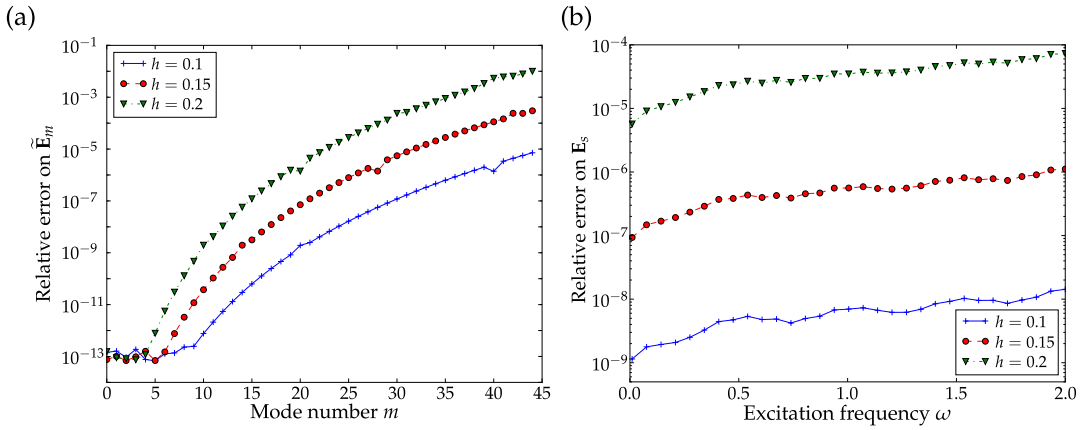

Figure 2.4: (a) Relative error on the computed modes with different mesh steps h. (b) Error on the reconstruction of the scattered field with $M = 45$ modes in the expansion when the cavity is illuminated by a plane wave.

in the considered spectra. The error steadily rises as the excitation frequency increases. We plot the field inside the cavity at the real frequency $\omega = 4.23$ in Fig. 2.5 for different numbers M of QNMs included the expansion. The QNMs are added in order of increasing resonant frequency. For reference, the real part of the eigenfrequency of $Re(\widetilde{\omega}_9) = 8.16$ is about twice the value of the excitation frequency and we can notice some very important discrepancies between the exact solution and the reconstructed field with $M = 10$ modes, even at the center of the cavity.

The field is correct inside most of the cavity but at the edge of the cavity is relatively inaccurate with very few QNMs as seen in Fig. 2.5b. The more modes are added into the expansion, the more accurate the field inside the cavity and especially on the edge becomes. Even with 100 modes, we still have a very noticeable difference at the edge of the cavity. These results seem similar to other reconstructions of the field of the Fabry-Pérot cavity found in [14]. In this article, in Fig. 10, the field is well reconstructed inside the cavity with 13 QNMs, with the reconstruction with 5 QNMs showing some slight discrepancies inside the cavity, more noticeably near the edge of the cavity.

In this example, we see the limits of this numerical attempt to reconstruct. We can observe that the Finite Element solver can only compute the quasinormal modes correctly within a frequency range, out of which their eigenfrequencies differ widely from their expected values given by Eq. 2.17. This is due to many numerical factors, like the boundary conditions and the finesse of the mesh. These different numerical conditions not only affect the computation of QNMs but also spawn numerical modes.

We illustrate this difference between the theoretical ideal and the numerical reality given by the tools we use in Fig. 2.6. Ideally, we would only like to use QNMs modes, because these modes hold physical meaning that we can use to analyze the dynamics of the resonator response. In this case, the cavity response is a superposition of waves oscillating from one end of the cavity to the other. However, the results of Fig. 2.5 imply that convergence inside the whole cavity might require hundreds of modes.

The number of modes M needed to reach a given accuracy will also depend

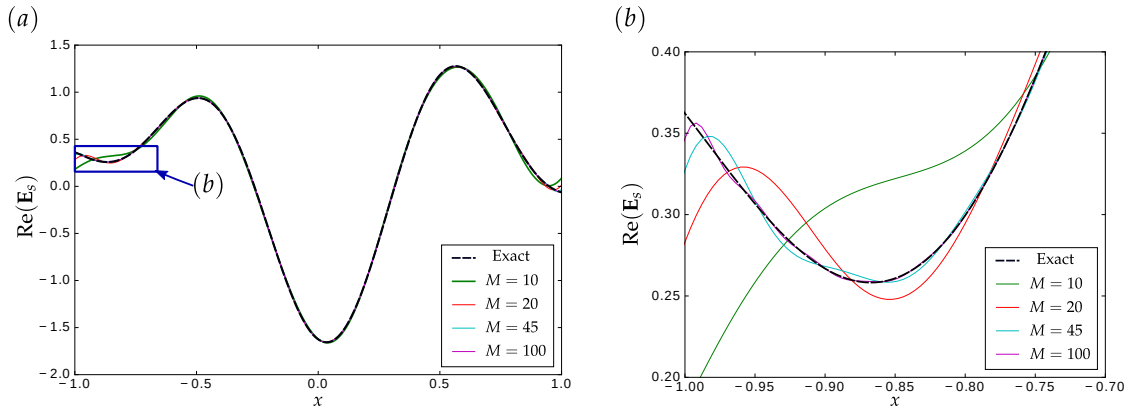

Figure 2.5: (a) Reconstruction of the field inside the cavity $(-1 < x < 1)$ with $M = 10, 20, 45, 100$ QNMs. (b) Reconstruction of the field on the left edge of the cavity.

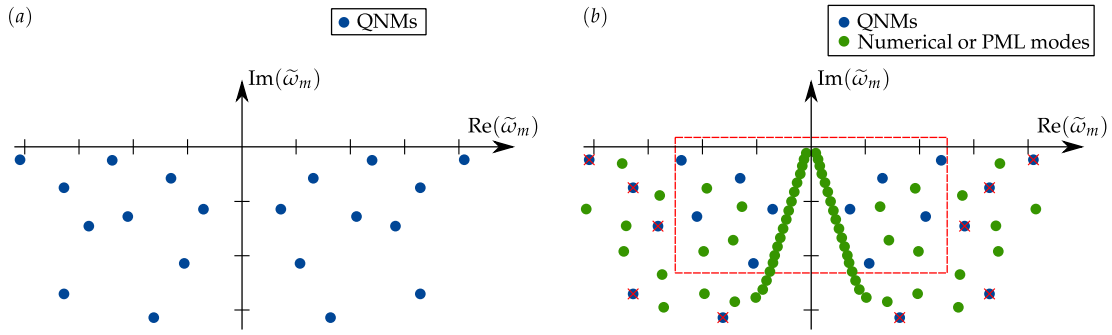

Figure 2.6: (a) Theoretical complex plane for a resonator where all the modes are QNMs. (b) Numerical complex plane for the same resonator. Due to the discretization of the system, We can only compute a limited set of QNMs, comprised within the red dotted box. Numerical modes, oftentimes called "PML modes" (see the footnotes of [57]) appear due to numerous numerical factors: finesse of the numerical mesh, ways to satisfy the outgoing-wave boundary conditions, using Perfectly Matched Layers, for example.

on the type of excitation. In this example, the excitation is a plane wave, the corresponding source term is $S(x,\omega) = \omega(n_2^2 - n_1^2)e^{i\omega x}$ inside the cavity and 0 elsewhere. The source term is discontinuous at the edges of the cavity and is projected upon the QNM basis, a set of continuous oscillating functions. This causes the oscillations of the reconstructed field at the edges of the cavity, like the Gibbs phenomenon when approximating a square with the corresponding Fourier series. There is also no given speed of convergence as the number of modes increase M. The expansion is expected to converge but will not converge at a set pace with each mode added into the expansion: some modes are more crucial to the reconstruction than others, which is helpful when analyzing resonator dynamics but there is no universal method of sorting the modes before reconstructing the field.

This section has shown that the numerical implementation of the QNM expansion suffers from side effects from the discretization and method.

2.3 Conclusion

In this chapter, we defined the eigenvectors of the Maxwell's equations for open systems, the quasinormal modes. These quasinormal modes, intrinsically linked to the resonator structure, are a useful mathematical tool to understand the dynamics of a resonator response. The quasinormal mode expansion being complete inside the resonator for one-dimensional cavities is an important result, showing that they can be used to reconstruct the resonator response exactly, provided all the modes are included in the expansion. While it is a powerful property for the QNM expansion, it is only applicable to these cavities and the numerical application has shown that the mesh computation for the one-dimensional example depends heavily on the finesse of the mesh.

We have observed however that for an example where the modes' field and eigenfrequencies have clear analytical expressions, that numerical solvers can only compute modes within a certain spectral range in the complex plane and that discretization and the numerical methods create modes of numerical origin. The role that these modes play in the convergence of the expansion, inside and out of the resonator, will be further investigated in Chapters 3, 4, and 5.

Chapter 3

Non-uniqueness of the Quasinormal mode expansion of Electromagnetic Lorentz Dispersive Materials

Optical micro and nanoresonators, be they plasmonic, photonic or hybrid, enhance and localize the electromagnetic energy at wavelength and subwavelength scales and are key components in many photonic applications. Their optical response is characterized by resonant features resulting from the excitation of one or a few dominant modes, intrinsic to the resonator. In the case of open resonators, where the energy leaks out into free space, the modes in questions are solutions of the source-free Maxwell's equations at the complex frequency $\widetilde{\omega}_m$ [14]:

$$\begin{cases} -i\,\widetilde{\omega}_m \varepsilon(\widetilde{\omega}_m)\widetilde{\mathbf{E}}_m(\mathbf{r}) - \nabla \times \widetilde{\mathbf{H}}_m(\mathbf{r}) &= 0, \\ -i\,\widetilde{\omega}_m \mu(\widetilde{\omega}_m)\widetilde{\mathbf{H}}_m(\mathbf{r}) + \nabla \times \widetilde{\mathbf{E}}_m(\mathbf{r}) &= 0, \\ + \text{Boundary conditions}, \end{cases} \tag{3.1}$$

where $\widetilde{\mathbf{E}}_m$ and $\widetilde{\mathbf{H}}_m$ are the electric and magnetic field vector distributions of the mode, intrinsic to the structure characterized by the dielectric permittivity distribution ε and the magnetic permeability distribution μ. Equation (1) defines an eigenvalue boundary problem to which the mode $\left[\widetilde{\mathbf{E}}_m, \widetilde{\mathbf{H}}_m; \widetilde{\omega}_m\right]$ is one of its many solutions [14].

These modes of open, leaky resonators are oftentimes called quasinormal modes (QNMs) to emphasize that their harmonic evolution is characterized by an exponential damping in time, since they are the eigenstates of a non-Hermitian operator. Consequently, the complex eigenfrequency $\widetilde{\omega}_m$ has a negative imaginary part, $\mathrm{Im}(\widetilde{\omega}_m) < 0$ (the $\exp(-i\omega t)$ convention for time-harmonic fields is assumed). Micro and nanoresonators play a leading role in many areas of nanophotonics. This pushes a strong pressure on the development of QNM theory and numerical methods that explicitly consider QNMs in the analysis, providing important clues towards the interpretation of the resonator response.

The resonator response (i.e. the field scattered by the resonator due to an excitation by a driving field) can be expanded as a superposition of its modes. This is what is commonly called reconstruction, and is usually summarized with

the following expansion in the frequency domain:

$$\mathbf{E}_s(\mathbf{r},\omega) = \sum_m \alpha_m(\omega)\widetilde{\mathbf{E}}_m(\mathbf{r}), \tag{3.2}$$

where $\mathbf{E}_s$ is the scattered electric field, computed at the real frequency ω, and α_m is the excitation coefficient of the m^{th} QNM mode. The excitation coefficient is at the center of the numerical efficiency of QNM-expansion reconstruction, owing to the analytical dependence of α_m with the frequency. This implies that, once the QNMs are computed, the reconstruction for many instances of the driving field is trivial, even in the temporal domain when resonators are illuminated by pulses [30, 58].

However while there is a general agreement on the use of the QNM expansion of Eq. 3.2 in the frequency domain, the expression of the excitation coefficient α_m varies, depending on the method used to project the scattered field onto the QNM basis. The recent review article [14] lists no fewer than five formulas, depending on the method used to project the scattered field onto the QNM basis, from a Green's dyadic decomposition [31, 59], Lorentz reciprocity theorem [37], biorthogonality products on discretized operators [32], to advanced numerical methods, e.g. the Lanczos reduction-type method [33]. And the list is getting longer. For material dispersion that can be described by a Drude-Lorentz model, a new formula for α_m, different from the one initially derived in [30] by linearizing the eigenproblem of Eq. 3.1 with auxiliary fields, has been proposed last year [34]. Even more recently, another formula for the expansion of the total field [60], this time, has been shown to provide better convergence performance than the formula in [30], as confirmed in a recent theoretical work on the use of the QNM expansion for non-linear nano-optics [41].

To understand why there are so many expressions, first it is important to differentiate two different approaches of the literature.

In foundational electromagnetic studies [61, 31] as well as in more advanced works [51, 62, 63], only "true" quasinormal modes are considered in the expansion of Eq. 3.2. The Maxwell operator of Eq. 3.1 is a continuous operator defined in an infinite open space. Completeness issues restrict the validity of the scattered-field expansion of Eq. 3.2 to the resonator inside, not over the whole space. Additionally, to avoid branch cuts in the complex plane, only resonators placed in uniform background (no substrate) can be considered. Only simple geometries, e.g. one-dimensional Fabry-Perot cavities and Mie sphere resonators, for which the QNMs can be analytically calculated over the entire electromagnetic spectrum, from DC to high frequencies, are accurately investigated. In this approach, whether the materials are dispersive or not, there are an infinity of correct formulas for α_m owing to the overcompleteness of the expansion [31, 51].

The approach that we consider hereafter is more oriented towards numerics. It is also simpler mathematically: the continuous operator of Eq. 3.1, originally defined on an unbounded space, is replaced by a discretized operator (a finite-dimensional matrix) defined on a finite mapped space [14], with new permittivity and permeability distributions that accommodate Perfectly Matched Layers (PMLs). Therefore only a subset of the infinite QNM sets of the continuous operator are accurately approximated and this subset is completed with another finite (but huge) set of numerical modes often referred as PML modes [14, 32, 36, 33, 30, 34, 35], as they originate from the finite-discretized space bounded by PMLs.

This approach preserves the spirit of QNM expansions since the QNMs with frequencies in the spectral range of interest are included, and additionally enable the analysis of complex resonators with arbitrary shapes [64], dispersive materials [36, 33, 30, 34, 35] and several inclusions (e.g. dimers) [30], within complex environments (e.g. deposited on metallic or dielectric substrates or embedded in thin-film stacks) [30, 35]. Owing to the finite-dimensional discretized operator, completeness of the scattered-field expansion of Eq. 3.2 is valid everywhere in the computational domain (inside or outside the resonator, even in the PML domains). The derivation of analytical formulas for α_m relies on simple algebra [30].

The present work focuses on the reconstruction problem of resonators composed of Drude-Lorentz materials, with the aim of clarifying the origin of the non-uniqueness for the expressions of the excitation coefficients by using a common formalism based on a linearization of the nonlinear eigenvalue problem. We start by re-introducing the quasinormal mode expansion of the scattered field for the sake of consistency, largely following the initial derivation in [30]. We further show that different linearizations of the nonlinear eigenvalue problem with the use of auxiliary fields yield different formulas for α_m, and successfully derive three formulas of the excitation coefficient α_m available in the recent literature. The derivation evidences that all these formulas are mathematically correct, a point that is further checked with numerical data exhibiting convergence towards the same unique solution.

We then use the auxiliary field approach to show that, in fact, an infinity of formulas can be found by writing different linearization schemes of Maxwell's equations. We also explain how degenerate eigenvalues (i.e. multiple eigenvalues) can be treated correctly with a simple Gram-Schmidt orthogonalization procedure. Finally, numerical results are presented in order to compare the accuracy of the three different formulas that will have been rederived.

3.1 Scattering problem and excitation coefficients

The scattered field $[\mathbf{E}_s(\mathbf{r},\omega), \mathbf{H}_s(\mathbf{r},\omega)]$ is solution to the time-harmonic Maxwell's equations:

$$\left\{\begin{array}{lcl} -i\omega\varepsilon(\omega)\mathbf{E}_s(\mathbf{r},\omega) - \nabla\times\mathbf{H}_s(\mathbf{r},\omega) &=& i\omega(\varepsilon(\omega)-\varepsilon_b)\mathbf{E}_{inc}, \\ -i\omega\mu(\omega)\mathbf{H}_s(\mathbf{r},\omega) + \nabla\times\mathbf{E}_s(\mathbf{r},\omega) &=& i\omega(\mu(\omega)-\mu_b)\mathbf{H}_{inc}, \\ + \text{Sommerfeld conditions,} \end{array}\right. \tag{3.3}$$

where $[\mathbf{E}_{inc}, \mathbf{H}_{inc}]$ is the incident field and ε_b, μ_b are the permittivity and permeability of the background medium. The incident field satisfies the homogenous Maxwell's equations in the background medium. Let us introduce $\mathbf{J}(\mathbf{r},\omega) = i\omega(\varepsilon(\omega)-\varepsilon_b)\mathbf{E}_{inc}$, the source term. We are considering non-magnetic materials whose relative permittivity $\varepsilon(\omega)$ is described by a N-pole Drude-Lorentz model, thus $\mu(\omega) = \mu_b = \mu_0$ and:

$$\varepsilon(\omega)/\varepsilon_\infty = 1 - \sum_{i=1}^{N} \omega_{p,i}^2/(\omega^2 - \omega_{0,i}^2 + i\omega\gamma_i), \tag{3.4}$$

which may model a large variety of systems with increasing accuracy as the number of poles increases. It also respects the causality relation $\bar{\varepsilon}(\omega) = \varepsilon(-\bar{\omega})$ where $\bar{\omega}$ stands for the complex conjugate of ω. The contributions of a free electron-gas of metals can be treated by a Drude permittivity, setting $\omega_{0,i} = 0$.

Let us denote Ω_{res} the domain of the resonator for which $\varepsilon(\omega)$ is different from ε_b (hence it is the support of the source term $\mathbf{J}$). In [14], a review of the literature surrounding quasinormal modes, an attempt was made to classify the different formulas used to compute the excitation coefficients. At least three formulas for α_m were reported:

- The formula 5.11 in [14]:

$$\alpha_m = \frac{1}{i(\widetilde{\omega}_m - \omega)} \int_{\Omega_{res}} \mathbf{J}(\mathbf{r}, \omega) \cdot \widetilde{\mathbf{E}}_m(\mathbf{r}) d\mathbf{r} \tag{3.5}$$

- The formula proposed in [30] (equivalent to formula 5.6 in [14]):

$$\begin{aligned} \alpha_m = \int_{\Omega_{res}} \quad & (\varepsilon_b - \varepsilon_\infty)\mathbf{E}_{inc} \cdot \widetilde{\mathbf{E}}_m(\mathbf{r}) \\ & + \frac{\widetilde{\omega}_m}{\widetilde{\omega}_m - \omega}(\varepsilon(\widetilde{\omega}_m) - \varepsilon_b)\mathbf{E}_{inc} \cdot \widetilde{\mathbf{E}}_m(\mathbf{r}) d\mathbf{r}, \end{aligned} \tag{3.6}$$

- The formula proposed in [34] (equivalent to formula 5.10 in [14]):

$$\alpha_m = \frac{\omega}{i\,\widetilde{\omega}_m(\widetilde{\omega}_m - \omega)} \int_{\Omega_{res}} \mathbf{J}(\mathbf{r}, \omega) \cdot \widetilde{\mathbf{E}}_m(\mathbf{r}) d\mathbf{r}. \tag{3.7}$$

All these formulas hold if the modes $\widetilde{\mathbf{E}}_m$ are normalized as follows

$$\int_\Omega \frac{\partial(\widetilde{\omega}_m \varepsilon(\widetilde{\omega}_m))}{\partial \widetilde{\omega}_m} \widetilde{\mathbf{E}}_m \cdot \widetilde{\mathbf{E}}_m - \frac{\partial(\widetilde{\omega}_m \mu(\widetilde{\omega}_m))}{\partial \widetilde{\omega}_m} \widetilde{\mathbf{H}}_m \cdot \widetilde{\mathbf{H}}_m d\mathbf{r}, \tag{3.8}$$

where Ω is the computational domain. This is the usual normalization [37]. Note that we use a tilde to differentiate the QNM fields from other fields, for instance the driving field or the scattered field, and consistently, we will also use a tilde to denote the QNM frequency $\widetilde{\omega}_m$.

3.2 Discrete modal expansion

In this section, we propose a common formalism based on the discrete Maxwell's equations to obtain these three formulas that we show to be valid for both QNMs and PML modes. More precisely, when $\varepsilon(\omega)$ is a rational function, auxiliary unknowns can be introduced in order to obtain a linear eigenvalue problem [33, 30]. After this linearization procedure and after discretization (e.g. with Finite Element Method), the time-harmonic Maxwell's equations can be written

$$-i\omega \widehat{\mathbf{M}}_h \mathbf{U}_h + \widehat{\mathbf{K}}_h \mathbf{U}_h = \mathbf{F}_h, \tag{3.9}$$

where $\widehat{\mathbf{M}}_h$ is the mass matrix, $\widehat{\mathbf{K}}_h \mathbf{U}_h$ is the stiffness matrix, and $\mathbf{F}_h$ is the source term while the subscript h denotes the mesh size. $\mathbf{U}_h$ is the main unknown that

will contain components of the scattered electric field $\mathbf{E}_s$ and other auxiliary unknowns introduced to obtain a linear eigenvalue problem. The Matrices $\widehat{\mathbf{M}}_h$ and $\widehat{\mathbf{K}}_h$ are independent of ω; an example of the matrices will be given in Section 4. The corresponding eigenvalue problem is

$$\widehat{\mathbf{K}}_h \widetilde{\mathbf{x}}_m = i\widetilde{\omega}_m \widehat{\mathbf{M}}_h \widetilde{\mathbf{x}}_m, \tag{3.10}$$

where $\widetilde{\mathbf{x}}_m$ is the right eigenvector of the system and its eigenvalue is $i\widetilde{\omega}_m$. Assuming $\widehat{\mathbf{M}}_h^{-1}\widehat{\mathbf{K}}_h$ is diagonalizable, we have $\widehat{\mathbf{M}}_h^{-1}\widehat{\mathbf{K}}_h = \widehat{\mathbf{V}}\widehat{\mathbf{D}}\widehat{\mathbf{V}}^{-1}$ where $\widehat{\mathbf{D}}$ is a diagonal matrix with eigenvalues $i\widetilde{\omega}_m$ on the diagonal and $\widehat{\mathbf{V}}$ the matrix whose columns are formed with the right eigenvectors $\widetilde{\mathbf{x}}_m$. The biorthogonal vectors of $\widehat{\mathbf{M}}_h^{-1}\widehat{\mathbf{K}}_h$ denoted $\mathbf{w}_m$, are the rows of matrix $\widehat{\mathbf{V}}^{-1}$. Since $\widehat{\mathbf{V}}\widehat{\mathbf{V}}^{-1} = \widehat{\mathbf{I}}$, vectors $\widetilde{\mathbf{x}}_m$ and $\mathbf{w}_m$ are biorthogonal: $\langle \widetilde{\mathbf{x}}_m, \mathbf{w}_m \rangle = \delta_{mn}$. The biorthogonal vector $\mathbf{w}_m$ can also be found by searching for the right eigenvectors of the transpose of $\widehat{\mathbf{M}}_h^{-1}\widehat{\mathbf{K}}_h$. In the case where $\widehat{\mathbf{K}}_h$ and $\widehat{\mathbf{M}}_h$ are symmetric, we have $(\widehat{\mathbf{M}}_h^{-1}\widehat{\mathbf{K}}_h)^T = \widehat{\mathbf{K}}_h\widehat{\mathbf{M}}_h^{-1}$. Hence $\mathbf{w}_m$ solves the following eigenvalue problem $\widehat{\mathbf{K}}_h\widehat{\mathbf{M}}_h^{-1}\mathbf{w}_m = i\widetilde{\omega}_m\mathbf{w}_m$. By introducing the left eigenvector $\widetilde{\mathbf{x}}_m^{\perp} = \widehat{\mathbf{M}}_h^{-1}\mathbf{w}_m$, we have come back to equation Eq. 3.10, meaning that $\widetilde{\mathbf{x}}_m^{\perp} = \widetilde{\mathbf{x}}_m$, provided that the eigenvector $\widetilde{\mathbf{x}}_m$ is normalized such that

$$\langle \widehat{\mathbf{M}}_h \widetilde{\mathbf{x}}_m, \widetilde{\mathbf{x}}_m \rangle = 1. \tag{3.11}$$

The convention $\langle \mathbf{x}, \mathbf{y} \rangle = \sum_i x_i y_i$ is used. Equation Eq. 3.11 is the discrete equivalent of equation Eq. 3.8. The solution $\mathbf{U}_h$ in Eq. 3.9 is expanded into the right eigenvectors $\widetilde{\mathbf{x}}_m$ (they form a basis under our assumption that the matrix is diagonalizable): $\mathbf{U}_h = \sum_m \alpha_m \widetilde{\mathbf{x}}_m$. By injecting this expansion into Eq. 3.9 and using Eq. 3.10, we obtain

$$\sum_m \alpha_m(-i\omega + i\widetilde{\omega}_m)\widehat{\mathbf{M}}_h\widetilde{\mathbf{x}}_m = \mathbf{F}_h. \tag{3.12}$$

The modal excitation coefficient α_m is directly obtained by projecting this equation onto the left eigenvector $\widetilde{\mathbf{x}}_m^{\perp}$ [32],

$$\alpha_m = \frac{1}{i(\widetilde{\omega}_m - \omega)} \langle \mathbf{F}_h, \widetilde{\mathbf{x}}_m^{\perp} \rangle. \tag{3.13}$$

From a discrete point of view, once the discrete linear system Eq. 3.9 is set, equation Eq. 3.13 is the unique general formula for α_m. In this specific case where the matrices $\widehat{\mathbf{K}}_h$ and $\widehat{\mathbf{M}}_h$ are symmetric, $\widetilde{\mathbf{x}}_m^{\perp} = \widetilde{\mathbf{x}}_m$ and we obtain

$$\alpha_m = \frac{1}{i(\widetilde{\omega}_m - \omega)} \langle \mathbf{F}_h, \widetilde{\mathbf{x}}_m \rangle, \tag{3.14}$$

which justifies that the expansion formulas of Eq. 3.5, 3.6, and 3.7 solely depend on the right eigenvector and not on the left eigenvector. This important result provides analyticity which has not been obtained in related works [32] and was derived in a different way using the divergence theorem and the continuous operator, not the discretized one, in [30].

Though the formula for the discrete version of the excitation coefficients is unique, the results of the biorthogonal projection described in Eq. 3.13 and 3.14 are not. Each different linearization will produce its own set of auxiliary unknowns, and consequently spawns a different set of matrices $\widehat{\mathbf{M}}_h$ and $\widehat{\mathbf{K}}_h$, and another source term $\mathbf{F}_h$, as we shall see.

3.3 Eigenmode expansion for the first-order formulation of Maxwell's Equations: Link between the discrete and continuous expansion

To simplify the notation hereafter, we assume that that only the resonator is composed of dispersive materials, but in practice, every domain with dispersive materials(including the PML) should be treated separately with auxiliary fields. We consider an isotropic medium with a dispersive permittivity described by a single-pole Lorentz model, $\varepsilon(\omega) = \varepsilon_\infty(1 - \omega_p^2/(\omega^2 - \omega_0^2 + i\gamma\omega))$, and a non-dispersive permeability $\mu(\omega) = \mu_0$. We introduce two auxiliary fields inside the resonator: the polarization $\mathbf{P}_s = -\varepsilon_\infty \dfrac{\omega_p^2}{\omega^2 - \omega_0^2 + i\gamma\omega}\mathbf{E}_s$ and the current $\mathbf{J}_s = -i\omega\mathbf{P}_s$ [33, 30]. With elementary algebraic manipulations, we can reformulate Maxwell's system in Eq. 3.3 as the following source problem:

$$\begin{cases} -i\omega\varepsilon_\infty\mathbf{E}_s + \mathbf{J}_s - \nabla\times\mathbf{H}_s &= \mathbf{J}, \\ -i\omega\mu_0\mathbf{H}_s + \nabla\times\mathbf{E}_s &= \mathbf{0}, \\ -i\omega\mathbf{P}_s - \mathbf{J}_s &= \mathbf{0}, \\ i\omega\mathbf{J}_s - \gamma\mathbf{J}_s - \omega_0^2\mathbf{P}_s + \varepsilon_\infty\omega_p^2\mathbf{E}_s &= \mathbf{0}, \end{cases} \tag{3.15}$$

inside the resonator. Outside the resonator, $\mathbf{E}_s$ and $\mathbf{H}_s$ solve Maxwell's equations in an uniform background: $-i\omega\varepsilon_b\mathbf{E}_s - \nabla\times\mathbf{H}_s = 0$, $-i\omega\mu_0\mathbf{H}_s + \nabla\times\mathbf{E}_s = \mathbf{0}$. In order to obtain a symmetric system, we multiply the second equation of Eq. 3.15 by -1, the third equation by $\omega_0^2/(\varepsilon_\infty\omega_p^2)$ and the fourth by $1/(\varepsilon_\infty\omega_p^2)$,

$$\begin{cases} -i\omega\varepsilon_\infty\mathbf{E}_s + \mathbf{J}_s - \nabla\times\mathbf{H}_s &= \mathbf{J}, \\ i\omega\mu_0\mathbf{H}_s - \nabla\times\mathbf{E}_s &= \mathbf{0}, \\ -i\omega\dfrac{\omega_0^2}{\varepsilon_\infty\omega_p^2}\mathbf{P}_s - \dfrac{\omega_0^2}{\varepsilon_\infty\omega_p^2}\mathbf{J}_s &= \mathbf{0} \\ \dfrac{i\omega}{\varepsilon_\infty\omega_p^2}\mathbf{J}_s - \dfrac{\gamma}{\varepsilon_\infty\omega_p^2}\mathbf{J}_s - \dfrac{\omega_0^2}{\varepsilon_\infty\omega_p^2}\mathbf{P}_s + \mathbf{E}_s &= \mathbf{0}, \end{cases} \tag{3.16}$$

We write this system using linear operators $\widehat{\mathbf{K}}$ and $\widehat{\mathbf{M}}$, and the source vector $\mathbf{F}$ and the solution $\mathbf{U}$.

$$\widehat{\mathbf{K}}\mathbf{U} - i\omega\widehat{\mathbf{M}}\mathbf{U} = \mathbf{F}, \tag{3.17}$$

with

$$\widehat{\mathbf{K}} = \begin{bmatrix} 0 & -\nabla\times & 0 & 1 \\ -\nabla\times & 0 & 0 & 0 \\ 0 & 0 & 0 & -\dfrac{\omega_0^2}{\varepsilon_\infty\omega_p^2} \\ 1 & 0 & -\dfrac{\omega_0^2}{\varepsilon_\infty\omega_p^2} & -\dfrac{\gamma}{\varepsilon_\infty\omega_p^2} \end{bmatrix}, \mathbf{U} = \begin{bmatrix} \mathbf{E}_s \\ \mathbf{H}_s \\ \mathbf{P}_s \\ \mathbf{J}_s \end{bmatrix},$$

$$\widehat{\mathbf{M}} = \begin{bmatrix} \varepsilon_e & 0 & 0 & 0 \\ 0 & -\mu_0 & 0 & 0 \\ 0 & 0 & \dfrac{\omega_0^2}{\varepsilon_\infty \omega_p^2} & 0 \\ 0 & 0 & 0 & -\dfrac{1}{\varepsilon_\infty \omega_p^2} \end{bmatrix}, \mathbf{F} = \begin{bmatrix} \mathbf{J} \\ \mathbf{0} \\ \mathbf{0} \\ \mathbf{0} \end{bmatrix}. \tag{3.18}$$

where $\varepsilon_e = \varepsilon_\infty$ inside the resonator domain and $\varepsilon_e = \varepsilon_b$ elsewhere. The unknowns $\mathbf{P}_s$ and $\mathbf{J}_s$ exist only inside the resonator. $\widehat{\mathbf{K}}, \widehat{\mathbf{M}}, \mathbf{U}$, and $\mathbf{F}$ are the continuous equivalents of the discrete $\widehat{\mathbf{K}}_h, \widehat{\mathbf{M}}_h, \mathbf{U}_h$, and $\mathbf{F}_h$, and equation Eq. 3.16 is the continuous equivalent of Eq. 3.9. In the same way, the continuous eigenvalue problem can be written $\widehat{\mathbf{K}}\widetilde{\mathbf{U}}_m = i\widetilde{\omega}_m \widehat{\mathbf{M}}\widetilde{\mathbf{U}}_m$ with $\widetilde{\mathbf{U}}_m = [\widetilde{\mathbf{E}}_m, \widetilde{\mathbf{H}}_m, \widetilde{\mathbf{P}}_m, \widetilde{\mathbf{J}}_m]^T$, similar to equation Eq. 3.10, with $\widetilde{\mathbf{U}}_m$ serving as the continuous equivalent of $\widetilde{\mathbf{x}}_m$. In the same way, Eq. 3.14 is the discrete equivalent of Eq. 3.5 since $\langle \mathbf{F}_h, \widetilde{\mathbf{x}}_m \rangle = \sum_i \widetilde{\mathbf{x}}_{m,i} \int_{\Omega_{res}} \mathbf{F}(\mathbf{r}) \cdot \boldsymbol{\varphi}_i(\mathbf{r})\, d\mathbf{r}$ where $\widetilde{\mathbf{x}}_{m,i}$ is the i-th component of $\widetilde{\mathbf{x}}_m$ and $\boldsymbol{\varphi}_i$ are finite element basis functions (given in chapter 5 of [65]). By swapping the sum and the integral, we obtain

$$\langle \mathbf{F}_h, \widetilde{\mathbf{x}}_m \rangle = \int_{\Omega_{res}} \mathbf{J}(\mathbf{r}, \omega) \cdot \widetilde{\mathbf{E}}_m(\mathbf{r}) d\mathbf{r}. \tag{3.19}$$

For numerical experiments, it is preferable to perform the scalar product as presented in Eq. 3.14 rather than approximating this integral. With the same arguments, we have the following equality:

$$\begin{aligned} \langle \widehat{\mathbf{M}}_h \widetilde{\mathbf{x}}_m, \widetilde{\mathbf{x}}_m \rangle = \int_\Omega & \varepsilon_e \widetilde{\mathbf{E}}_m \cdot \widetilde{\mathbf{E}}_m - \mu_0 \widetilde{\mathbf{H}}_m \cdot \widetilde{\mathbf{H}}_m \\ & + \frac{\omega_0^2}{\varepsilon_\infty \omega_p^2} \widetilde{\mathbf{P}}_m \cdot \widetilde{\mathbf{P}}_m - \frac{1}{\varepsilon_\infty \omega_p^2} \widetilde{\mathbf{J}}_m \cdot \widetilde{\mathbf{J}}_m d\mathbf{r}, \end{aligned} \tag{3.20}$$

Since $\widetilde{\mathbf{P}}_m = -\varepsilon_\infty \omega_p^2 / (\widetilde{\omega}_m^2 + i\gamma\widetilde{\omega}_m - \omega_0^2) \widetilde{\mathbf{E}}_m$ and $\widetilde{\mathbf{J}}_m = -i\widetilde{\omega}_m \widetilde{\mathbf{P}}_m$, it can be shown that

$$\langle \widehat{\mathbf{M}}_h \widetilde{\mathbf{x}}_m, \widetilde{\mathbf{x}}_m \rangle = \int_\Omega \frac{\partial(\widetilde{\omega}_m \varepsilon(\widetilde{\omega}_m))}{\partial \widetilde{\omega}_m} \widetilde{\mathbf{E}}_m \cdot \widetilde{\mathbf{E}}_m - \mu_0 \widetilde{\mathbf{H}}_m \cdot \widetilde{\mathbf{H}}_m d\mathbf{r}. \tag{3.21}$$

This relation proves that the normalization of Eq. 3.11 is the discrete equivalent of Eq. 3.8. Again, for the sake of simplicity, the relation of Eq. 3.11 is preferred to normalize discrete eigenvectors. Matrices $\widehat{\mathbf{M}}_h$ and $\widehat{\mathbf{K}}_h$ are real symmetric but both are indefinite. As a result, the eigenvalue problem $\widehat{\mathbf{K}}_h \widetilde{\mathbf{U}}_m = i\omega \widehat{\mathbf{M}}_h \widetilde{\mathbf{U}}_m$ is not selfadjoint and the eigenvalues are complex. Moreover inside the PML domains, the equations cannot be symmetrized and matrices $\widehat{\mathbf{K}}_h$ and $\widehat{\mathbf{M}}_h$ are not symmetric. While Eq. 3.21 normalizes the QNM fields, it cannot be used as a norm since $\langle \widehat{\mathbf{M}}_h \widetilde{\mathbf{x}}_m, \widetilde{\mathbf{x}}_m \rangle$ is a complex value.

3.4 Derivation of other formulas

3.4.1 Derivation of (3.6)

To obtain the formula of Eq. 3.5, first, we have written Maxwell's equations directly for the scattered field $[\mathbf{E}_s(\mathbf{r}, \omega), \mathbf{H}_s(\mathbf{r}, \omega)]$ and then introduced the auxiliary

fields $\mathbf{P}_s$ and $\mathbf{J}_s$. In the case of Eq. 3.6, in [30], Maxwell's equations are first written for the total fields and the auxiliary fields are introduced at this step. The total field $[\mathbf{E}_{tot}, \mathbf{H}_{tot}, \mathbf{P}_{tot}, \mathbf{J}_{tot}]$ solves the system of Eq. 3.15 with $\mathbf{J} = \mathbf{0}$. As a second step, in order to fall back onto the equations for the scattered field, we subtract the equations solved by the incident field (homogeneous Maxwell's equation with indices ε_b and μ_0), and use the relation $[\mathbf{E}_{tot}, \mathbf{H}_{tot}, \mathbf{P}_{tot}, \mathbf{J}_{tot}] = [\mathbf{E}_s + \mathbf{E}_{inc}, \mathbf{H}_s + \mathbf{H}_{inc}, \mathbf{P}_{tot}, \mathbf{J}_{tot}]$, to obtain the system solved by the scattered field:

$$\begin{cases} -i\omega\varepsilon_\infty \mathbf{E}_s + \mathbf{J}_{tot} - \nabla \times \mathbf{H}_s &= i\omega(\varepsilon_\infty - \varepsilon_b)\mathbf{E}_{inc}, \\ i\omega\mu_0 \mathbf{H}_s - \nabla \times \mathbf{E}_s &= \mathbf{0}, \\ -i\omega \dfrac{\omega_0^2}{\varepsilon_\infty \omega_p^2}\mathbf{P}_{tot} - \dfrac{\omega_0^2}{\varepsilon_\infty \omega_p^2}\mathbf{J}_{tot} &= \mathbf{0}, \\ \dfrac{i\omega}{\varepsilon_\infty \omega_p^2}\mathbf{J}_{tot} - \dfrac{\gamma}{\varepsilon_\infty \omega_p^2}\mathbf{J}_{tot} - \dfrac{\omega_0^2}{\varepsilon_\infty \omega_p^2}\mathbf{P}_{tot} + \mathbf{E}_s &= -\mathbf{E}_{inc}, \end{cases} \tag{3.22}$$

inside the resonator. Unlike the equations considered in Section 4, we can see that the source term on the right hand side of the equations is no longer confined to the first equation while the left hand side has not changed. The modal excitation coefficient α_m expressed in Eq. 3.6 is obtained after using the biorthogonal projection in Eq. 3.14. Since the source term differs slightly, we get a different formula from Eq. 3.5 even though the matrices $\widehat{\mathbf{K}}$ and $\widehat{\mathbf{M}}$ are the same in both cases.

Other formulas for α_m can be found by choosing a different distribution of the source over the four equations. This is the object of the next subsection.

3.4.2 Generalized source

Let us split the source term $\mathbf{J}$ into a set of artificial sources denoted $\mathbf{f}_1, \mathbf{f}_2, \mathbf{f}_3, \mathbf{f}_4$. We can rewrite the scattering problem thus:

$$\begin{cases} -i\omega\varepsilon_\infty \mathbf{E}_s + \mathbf{J}'_s - \nabla \times \mathbf{H}'_s &= \mathbf{f}_1, \\ i\omega\mu_0 \mathbf{H}'_s - \nabla \times \mathbf{E}_s &= \mathbf{f}_2, \\ -i\omega \dfrac{\omega_0^2}{\varepsilon_\infty \omega_p^2}\mathbf{P}'_s - \dfrac{\omega_0^2}{\varepsilon_\infty \omega_p^2}\mathbf{J}'_s &= \mathbf{f}_3, \\ \dfrac{i\omega}{\varepsilon_\infty \omega_p^2}\mathbf{J}'_s - \dfrac{\gamma}{\varepsilon_\infty \omega_p^2}\mathbf{J}'_s - \dfrac{\omega_0^2}{\varepsilon_\infty \omega_p^2}\mathbf{P}'_s + \mathbf{E}_s &= \mathbf{f}_4, \end{cases} \tag{3.23}$$

inside the resonator. By eliminating the unknowns $\mathbf{H}'_s$, $\mathbf{P}'_s$, $\mathbf{J}'_s$, we obtain the following equation for the scattered electric field $\mathbf{E}_s$:

$$\begin{aligned} -\omega^2\varepsilon(\omega)\mathbf{E}_s + \nabla \times \left(\frac{1}{\mu_0}\nabla \times \mathbf{E}_s\right) &= -i\omega\mathbf{f}_1 \\ +i\omega(\varepsilon(\omega) - \varepsilon_\infty)(i\omega\mathbf{f}_4 - \mathbf{f}_3) - \nabla \times \left(\frac{1}{\mu_0}\mathbf{f}_2\right), & \end{aligned} \tag{3.24}$$

which is equivalent to the standard second order Maxwell's equations:

$$-\omega^2\varepsilon(\omega)\mathbf{E}_s + \nabla\times\left(\frac{1}{\mu_0}\nabla\times\mathbf{E}_s\right) = -i\omega\mathbf{J}, \tag{3.25}$$

provided that

$$-i\omega\mathbf{f}_1 + i\omega(\varepsilon(\omega)-\varepsilon_\infty)(i\omega\mathbf{f}_4-\mathbf{f}_3) - \nabla\times\left(\frac{1}{\mu_0}\mathbf{f}_2\right) = -i\omega\mathbf{J}. \tag{3.26}$$

By choosing different splittings of the source (i.e. different fields $\mathbf{f}_1,\mathbf{f}_2,\mathbf{f}_3,\mathbf{f}_4$ that satisfy the relationship above), we will obtain different formulas for α_m given as

$$\begin{aligned}\alpha_m = \ & \frac{1}{i(\omega-\widetilde{\omega}_m)}\Big(\int_{\Omega_{res}} \mathbf{f}_1\cdot\widetilde{\mathbf{E}}_m + \mathbf{f}_2\cdot\widetilde{\mathbf{H}}_m \\ & +(\varepsilon(\widetilde{\omega}_m)-\varepsilon_\infty)\,(\mathbf{f}_3 - i\widetilde{\omega}_m\mathbf{f}_4)\cdot\widetilde{\mathbf{E}}_m\,d\Omega_{res}\Big).\end{aligned} \tag{3.27}$$

The modal expansion obtained with all these different formulas will converge towards the same electric field $\mathbf{E}_s$ when the number of modes increases. Since $i\omega\mu_0\mathbf{H}_s' = \nabla\times\mathbf{E}_s + \mathbf{f}_2$, it will also converge towards $\mathbf{H}_s' \neq \mathbf{H}_s$.

3.4.3 Derivation of (3.7)

In this section we propose a different linearization of the problem by starting from the second order formulation. With this alternative linearization, we obtain Eq. 3.7 for the coefficients α_m. Let us start from the second order formulation of Maxwell's equations described in equation Eq. 3.25. In order to linearize this equation, let us introduce the time-derivative of the scattered electric field $\mathbf{E}_s' = -i\omega\mathbf{E}_s$ and the auxiliary fields $\mathbf{J}_s = (\varepsilon(\omega)-\varepsilon_\infty)\mathbf{E}_s'$ and $\mathbf{J}_s' = -i\omega\mathbf{J}_s$. We obtain the following system of linear equations:

$$\begin{cases} -i\omega\mathbf{E}_s - \mathbf{E}_s' &= \mathbf{0}, \\ -i\omega\varepsilon_\infty\mathbf{E}_s' + \mathbf{J}_s' + \nabla\times\left(\frac{1}{\mu_0}\nabla\times\mathbf{E}_s\right) &= -i\omega\mathbf{J}, \\ -i\omega\mathbf{J}_s - \mathbf{J}_s' &= \mathbf{0}, \\ -i\omega\mathbf{J}_s' + \gamma\mathbf{J}_s' + \omega_0^2\mathbf{J}_s - \varepsilon_\infty\omega_p^2\mathbf{E}_s' &= \mathbf{0}, \end{cases} \tag{3.28}$$

,which gives the following stiffness and mass operators $\widehat{\mathbf{K}}$ and $\widehat{\mathbf{M}}$ for the vector $\mathbf{U} = [\mathbf{E}_s, \mathbf{E}_s', \mathbf{J}_s, \mathbf{J}_s']^T$:

$$\widehat{\mathbf{K}} = \begin{bmatrix} 0 & -1 & 0 & 0 \\ \mu_0^{-1}\nabla\times\nabla\times & 0 & 0 & 1 \\ 0 & 0 & 0 & -1 \\ 0 & -\varepsilon_\infty\omega_p^2 & \omega_0^2 & \gamma \end{bmatrix},$$

$$\widehat{\mathbf{M}} = \begin{bmatrix} 1 & 0 & 0 & 0 \\ 0 & \varepsilon_e & 0 & 0 \\ 0 & 0 & 1 & 0 \\ 0 & 0 & 0 & 1 \end{bmatrix}, \mathbf{F} = \begin{bmatrix} \mathbf{0} \\ -i\omega\mathbf{J} \\ \mathbf{0} \\ \mathbf{0} \end{bmatrix}. \tag{3.29}$$

Again, auxiliary fields $\mathbf{J}_s$ and $\mathbf{J}'_s$ only exist inside the resonator. Though the corresponding discrete matrices $\widehat{\mathbf{K}}_h$ and $\widehat{\mathbf{M}}_h$ are different this time, the discrete solution will be exactly the same with this formulation compared to the previous one mentioned in section 3.3. Since the matrix $\widehat{\mathbf{K}}_h$ is not symmetric, we do not have $\widetilde{\mathbf{x}}_m^{\perp} = \widetilde{\mathbf{x}}_m$ and must thus identify the different components of $\widetilde{\mathbf{x}}_m^{\perp}$ from the transpose eigenvalue problem. We obtain the following system of equation for the biorthogonal eigenvector, $\widetilde{\mathbf{x}}_m^{\perp} = [\widetilde{\mathbf{E}}_{m,\perp}, \widetilde{\mathbf{E}}'_{m,\perp}, \widetilde{\mathbf{J}}_{m,\perp}, \widetilde{\mathbf{J}}'_{m,\perp}]$:

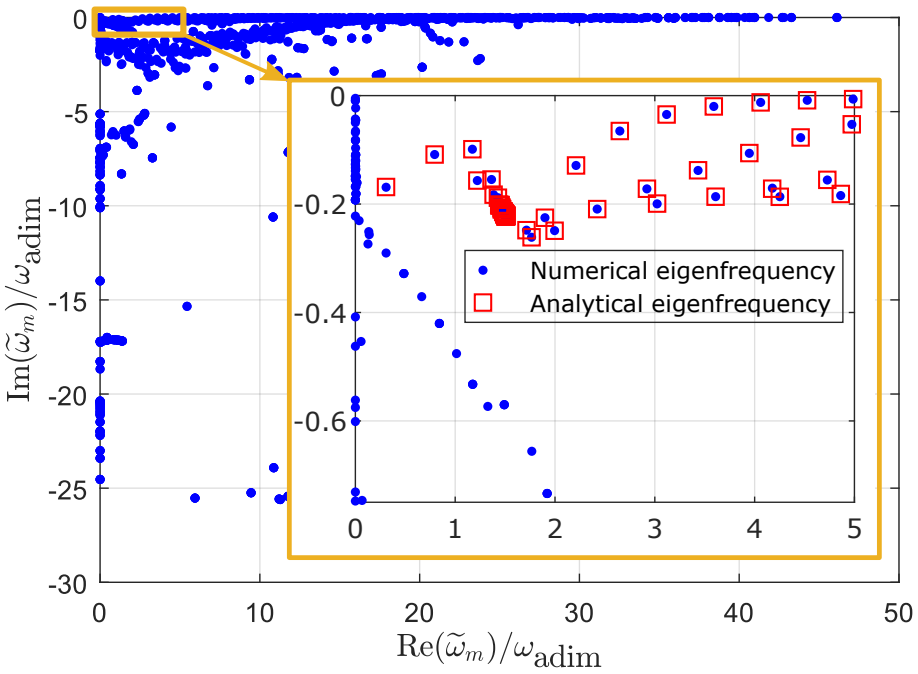

Figure 3.1: Numerical eigenfrequencies in the complex plane of the metallic wire. For each numerical eigenfrequency $\widetilde{\omega}_m$, we also find a mode on the opposite part of the complex plane whose eigenfrequency has the same imaginary part and the opposite real part. In the inset, we also plot the eigenfrequencies of the quasi-normal modes, computed analytically as red squares. The modes in the inset are included within a limited frequency range. $\omega_{adim} = 3 \cdot 10^{15}$ rad $\cdot$ s^{-1}.

$$\begin{cases} -i\widetilde{\omega}_m \widetilde{\mathbf{E}}_{m,\perp} + \nabla \times \left(\dfrac{1}{\mu_0} \nabla \times \widetilde{\mathbf{E}}'_{m,\perp} \right) &= \mathbf{0}, \\ -i\widetilde{\omega}_m \varepsilon_e \widetilde{\mathbf{E}}'_{m,\perp} - \varepsilon_\infty \omega_p^2 \widetilde{\mathbf{J}}'_{m,\perp} - \widetilde{\mathbf{E}}_m &= \mathbf{0}, \\ -i\widetilde{\omega}_m \widetilde{\mathbf{J}}_{m,\perp} + \omega_0^2 \widetilde{\mathbf{J}}'_{m,\perp} &= \mathbf{0}, \\ -i\widetilde{\omega}_m \widetilde{\mathbf{J}}'_{m,\perp} + \gamma \widetilde{\mathbf{J}}'_{m,\perp} + \widetilde{\mathbf{E}}'_{m,\perp} - \widetilde{\mathbf{J}}_{m,\perp} &= \mathbf{0}. \end{cases} \tag{3.30}$$

By eliminating the other variables, we can show that $\widetilde{\mathbf{E}}'_{m,\perp}$ verifies

$$-\widetilde{\omega}_m^2 \varepsilon(\widetilde{\omega}_m) \widetilde{\mathbf{E}}'_{m,\perp} + \nabla \times \left(\frac{1}{\mu_0} \nabla \times \widetilde{\mathbf{E}}'_{m,\perp} \right) = \mathbf{0}, \tag{3.31}$$

which is the second order Maxwell's eigenproblem, which the eigenvector $\widetilde{\mathbf{E}}_m$ is

a solution of. Subsequently we can identify the rest of the components of $\widetilde{\mathbf{x}}_m^{\perp}$:

$$\begin{cases} \widetilde{\mathbf{E}}'_{m,\perp} = \widetilde{\mathbf{E}}_m, \\ \widetilde{\mathbf{E}}_{m,\perp} = -i\widetilde{\omega}_m \varepsilon(\widetilde{\omega}_m)\widetilde{\mathbf{E}}_m, \\ \widetilde{\mathbf{J}}_{m,\perp} = \dfrac{\omega_0^2}{\omega_0^2 - i\gamma\widetilde{\omega}_m - \widetilde{\omega}_m^2}\widetilde{\mathbf{E}}_m, \\ \widetilde{\mathbf{J}}'_{m,\perp} = \dfrac{i\widetilde{\omega}_m}{\omega_0^2 - i\gamma\widetilde{\omega}_m - \widetilde{\omega}_m^2}\widetilde{\mathbf{E}}_m, \end{cases} \tag{3.32}$$

where $\widetilde{\mathbf{E}}_m$ is the electric field component of the right eigenvector $\widetilde{\mathbf{x}}_m$. We can now obtain the excitation coefficient:

$$\alpha_m = \frac{1}{i(\widetilde{\omega}_m - \omega)} \frac{\langle \mathbf{F}_h, \widetilde{\mathbf{x}}_m^{\perp} \rangle}{\langle \widehat{\mathbf{M}}_h \widetilde{\mathbf{x}}_m, \widetilde{\mathbf{x}}_m^{\perp} \rangle} = \frac{-i\omega \int_{\Omega_{res}} \mathbf{J}(\mathbf{r}, \omega) \cdot \widetilde{\mathbf{E}}_m d\mathbf{r}}{i(\widetilde{\omega}_m - \omega) N_m} \tag{3.33}$$

where the coefficient N_m appears since we chose the normalization Eq. 3.8 of the first order formulation. N_m is given as

$$\begin{aligned} N_m = \ & \langle \widehat{\mathbf{M}}_h \widetilde{\mathbf{x}}_m, \widetilde{\mathbf{x}}_m^{\perp} \rangle = -i\widetilde{\omega}_m \Big[\int_{\Omega} (\varepsilon(\widetilde{\omega}_m) + \varepsilon_e) \widetilde{\mathbf{E}}_m \cdot \widetilde{\mathbf{E}}_m \\ & + \frac{\varepsilon_\infty \omega_p^2}{(\omega_0^2 - i\gamma\widetilde{\omega}_m - \widetilde{\omega}_m^2)} (\omega_0^2 + \widetilde{\omega}_m^2) \widetilde{\mathbf{E}}_m \cdot \widetilde{\mathbf{E}}_m \, d\Omega \Big]. \end{aligned} \tag{3.34}$$

By using the relation $\widetilde{\mathbf{H}}_m = \dfrac{1}{i\omega\mu_0} \nabla \times \widetilde{\mathbf{E}}_m$ and the variational formulation satisfied by $\widetilde{\mathbf{E}}_m$, we have $-\int_\Omega \mu_0 \, \widetilde{\mathbf{H}}_m \cdot \widetilde{\mathbf{H}}_m \, d\Omega = \int_\Omega \varepsilon(\tilde{\omega}_m) \tilde{\mathbf{E}}_m \cdot \tilde{\mathbf{E}}_m \, d\Omega$. Straightforward derivation gives that $\dfrac{\partial \left(\tilde{\omega}_m \varepsilon(\tilde{\omega}_m) \right)}{\partial \tilde{\omega}_m} = \varepsilon_\infty + \varepsilon_\infty \omega_p^2 \dfrac{\tilde{\omega}_m^2 + \omega_0^2}{\left(\tilde{\omega}_m^2 + i\gamma\tilde{\omega}_m - \omega_0^2 \right)^2}$ inside the resonator. Therefore, we check that N_m is equal to the normalization (3.8) multiplied by $-i\widetilde{\omega}_m$. As a result, if $\widetilde{\mathbf{E}}_m$ is normalized by equation (3.8), we obtain $N_m = -i\widetilde{\omega}_m$, which gives us this expression for the excitation coefficient:

$$\alpha_m = \frac{\omega}{i\widetilde{\omega}_m(\widetilde{\omega}_m - \omega)} \int_{\Omega_{res}} \mathbf{J}(\mathbf{r}, \omega) \cdot \widetilde{\mathbf{E}}_m d\mathbf{r} \tag{3.35}$$

We recognize the formula in Eq. 3.7. We were able to obtain this formula with the use of the the biorthogonal projection and auxiliary fields unlike the way it is derived in [34].

3.4.4 Treatment of Degenerate Eigenvalues

A set of degenerate modes $\{\widetilde{\mathbf{x}}_k\}_{m_1 \leq k \leq m_2}$ are solutions of the eigenvalue problem at the same eigenfrequency $\widetilde{\omega}_{m_1}$. Degenerate eigenvectors do not necessarily form an orthogonal sub-basis with respects to $\widehat{\mathbf{M}}_h$. However, using a Gram-Schmidt orthogonalization process, an orthogonal sub-basis with respect to $\widehat{\mathbf{M}}_h$ can be constructed from a set of degenerate modes by algorithm 1.

By applying this procedure, Eq. 3.5 holds for degenerate eigenvalues with normalization Eq. 3.8.

Algorithm 1 Algorithm to apply Gram-Schmidt orthogonalization to vectors $\widetilde{\mathbf{x}}_m$

for $m = m_1$ to m_2 **do**
  Initialize $y = \widetilde{\mathbf{x}}_m$
  for $j = m_1$ to $m - 1$ **do**
    $\alpha \leftarrow \langle \widehat{\mathbf{M}}_h \widetilde{\mathbf{x}}_m, \widetilde{\mathbf{x}}_j^{\perp} \rangle$
    $y \leftarrow y - \alpha \widetilde{\mathbf{x}}_j$
  Compute left eigenvector $y^{\perp}$ from right eigenvector y using the transpose eigenvalue problem.
  $\widetilde{\mathbf{x}}_m \leftarrow y / \langle \widehat{\mathbf{M}}_h y, y^{\perp} \rangle$
  $\widetilde{\mathbf{x}}_j^{\perp} \leftarrow y^{\perp} / \langle \widehat{\mathbf{M}}_h y, y^{\perp} \rangle$

3.4.5 Case of metals: $\omega_0 = 0$

In section 3.3, the third equation of system Eq. 3.15 has been multiplied by $\omega_0^2/(\varepsilon_\infty \omega_p^2)$ which vanishes when $\omega_0 = 0$. In that case, the linear system Eq. 3.9 is no longer invertible because some rows of $\widehat{\mathbf{M}}$ and $\widehat{\mathbf{K}}$ are null. But this case is often interesting because it occurs for metallic materials, and we cannot symmetrize the linear system with our choice of auxiliary fields. Therefore the calculations made in section 3.3 are no longer valid for metals. However if we consider the non-symmetric system Eq. 3.17 with the following matrix,

$$\widehat{\mathbf{K}} = \begin{bmatrix} 0 & -\nabla\times & 0 & 1 \\ -\nabla\times & 0 & 0 & 0 \\ 0 & 0 & 0 & -1 \\ \varepsilon_\infty \omega_p^2 & 0 & \omega_0^2 & -\gamma \end{bmatrix},$$

$$\widehat{\mathbf{M}} = \begin{bmatrix} \varepsilon_\infty & 0 & 0 & 0 \\ 0 & -\mu_0 & 0 & 0 \\ 0 & 0 & 1 & 0 \\ 0 & 0 & 0 & -1 \end{bmatrix}. \tag{3.36}$$

The left eigenvector $\widetilde{\mathbf{x}}_m^{\perp}$ is not equal to $\widetilde{\mathbf{x}}_m$, but is given as:

$$\widetilde{\mathbf{x}}_m^{\perp} = \begin{bmatrix} \widetilde{\mathbf{E}}_m \\ \widetilde{\mathbf{H}}_m \\ \dfrac{\omega_0^2}{\varepsilon_\infty \omega_p^2} \widetilde{\mathbf{P}}_m \\ \dfrac{1}{\varepsilon_\infty \omega_p^2} \widetilde{\mathbf{J}}_m \end{bmatrix}. \tag{3.37}$$

As a result, we still obtain the modal excitation coefficient of Eq. 3.5 and the normalization of Eq. 3.8.

3.5 Numerical results

In this Section, we provide numerical tests to compare the convergence rate of the three formulas Eq. 3.5 (referred to as "Usual"), Eq. 3.6 (referred to as "Alternative source"), and Eq. 3.7 (referred to as "Order2"). The Usual and Alternative

Source formulas are implemented by taking a source term as explained in Sections 3.3 and 3.4. For formula Eq. 3.7, we did not implement matrices $\widehat{\mathbf{K}}_h$ and $\widehat{\mathbf{M}}_h$ introduced in section 5.C, but we use the discrete equivalent of Eq. 3.7.

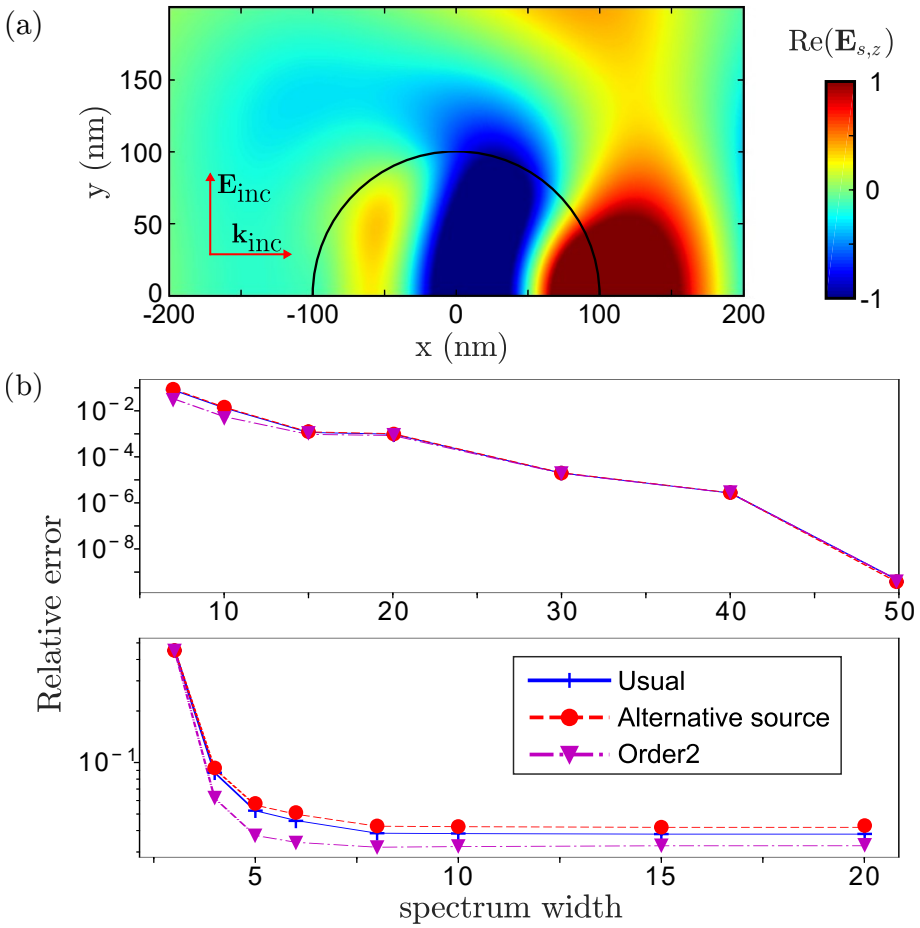

Figure 3.2: (a) Real part of the scattered electric field for $\omega = 3\omega_0/2$ computed with the direct FEM. The relative error between the FEM and analytical solutions is 0.15%. The cylinder is illuminated by a plane wave propagating along the x-axis and polarized parallel to the cylinder axis. (b) Relative error between the scattered field computed with the modal expansion and with the direct FEM solver as a function of the width of the spectral for the three formulas. Top panel: the error is computed over the whole physical domain and all modes (QNMs+PML modes) are retained in the expansion. Bottom panel: the error is computed over the cylinder interior and only modes with $\text{Im}(\omega) \geq -3 \cdot 10^{15}$ rad $\cdot$ s^{-1} are retained, therein preferentially selecting QNMs and removing PML modes.

Two simple geometries, a 2D cylinder and a 3D spheres for which analytical solutions exist, are considered for the comparison. All the numerical results are obtained with the finite element software Montjoie [48] for the computation of the finite matrices $\widehat{\mathbf{M}}_h$ and $\widehat{\mathbf{K}}_h$ given in section 3.2. The eigenfrequencies ω_m of the matrix $\widehat{\mathbf{M}}_h^{-1}\widehat{\mathbf{K}}_h$ are computed with Lapack [66]. All the eigenvalues such that $|\widetilde{\omega}_m| < 10^{-3}\omega_{\text{adim}}$ are dropped in order to remove static modes. These static modes are not included because they are too numerous. Only modes with $\text{Re}(\widetilde{\omega}_m) \geq 0$ are computed but the complex-conjugate modes with $\text{Re}(\omega) < 0$ are

also considered for the reconstruction. Finally, if two eigenfrequencies $\widetilde{\omega}_i$ and $\widetilde{\omega}_j$ are close enough (i.e. $|\widetilde{\omega}_i - \widetilde{\omega}_j| < 10^{-6}\omega_{\text{adim}}$), they are considered degenerate.

For simplicity, the Maxwell's equations are adimensionalized with $\omega_{\text{adim}} = 3 \cdot 10^{15}\text{rad} \cdot \text{s}^{-1}$ such that the numerical eigenvalues are in the range of 1.

3.5.1 Two-dimensional example : Infinite metallic wire

We first consider the field scattered by a cylindrical wire with a radius of 100 nm in air. The metallic wire is modeled with a Drude-Lorentz permittivity with $\varepsilon_\infty = 6, \omega_0 = 4.572 \cdot 10^{15}\text{rad/s}, \omega_p = \frac{\omega_0}{2}, \gamma = 1.332 \cdot 10^{15}\text{rad/s}$. The wire axis is denoted by the coordinate z.

The physical computational domain is 400 nm long and 200 nm wide. 100-nm-thick perfectly matched layers are added at the edges of the physical domain. The field driving the system is a TE-polarized plane wave propagating along the x-axis, at the real frequency ω. As a result, only the z-component E_z of the electric field is non null and is discretized with continuous finite elements.

Figure 3.1 shows the eigenfrequencies $\widetilde{\omega}_m$ computed with Montjoie and compare them with analytical values obtained with Hankel functions. We see that the QNMs are correctly computed and that we compute a significant amount of other modes, referred to as PML modes [30, 32]. Note the existence of one accumulation point corresponding to the pole of the permittivity $\varepsilon(\omega)$ of the cylinder. The matrices $\widehat{\mathbf{M}}_h$ and $\widehat{\mathbf{K}}_h$ have 5300 rows. Among the 1798 eigenvectors stored, 286 correspond to degenerate modes. The presence of degenerate eigenvalues can be due to accumulation points or symmetry in the PML layout.

We represent in Fig. 3.1 the eigenfrequencies $\widetilde{\omega}_m$ of the cylinder. We can see that the QNMs are correctly computed and that we compute a significant amount of other modes, referred to as PML modes. We can distinguish them from QNMs by either observing their field profile (PML modes usually have a large field magnitude inside the PMLs). The ratio of the field intensity inside the PML over the intensity inside the physical domain is a decent criterion to distinguish QNMs and PML modes. Another way to distinguish them would be to perform the same eigenmode search with different PML parameters. The QNMs would see their eigenfrequencies barely affected while PML modes eigenfrequencies would shift significantly. The matrices $\widehat{\mathbf{M}}_h$ and $\widehat{\mathbf{K}}_h$ have 5300 rows. Among the 1798 eigenvectors stored, 286 correspond to degenerate modes. The presence of degenerate eigenvalues can be due to accumulation points or symmetry in the PML layout.

In Fig. 3.2, we display the relative error between the modal expansion of the scattered field

$$\mathbf{E}_s^{modal} = \sum_m^N \alpha \widetilde{\mathbf{E}}_m \tag{3.38}$$

and the direct FEM solution:

$$\mathbf{E}_s^{FEM} = (-i\omega\widehat{\mathbf{M}}_h + \widehat{\mathbf{K}}_h)^{-1}\mathbf{F}_h \tag{3.39}$$

as a function of the width L of the spectral interval covered by the eigenmodes retained in the expansion. We compare the error between inversing the matrix

directly (direct FEM solution), and using the modal expansion for a limited number N of eigenmodes. For a given L, the retained modes satisfy two conditions: they are contained within a rectangular section of the complex plane, defined by $\mathrm{Re}(\widetilde{\omega}_m) \in [-L\,\omega_{\mathrm{adim}}, L\,\omega_{\mathrm{adim}}]$ and the mode eigenfrequency is such that $\mathrm{Im}(\widetilde{\omega}_m) \in [-\omega_{\mathrm{adim}}\,L/2, 0]$.

The relative error defined by

$$\text{Relative Error} = \sqrt{\frac{\int_{\Omega_p} \left|\mathbf{E}_s^{modal} - \mathbf{E}_s^{FEM}\right|^2 d\mathbf{r}}{\int_{\Omega_p} \left|\mathbf{E}_s^{FEM}\right|^2 d\mathbf{r}}}, \tag{3.40}$$

is computed for 31 frequencies, evenly spaced in the interval $[\omega_0/2, 2\omega_0]$, and the maximum value of the error is retained and plotted. Two domains Ω_p will be considered.

The main result of the comparison is shown in the upper inset of Fig. 3.2.b, where it is shown that the three formulas converge towards the direct FEM solution, as expected, with similar convergence rates. The Usual and Alternative source formulas are very close, while the Order2 formula is a bit more accurate when the spectral width L is small. We note that, for $L = 15$, the relative error is 0.1 %, a value comparable to the difference between the FEM solution and the analytical solution calculated with Hankel functions. To achieve very good accuracy, very high frequency modes have to be retained in the expansion. Let us finally point out that the reconstruction is performed over the entire physical domain, i.e. Ω_p is the domain formed by the cylinder and the air background (the PML is not included).

In the bottom panel of Fig. 3.2.b, we have also displayed the relative error computed while retaining only the modes whose eigenfrequency's imaginary parts are small: $\mathrm{Re}(\widetilde{\omega}_m) \in [-L\omega_{\mathrm{adim}}, L\omega_{\mathrm{adim}}]$ and $\mathrm{Im}(\widetilde{\omega}_m) \in [-\omega_{\mathrm{adim}}, 0]$. With this criterion, we expect to retain mostly QNMs in the expansion [32], and thus to test the convergence without PML modes. Additionally, since the QNM basis is complete only in the interior of the resonator [31], the reconstruction is performed in a domain Ω_p restricted to the cylinder interior.

3.5.2 Three-dimensional example : Metallic Sphere

We further consider a metallic sphere with a permittivity described by the same Drude-Lorentz model and a radius of 100 nm. The sphere is illuminated by a plane wave propagating along the z-axis and polarized parallel to the x-axis.

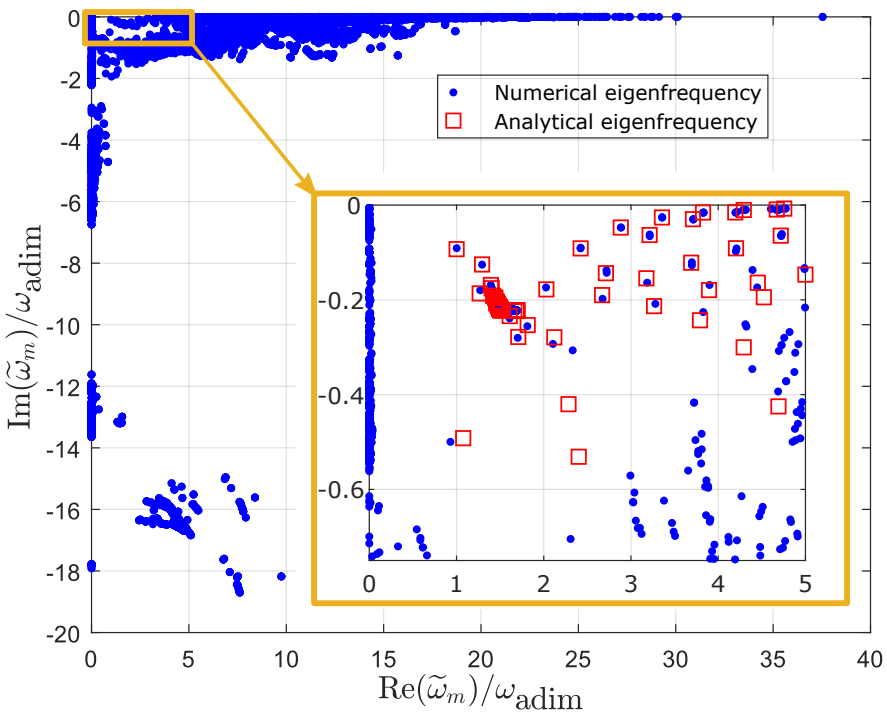

Figure 3.3: Numerical eigenfrequencies in the complex plane for the metallic sphere with a Drude permittivity. In the inset, we also plot the eigenfrequencies (red squares) of the quasinormal modes, computed analytically with Mie's theory. The modes in the inset are included within a limited frequency range. $\omega_{adim} = 3 \cdot 10^{15}$ rad $\cdot$ s^{-1}.

Owing to symmetry, we only mesh one quarter of numerical space. The latter is composed of physical domain, a [0,150 nm]×[0,150 nm]×[-150 nm,150 nm] parallelepiped box surrounded by a 100 nm-thick PML layers. We impose a Perfectly conducting condition on plane $x = 0$ (i.e. $\mathbf{E} \times \mathbf{n} = 0$) and a Neumann condition on plane $y = 0$ (i.e. $\mathbf{H} \times \mathbf{n}$). Fourth order edge elements are used for the unknown $\mathbf{E}$ and the mesh. For this case, the matrices $\widehat{\mathbf{M}}_h$ and $\widehat{\mathbf{K}}_h$ have 31246 rows. Among the 8055 stored eigenvectors, 919 are degenerate.

The computed eigenfrequencies are plotted in Fig. 3.3. The inset shows a subdomain of the complex plane and Mie analytical eigenfrequencies corresponding to QNMs only. Since the mesh is much coarser in this 3D example, some QNMs are not correctly approximated (the relative error between the direct FEM solver results and the analytical Mie solution is around 4%). We have two accumulation points, one for $\widetilde{\omega}_m = (1.5088 - 0.2221i)\omega_{\mathrm{adim}}$ which corresponds to the pole of $\varepsilon(\omega)$ and one for the zero of $\varepsilon(\omega)$ at $\widetilde{\omega}_m = (1.6905 - 0.2221i)\omega_{\mathrm{adim}}$.

We again consider 31 angular frequencies ω evenly spaced in the interval $[\omega_0/2, 2\omega_0]$ and compute the relative error between the modal solution and the direct FEM solution. However, to circumvent the issue of static modes, the relative error is computed with the curl of $\mathbf{E}$

$$\text{Relative Error} = \sqrt{\frac{\int_{\Omega_p} \left| \nabla \times \mathbf{E}_s^{modal} - \nabla \times \mathbf{E}_s^{FEM} \right|^2 d\mathbf{r}}{\int_{\Omega_p} \left| \nabla \times \mathbf{E}_s^{FEM} \right|^2 d\mathbf{r}}}. \tag{3.41}$$

The error is plotted in Fig. 3.4 for the three formulas. Essentially, the same conclusions as in the 2D case hold. The three formulas provide a modal solution that converges towards the direct FEM solution. When the width L of the spectral interval is small, formula (3.7) is slightly more accurate. However, in contrast to the previous case, we have to choose $L \approx 7.5$ to achieve a relative error of 4 % (which is the error between the FEM solution and the analytical solution). In order for the modal expansion to well converge, high frequency modes are once again necessary.

If the electric field, rather than its curl, is desired, the formulas in Eq. 3.7, 3.6 and 3.5 cannot be used owing to the large number of static modes. A nice approach consists in discretizing $\mathbf{H}$ with edge elements (instead of $\mathbf{E}$), and to reconstruct $\mathbf{H}_s$ with the modal expansion $\mathbf{H}_s^{modal} = \sum_m \alpha_m \widetilde{\mathbf{H}}_m$. $\mathbf{E}_s$ can be obtained through Maxwell's equations

$$\mathbf{E}_s^{modal} = \frac{1}{-i\omega\varepsilon(\omega)}(\mathbf{J} + \nabla \times \mathbf{H}_s^{modal}). \tag{3.42}$$

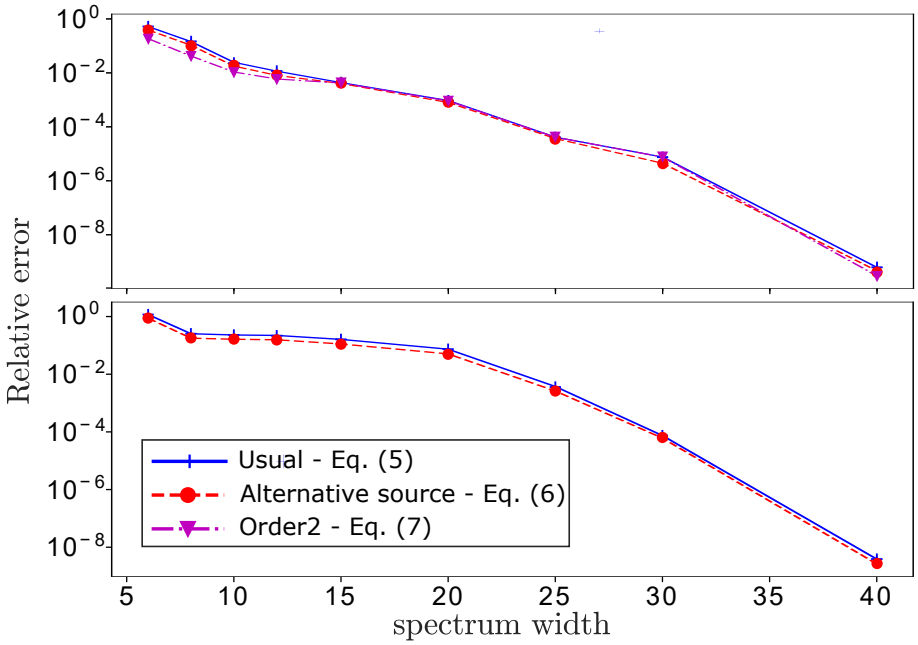

Figure 3.4: Top: Relative error on the curl of $\mathbf{E}_s$ versus the spectral width of the modes included in the modal expansion for the case of the metallic sphere. Bottom: Relative error on $\mathbf{E}_s$ versus the spectral width of the modes included in the modal expansion for the case of the metallic sphere. $\mathbf{E}_s$ is obtained from the curl of $\mathbf{H}_s$, which is obtained using the modal expansion. In both cases, the error is computed over the physical domain.

With this approach, static modes are ignored ($\widetilde{\omega}_m << \omega$), and the reconstructed field converges to the correct solution.

In the lower panel of Fig. 3.4, the relative error on the electric field has been computed by using Eq. 3.42. Only the formulas Eq. 3.5 and Eq. 3.6 can be considered to obtain $\mathbf{H}_s^{modal}$ with the coefficients α_m. The modal excitation coefficient given by formula Eq. 3.7 can be used only to reconstruct $\mathbf{E}_s^{modal}$, since the magnetic field was not introduced during the derivation of the formula.

In the lower panel of Fig. 3.4, we observe that the reconstructed field $\mathbf{E}_s$ with this method converges correctly to the numerical electric field. However, the accuracy obtained on $\mathbf{E}_s$ is not as good as the accuracy obtained for $\mathbf{H}_s$ in the upper panel of Fig. 3.4.

In this section we have shown that the reconstructed field converges towards the numerical solution. However, the convergence was achieved with a high spectral width which corresponds not only to a high number of modes, but also to modes whose resonance frequencies are high. In those cases, high frequency modes are necessary to achieve convergence of the modal expansion towards the direct FEM results even though their resonance frequency is almost 10 times greater than the maximum frequency on which the error on the field was computed, in spite of their small linewidth. The combined contribution of these non-resonant high frequencies allow the expansion to converge. We have also seen that numerical modes, also called PML modes, with very large linewidths also have an important effect on the overall convergence of the expansion, as previously discussed in [30].

In summary, we have discussed how scattered fields can be computed from the discrete eigenmodes of Maxwell's equations. Due to the discrete nature of the problem, these discrete eigenmodes form a complete basis meaning the numerical solution can be written exactly as a combination of the eigenmodes. Despite the discretization, there is no uniqueness of the modal expansion coefficients. We have shown that, in fact, an infinity of formulas exists for the expansion coefficients. Even new formulas can be found by choosing a different linearization of the dispersive Maxwell's equations or different equivalent source terms. With our common formalism, we have been able to recover 3 different formulas among others that have been proposed in the recent literature. Our numerical tests, obtained for simple geometries, do not provide conclusive observations on which formula provides the better convergence. We also explain how degenerate eigenvalues are treated with a simple Gram-Schmidt orthogonalization. This procedure is essential in order to construct an orthogonal basis of eigenmodes with respect to the mass matrix $\widehat{\mathbf{M}}_h$, which can be seen as a non-classical scalar product. Furthermore, an indirect important consequence of the present work that we would like to emphasize in this conclusion is that, with certain symmetric formulations of Maxwell's equations that there is no need to compute the left eigenvectors as they can be computed from the right eigenvectors. However, in more complex cases such as gratings with quasi-periodic conditions where the Maxwell's equations are no longer symmetric, the computation of the left eigenvector is required[35].

Chapter 4

Quasinormal mode reconstruction of the electromagnetic fields of gratings

The efficiencies of gratings as a function of the wavelength may present peaks, dips or anomalies generated by the excitation of leaky photonic of plasmonic modes. This is well known since U. Fano introduced a surface- plasmon model to analyze light diffraction by metallic gratings and explained Wood's anomalies [67].Nowadays, grating resonances have many applications for biosensing, photodetectors, photovoltaics, light emission, optical processing, metamaterials ... and their theoretical analysis for harnessing light-matter interaction remains of great importance. The theory of grating anomalies was pioneered by a milestone work by Hessel and Oliner [68] and was then followed by a series of works summarized in Refs. [69, 70, 24], which contributed to the systematic development of a phenomenological study of grating anomalies through the poles and zeros of the scattering operator, the so-called "pology". Poles were indifferently computed by considering a real frequency ω (equal to the driving laser frequency) and looking for complex in-plane wave-vectors $\widetilde{k}(\omega)$ or angles of incidence $sin(\widetilde{\theta}(\omega))$, or by considering a fixed angle of incidence θ, and looking for complex frequencies $\widetilde{\omega}(\theta)$. Great insight in the physics of grating anomalies was achieved by tracking the pole trajectories in the complex plane as some parameters, e.g. the grating depth, are tuned [70].The frequency poles $\widetilde{\omega}$, , i.e. the natural resonances, have a profound meaning (these poles correspond to the quasinormal-modes or QNMs hereafter). They define important quantities such as the resonance frequency, $\mathrm{Re}(\widetilde{\omega})$, or the inverse of the mode lifetime, $2\mathrm{Im}(\omega)$. The theory of grating anomalies changed little during several decennia, and the pology has been used to analyze or engineer various anomalous grating effects [71]. In 2014, Vial and his colleagues published a paper that contains many important results [32]. Assuming one-dimensional gratings made of nondispersive materials, they computed many QNMs (poles) at complex frequencies, then normalized the QNMs and computed their excitation coefficients, to finally reconstruct the field scattered by an incident plane wave in the QNM basis. The formalism was subsequently used to design spectral filters in the infrared [72]. The new possibilities offered by the availability of stable methods to normalize QNMs were also exploited for deriving closed-form expressions of the changes of grating resonance frequency and linewidth due to tiny refractive index changes [73, 74]. Recently, several numerical methods to compute and normalize the QNMs of

plasmonic nanoresonators, including metal gratings and plasmonic crystals, were successfully benchmarked, establishing standards for the computation and normalization of QNMs of dispersive resonators [64].These initiatives are part of broader, more comprehensive studies on QNM-expansion formalisms for analyzing light interaction with resonances of open non-Hermitian electromagnetic systems [14], which are presently knowing rapid progresses [30].

However, most recent works on the modes of gratings compute quasinormal modes for fixed in-plane Bloch wave vector k_p whose physical relevance is extrapolated to fit with grating experiments where the angle of incidence θ is usually fixed while the wavelength of the impinging light changes. In order to compute modes that correspond to the reality of grating experiments, we decide to compute modes that would correspond to the fixed incident direction experiments. This ends up changing many things, from the pseudo-periodicity conditions to the normalization and excitation coefficients.

4.1 Problem definition: wave scattering on a grating

We consider the following scattering problem. A linearly polarized plane wave is impinging upon either a one-dimensional or two-dimensional grating with an angle of incidence θ and an azimuthal angle φ. For this chapter, the convention $\exp(-i\omega t)$ is assumed for time-harmonic fields.

Using the Rayleigh expansion [75, 76], the total field in the lower and upper half planes can be expressed as a sum of plane waves:

$$\begin{cases} \mathbf{E}_{tot,I} = \mathbf{E}_{inc} + \sum_j r_j \exp\left(i\left(k^r_{j,x}x + k^r_{j,y}y + k^r_{j,z}z\right)\right), \\ \mathbf{E}_{tot,II} = \sum_j t_j \exp\left(i\left(k^t_{j,x}x + k^t_{j,y}y + k^t_{j,z}z\right)\right), \end{cases} \tag{4.1}$$

where r_j and t_j are the complex amplitudes of the j^{th} reflected and transmitted order respectively, and $k^r_{j,x}, k^r_{j,y}, k^r_{j,z}$ are the x-,y-,z-components of the j^{th} order reflected plane wave's wavevector and $k^t_{j,x}, k^t_{j,y}, k^t_{j,z}$ are the x-,y-,z-components of the j^{th} order transmitted plane wave's wavevector.

In the scattering fields formulation, the scattered field is a solution of Maxwell's equation for the permittivity distribution of the periodic structure $\varepsilon = \varepsilon_b + \Delta\varepsilon$, where ε_b is the background permittivity and $\Delta\varepsilon$ a permittivity perturbation, usually corresponding to the resonator in cases where ε_b is uniform. The incident field $\mathbf{E}_{inc}$ spawns the driving field $\mathbf{E}_d$ which is a solution of Maxwell's equations for ε_b.

The total field of the system is thus written in the scattering field formulation as

$$\mathbf{E}_{tot} = \mathbf{E}_s + \mathbf{E}_d \tag{4.2}$$

This leads to a direct relationship between the modal reconstruction of the scattered field and the field in the upper and lower half plane. In the case of the field in the upper half plane, we have

$$\mathbf{E}_{tot} = \sum_m \alpha_m \widetilde{\mathbf{E}}_m + \mathbf{E}_d = \mathbf{E}_{inc} + \sum_j r_j \exp(i(k^r_{j,x}x + k^r_{j,y}y + k^r_{j,z}z)). \tag{4.3}$$

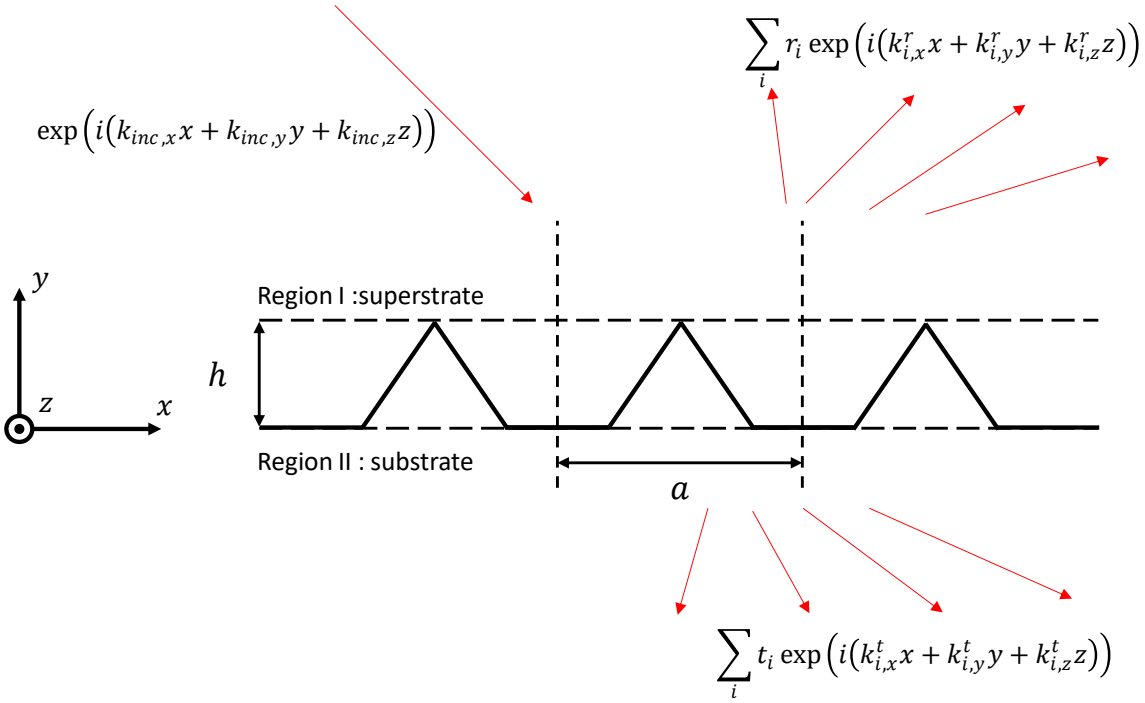

Figure 4.1: The scattered field of the grating illuminated by a plane wave is made up of a superposition of plane waves in the superstrate and substrate regions of space.

4.2 Quasinormal mode expansion of the scattered field of gratings

4.2.1 Two types of modes, different normalizations

Consider a grating that is periodic along the x and z directions, and a typical scattering problem in which the grating is illuminated by a plane wave with a direction of incidence defined by having $\mathbf{k}_p = \frac{n_i\omega}{c}[\sin(\theta)\cos(\varphi)\hat{\mathbf{x}} + \sin(\theta)\sin(\varphi)\hat{\mathbf{z}}]$, where θ and φ are the angular components of the spherical coordinates that specify the incident angles in a medium with refractive index n_i assumed to be non-dispersive). We can see that $\mathbf{k}_p$ changes with the frequency ω. Due to the periodic nature of the problem, it is convenient to employ Bloch's theorem. We can express the scattered field of the system $[\mathbf{H}_s(\mathbf{r},\omega), \mathbf{E}_s(\mathbf{r},\omega)] = [\mathbf{h}_s(\mathbf{r},\omega), \mathbf{e}_s(\mathbf{r},\omega)]\exp(i\mathbf{k}_p \cdot \mathbf{r})$ where $\mathbf{h}_s$ and $\mathbf{e}_s$ are periodic functions with the same periodicity as the grating.

Derivation of the Normalisation and excitation of $\mathbf{k}_p$ modes

We fix the value of the parameter $\mathbf{k}_p$. We can expand the scattered field on the fixed-$\mathbf{k}_p$ QNMs by $[\widetilde{\mathbf{H}}_k(\mathbf{r}), \widetilde{\mathbf{E}}_k(\mathbf{r})] = [\widetilde{\mathbf{h}}_k(\mathbf{r}), \widetilde{\mathbf{e}}_k(\mathbf{r})]\exp(i\mathbf{k}_p \cdot \mathbf{r})$, $\widetilde{\mathbf{h}}_k(\mathbf{r})$ and $\widetilde{\mathbf{e}}_k(\mathbf{r})$ also being periodic functions with the same periodicity as the grating. $[\widetilde{\mathbf{H}}_k(\mathbf{r}), \widetilde{\mathbf{E}}_k(\mathbf{r})]$ solves the regular source-free Maxwell's equations at the complex frequency $\widetilde{\omega}_k$, but we can rewrite the equations for the Bloch field $[\widetilde{\mathbf{h}}_k(\mathbf{r}), \widetilde{\mathbf{e}}_k(\mathbf{r})]$ using the vectorial relation $\nabla \times (f(\mathbf{r})\mathbf{A}(\mathbf{r})) = f(\mathbf{r})\nabla \times \mathbf{A}(\mathbf{r}) + \nabla f(\mathbf{r}) \times \mathbf{A}(\mathbf{r})$, where $f(\mathbf{r})$ is a

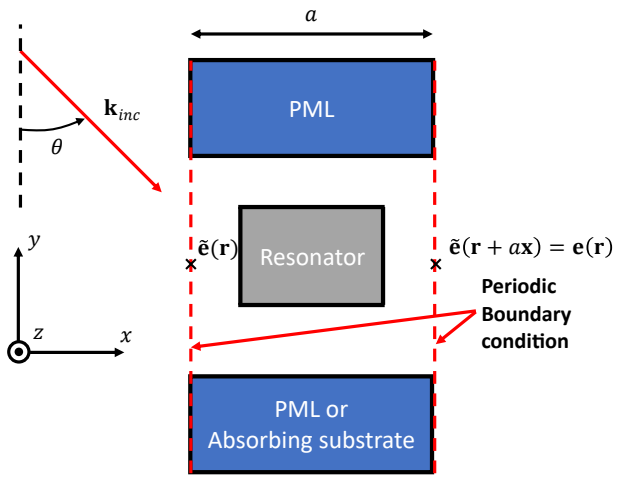

Figure 4.2: Basic schematic of the unit cell for a one-dimensional grating.

scalar function and $\mathbf{A}(\mathbf{r})$ is a field:

$$\begin{cases} \nabla \times \widetilde{\mathbf{e}}_k(\mathbf{r}) = -i\mathbf{k}_p \times \widetilde{\mathbf{e}}_k(\mathbf{r}) + i\widetilde{\omega}_m \mu_0 \widetilde{\mathbf{h}}_k(\mathbf{r}), \\ \nabla \times \widetilde{\mathbf{h}}_k(\mathbf{r}) = -i\mathbf{k}_p \times \widetilde{\mathbf{h}}_k(\mathbf{r}) - i\widetilde{\omega}_m \varepsilon(\mathbf{r}) \widetilde{\mathbf{e}}_k(\mathbf{r}). \end{cases} \tag{4.4}$$

We can rewrite this equation into an eigenvalue problem $\widehat{\mathbf{K}}_k \widetilde{\mathbf{x}}_k = i\widetilde{\omega}_k \widehat{\mathbf{M}}_k \widetilde{\mathbf{x}}_k$ with

$$\widehat{\mathbf{K}}_k = \begin{bmatrix} 0 & (\nabla\times) - (i\mathbf{k}_p\times) \\ (\nabla\times) - (i\mathbf{k}_p\times) & 0, \end{bmatrix}, \widehat{\mathbf{M}}_k = \begin{bmatrix} \mu_0 & 0 \\ 0 & -\varepsilon, \end{bmatrix}, \widetilde{\mathbf{x}}_k = \begin{bmatrix} \widetilde{\mathbf{h}}_k \\ \widetilde{\mathbf{e}}_k \end{bmatrix}. \tag{4.5}$$

By fixing the value of the parallel wavevector $\mathbf{k}_p$, $\mathbf{k}_p\times$ being an unvarying operator with regards to frequency, it can be included inside the matrix $\widehat{\mathbf{K}}_k$. As in the previous chapters, the left eigenvector $\widetilde{\mathbf{x}}_k^{\perp} = [\widetilde{\mathbf{h}}_k^{\perp}(\mathbf{r}), \widetilde{\mathbf{e}}_k^{\perp}(\mathbf{r})]$ is found by searching for the right eigenvector of the transpose problem, which is written thus:

$$\begin{cases} \nabla \times \widetilde{\mathbf{e}}_k^{\perp}(\mathbf{r}) = +i\mathbf{k}_p \times \widetilde{\mathbf{e}}_k^{\perp}(\mathbf{r}) + i\widetilde{\omega}_m \mu_0 \widetilde{\mathbf{h}}_k^{\perp}(\mathbf{r}) = -i(-\mathbf{k}_p) \times \widetilde{\mathbf{e}}_k^{\perp}(\mathbf{r}) + i\widetilde{\omega}_m \mu_0 \widetilde{\mathbf{h}}_k^{\perp}(\mathbf{r}), \\ \nabla \times \widetilde{\mathbf{h}}_k^{\perp}(\mathbf{r}) = +i\mathbf{k}_p \times \widetilde{\mathbf{h}}_k^{\perp}(\mathbf{r}) - i\widetilde{\omega}_m \varepsilon \widetilde{\mathbf{e}}_k^{\perp}(\mathbf{r}) = -i(-\mathbf{k}_p) \times \widetilde{\mathbf{h}}_k^{\perp}(\mathbf{r}) - i\widetilde{\omega}_m \varepsilon \widetilde{\mathbf{e}}_k^{\perp}(\mathbf{r}). \end{cases} \tag{4.6}$$

It is evident that $\widetilde{\mathbf{x}}_k^{\perp} = [\widetilde{\mathbf{h}}_{-k}(\mathbf{r}), \widetilde{\mathbf{e}}_{-k}(\mathbf{r})]$, which is the QNM field obtained with the opposite in-plane Bloch wavevector $-\mathbf{k}_p$.

This leads to the following normalization of fixed-$-\mathbf{k}_p$ Bloch QNM modes for materials with non-dispersive permittivity distribution $\varepsilon(\mathbf{r})$:

$$\langle \widehat{\mathbf{M}}_k \widetilde{\mathbf{x}}_{-k}, \widetilde{\mathbf{x}}_k \rangle = \int_\Omega \widetilde{\mathbf{e}}_k(\mathbf{r}) \cdot \varepsilon(\mathbf{r}) \widetilde{\mathbf{e}}_{-k}(\mathbf{r}) - \widetilde{\mathbf{h}}_k(\mathbf{r}) \cdot \mu_0 \widetilde{\mathbf{h}}_{-k}(\mathbf{r}) d^3\mathbf{r} = 1, \tag{4.7}$$

and the following excitation coefficient:

$$\alpha_k = -\frac{1}{\omega - \widetilde{\omega}_k} \int_{\Omega_{res}} \mathbf{J}(\mathbf{r}, \omega) \cdot \widetilde{\mathbf{e}}_{-k}(\mathbf{r}) d^3\mathbf{r} = 1. \tag{4.8}$$

The normalization and excitation coefficients can also be demonstrated by applying the divergence theorem to the modes $[\widetilde{\mathbf{H}}_k(\mathbf{r}), \widetilde{\mathbf{E}}_k(\mathbf{r})]$ and $[\widetilde{\mathbf{H}}_{-k}(\mathbf{r}), \widetilde{\mathbf{E}}_{-k}(\mathbf{r})]$, while assuming that these modes are orthogonal.

Since the pseudoperiodicity parameter $\mathbf{k}_p$ is fixed, most Maxwell eigenmode solvers with integrated pseudo-periodic conditions will be able to compute the corresponding Bloch QNMs, like COMSOL Multiphysics [77] for example using its default Electromagnetic Wave simulation with the RF module. However, due to the relation between $\mathbf{k}_p$ and the frequency and direction of the incident plane wave, fixed-$\mathbf{k}_p$ modes are only valid for that specific non-null value of $\mathbf{k}_p$ which corresponds to functional combinations of ω, θ, and ϕ. This would translate into an experiment where the beam impinging upon the grating would need to rotate to specific angles for every change in wavelength. These modes do not represent the usual protocol of grating experiments where the direction of the incident beam is fixed, and the spectra is scanned. This is the framework that $\boldsymbol{\eta}$-modes represent.

Derivation of normalization for fixed $\boldsymbol{\eta}$-modes

Consider the same grating experiment as in the previous part. This time, the modes of the system are not computed for a fixed parallel momentum but instead a fixed "directionality" vector $n_i[sin(\theta)cos(\varphi)\hat{\mathbf{x}} + sin(\theta)sin(\varphi)\hat{\mathbf{z}}]$, which is set by the direction of the incident plane wave, described by the two angles θ and φ. The scattered field can thus be rewritten as

$$[\mathbf{H}_s(\mathbf{r},\omega), \mathbf{E}_s(\mathbf{r},\omega)] = [\mathbf{h}_s(\mathbf{r},\omega), \mathbf{e}_s(\mathbf{r},\omega)] \exp(i\frac{\omega}{c}\boldsymbol{\eta}\cdot\mathbf{r}).$$

The Bloch QNM fields of the system will this time be denoted by $[\mathbf{H}_\eta(\mathbf{r}), \mathbf{E}_\eta(\mathbf{r})] = [\mathbf{h}_\eta(\mathbf{r}), \mathbf{e}_\eta(\mathbf{r})]\exp(i\frac{\omega}{c}\boldsymbol{\eta}\cdot\mathbf{r})$, $\mathbf{h}_\eta(\mathbf{r})$ and $\mathbf{e}_\eta(\mathbf{r})$ also being periodic functions with the same periodicity as the grating. $[\mathbf{H}_\eta(\mathbf{r}), \mathbf{E}_\eta(\mathbf{r})]$ is a solution to the source free Maxwell's equations at the complex frequency $\widetilde{\omega}_\eta$. In the same manner as before we can write the following set of equations for the Bloch field$[\mathbf{h}_\eta(\mathbf{r}), \mathbf{e}_\eta(\mathbf{r})]$.

$$\begin{cases} \nabla\times\widetilde{\mathbf{e}}_\eta(\mathbf{r}) = -i\dfrac{\widetilde{\omega}_\eta}{c}\boldsymbol{\eta}_p\times\widetilde{\mathbf{e}}_\eta(\mathbf{r}) + i\widetilde{\omega}_m\mu_0\widetilde{\mathbf{h}}_\eta(\mathbf{r}) = i\widetilde{\omega}_\eta\left(\mu_0\widetilde{\mathbf{h}}_\eta(\mathbf{r}) - \dfrac{1}{c}\boldsymbol{\eta}_p\times\widetilde{\mathbf{e}}_\eta(\mathbf{r})\right), \\ \nabla\times\widetilde{\mathbf{h}}_\eta(\mathbf{r}) = -i\dfrac{\widetilde{\omega}_\eta}{c}\boldsymbol{\eta}_p\times\widetilde{\mathbf{h}}_\eta(\mathbf{r}) - i\widetilde{\omega}_m\varepsilon\widetilde{\mathbf{e}}_\eta(\mathbf{r}) = i\widetilde{\omega}_\eta\left(-\dfrac{1}{c}\boldsymbol{\eta}_p\times\widetilde{\mathbf{e}}_\eta(\mathbf{r}) - \varepsilon\widetilde{\mathbf{e}}_\eta(\mathbf{r})\right). \end{cases} \tag{4.9}$$

We can rewrite this equation into an eigenvalue problem $\widehat{\mathbf{K}}_\eta\widetilde{\mathbf{x}}_\eta = i\widetilde{\omega}_\eta\widehat{\mathbf{M}}_\eta\widetilde{\mathbf{x}}_\eta$ with

$$\widehat{\mathbf{K}}_\eta = \begin{bmatrix} 0 & \nabla\times \\ \nabla\times & 0, \end{bmatrix}, \widehat{\mathbf{M}}_\eta = \begin{bmatrix} \mu_0 & -\left(\frac{1}{c}\boldsymbol{\eta}\times\right) \\ -\left(\frac{1}{c}\boldsymbol{\eta}\times\right) & -\varepsilon, \end{bmatrix}, \widetilde{\mathbf{x}}_\eta = \begin{bmatrix} \widetilde{\mathbf{h}}_\eta \\ \widetilde{\mathbf{e}}_\eta \end{bmatrix}. \tag{4.10}$$

Since the parameter η is the one that's fixed, the Bloch phase $\exp(i\frac{\omega}{c}\boldsymbol{\eta}\cdot\mathbf{r})$ is now a function of the frequency ω. As a direct consequence, an extra term in $\widetilde{\omega}_\eta$

appears in the equations verified by $[\mathbf{h}_\eta(\mathbf{r}), \mathbf{e}_\eta(\mathbf{r})]$ and extra operators fill the off diagonal terms of $\widehat{\mathbf{M}}_\eta$.

It is trivial that the left eigenvector in this case is $\widetilde{\mathbf{x}}_\eta^\perp = [\mathbf{h}_{-\eta}(\mathbf{r}), \mathbf{e}_{-\eta}(\mathbf{r})]$. This is once again the counter-propagative mode, one that comes from an incident plane wave that has a directionality of $-\boldsymbol{\eta}$. This leads to the following normalization for the $\boldsymbol{\eta}$-Bloch modes:

$$\begin{aligned}\langle \widehat{\mathbf{M}}_k \widetilde{\mathbf{x}}_{-\eta}, \widetilde{\mathbf{x}}_\eta \rangle = \int_\Omega [\widetilde{\mathbf{e}}_\eta(\mathbf{r}) \cdot \varepsilon(\mathbf{r}) \widetilde{\mathbf{e}}_{-\eta}(\mathbf{r}) - \widetilde{\mathbf{h}}_\eta(\mathbf{r}) \cdot \mu_0 \widetilde{\mathbf{h}}_{-\eta}(\mathbf{r}) \\ -\frac{1}{c}\boldsymbol{\eta} \cdot (\widetilde{\mathbf{h}}_{-\eta} \times \widetilde{\mathbf{e}}_\eta + \widetilde{\mathbf{e}}_{-\eta} \times \widetilde{\mathbf{h}}_\eta)] d^3\mathbf{r} = 1,\end{aligned} \tag{4.11}$$

In the case of materials whose permittivity is dispersive and can be described by the Drude-Lorentz model, the introduction of the periodic fields auxiliary fields $\widetilde{\mathbf{p}}_\eta = (\varepsilon(\widetilde{\omega}_\eta) - \varepsilon_\infty)\widetilde{\mathbf{e}}_\eta$ and $\widetilde{\mathbf{j}}_\eta = -i\widetilde{\omega}_\eta \widetilde{\mathbf{p}}_\eta$ allows us to write the linearized eigenproblem $\widehat{\mathbf{K}}_\eta \widetilde{\mathbf{x}}_\eta = i\widetilde{\omega}_\eta \widehat{\mathbf{M}}_\eta \widetilde{\mathbf{x}}_\eta$ with

$$\begin{aligned}\widehat{\mathbf{K}}_\eta &= \begin{bmatrix} 0 & \nabla\times & 0 & 0 \\ \nabla\times & 0 & 0 & -i \\ 0 & 0 & 0 & i \\ 0 & i\omega_p^2\varepsilon_\infty & -i\omega_0^2 & -i\gamma \end{bmatrix}, \\ \widehat{\mathbf{M}}_\eta &= \begin{bmatrix} \mu_0 & -(\frac{1}{c}\boldsymbol{\eta}\times) & 0 & 0 \\ -(\frac{1}{c}\boldsymbol{\eta}\times) & -\varepsilon & 0 & 0 \\ 0 & 0 & 1 & 0 \\ 0 & 0 & 0 & 1 \end{bmatrix}, \widetilde{\mathbf{x}}_\eta = \begin{bmatrix} \widetilde{\mathbf{h}}_\eta \\ \widetilde{\mathbf{e}}_\eta \\ \widetilde{\mathbf{p}}_\eta \\ \widetilde{\mathbf{j}}_\eta \end{bmatrix}.\end{aligned} \tag{4.12}$$

The following system gives us the following form of the normalization

$$\begin{aligned}\langle \widehat{\mathbf{M}}_k \widetilde{\mathbf{x}}_{-\eta}, \widetilde{\mathbf{x}}_\eta \rangle = \int_\Omega \Big[\widetilde{\mathbf{e}}_\eta(\mathbf{r}) \cdot \frac{\partial(\widetilde{\omega}_\eta \varepsilon)}{\partial \widetilde{\omega}_\eta} \widetilde{\mathbf{e}}_{-\eta}(\mathbf{r}) - \widetilde{\mathbf{h}}_\eta(\mathbf{r}) \cdot \mu_0 \widetilde{\mathbf{h}}_{-\eta}(\mathbf{r}) \\ -\frac{1}{c}\boldsymbol{\eta} \cdot (\widetilde{\mathbf{h}}_{-\eta} \times \widetilde{\mathbf{e}}_\eta + \widetilde{\mathbf{e}}_{-\eta} \times \widetilde{\mathbf{h}}_\eta)\Big] d^3\mathbf{r} = 1,\end{aligned} \tag{4.13}$$

We can see that while there are similarities between the two approaches to compute the modes of periodic structures, using the directionality of the incident plane wave as the parameter modifies the normalization of the modes. Since the $\mathbf{k}_p$ and $\boldsymbol{\eta}$-Bloch modes are computed for different parameters, and ultimately different equations, they are not the same kind of modes. Though they will coincide normal incidence ($\mathbf{k}_p = \boldsymbol{\eta} = 0$), the modes will have different eigenfrequencies and modal fields at oblique incidence. Figure 4.3 shows the trajectory of a fundamental mode of a lamellar one-dimensional grating as both parameters rise.

Computation of η-modes in COMSOL

Due to the slightly different equations to solve, the standard Electromagnetics solver of COMSOL's with pseudoperiodicity is not a viable tool to compute the

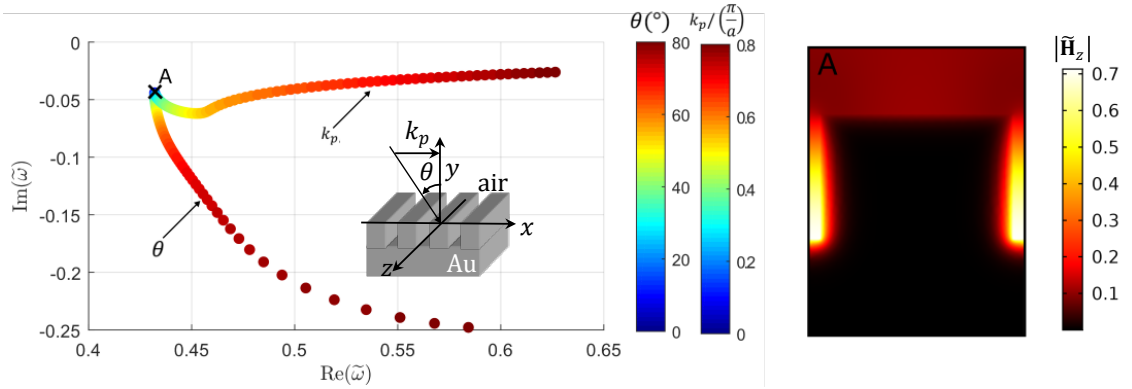

Figure 4.3: Eigenfrequencies of a η- and $\mathbf{k}_p$-modes of a 1-D periodic lamellar groove grating in the complex plane for different values the angle of incidence θ and the parallel momentum k_p. We show the absolute value of the normalized magnetic field of the mode at $k_p = \theta = 0$.

modes. In that scheme, the components of $\mathbf{k}_p$ need to be entered into the "Periodic Boundary Condition" widget. Unfortunately, the solver does not accept a value of $\mathbf{k}_p$ that contains the eigenvalue of the mode.

To compute the η-modes with COMSOL Multiphysics, we rewrite the second order Maxwell's equations for $\tilde{\mathbf{e}}_\eta(\mathbf{r})$ in weak formulation and apply Periodic Boundary Conditions where needed. In the case of Lorentz-Dispersive materials, an additional equation verified by the auxiliary fields $\tilde{\mathbf{p}}_\eta$ in the those material domains. PMLs are applied if needed in the directions where the domain should be infinite. With this solver [47, 30], we can compute a large number of modes around a central frequency. In figure 4.4we plot the spectrum obtained through 6 separate computations of 1000 modes, for a total of 6000 modes.

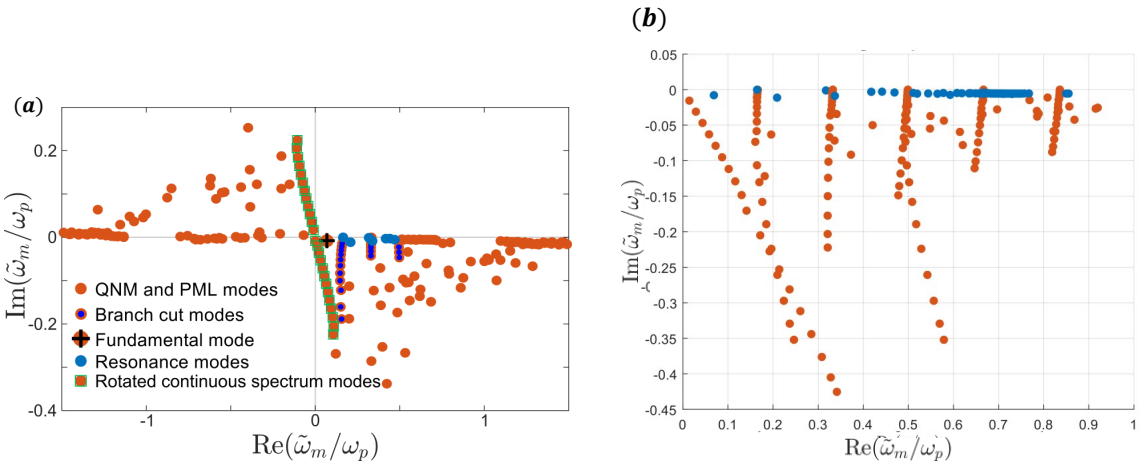

Figure 4.4: (a) Complex plane representation of a sample of 200 η-modes computed with the solver for a 1D lamellar grating. (b)Within the area in the red dashed rectangle, we have computed modes for the same structure but with a different PML. The QNMs have stayed in the same position in the complex plane while the PML modes are different.

Among the complex frequencies plotted in figure 4.4, we can note that there are modes near the real axis which usually are physical modes. We also find 2

mode patterns previously reported by Vial in 2014. The first being the "rotated" continuous spectrum that arises from the use of PMLs, causing modes with real eigenfrequencies to rotate in the complex plane. The second pattern are modes that are present at the real frequency corresponding to the Rayleigh anomalies, or the frequency where a diffraction order goes from being evanescent to propagating. These branches of modes are regularly spaced along the real axis, with a gap of $\frac{2\pi c}{a}$ between each branch. These are called "branch cut modes" due to the fact that they represent a mathematical discontinuity, in this case, the transition from evanescent diffraction orders to propagative ones.

In figure 4.4, we notice that the modes have a central symmetry point at the origin of the complex plane. The modes with negative real parts have positive imaginary parts which would imply that they are no longer damped in time and instead exponentially amplified. This, however, is a purely numerical phenomena caused by the use of non-dispersive PMLs in that particular computation.

4.2.2 Scattered field formulation

Choice of the background medium

In the case of an isolated resonator it is usually convenient to choose the background permittivity ε_b as uniform. However, in the case of more complex structures, like infinitely long slabs with a singular nanoparticle on its surface or a nanoparticle on a substrate, the resonator domain could be infinitely large.

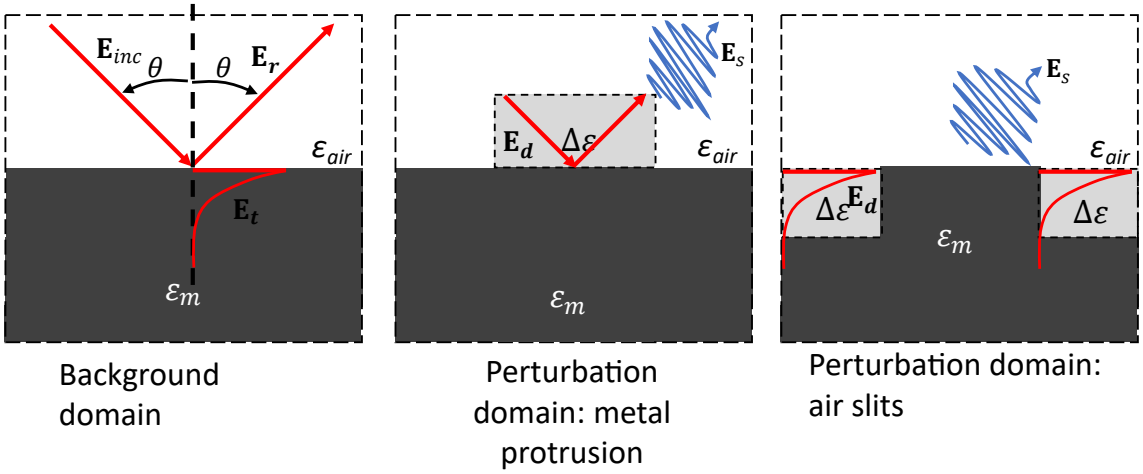

Figure 4.5: Example of a driving field $\mathbf{E}_d$ inside the perturbation domain in the case of a lamellar grating with an absorbing metal substrate with an air superstrate. In (metal protrusion), the driving field inside the perturbation domain is a superposition of the incident and reflected field. In (air slits), the driving field is the transmitted field, exponentially damped inside the metal substrate.

The driving field is a solution of Maxwell's equation in an inhomogeneous background medium. Here, the background domain has a flat interface between the air and the metal substrate. The driving field above the substrate is a superposition of the incident field from the source and the field reflected off the flat interface [78]. The field transmitted inside the substrate is exponentially damped

due to the absorbing properties of the material. The lamellar grating can be constructed from the background domain in two ways. A metal protrusion can be added on top of the flat interface or air slits can be dug into the substrate. This leads to two complementary definition of the perturbation domain inside which $\Delta\varepsilon$ is non-null with different driving fields.

η-QNM expansion of the scattered field from illumination at a fixed incidence angle

Derivation of the excitation coefficient

The following derivation is very similar to the derivation of the excitation coefficient found in previous chapters. Let us now consider the reconstruction problem of the scattered field upon illumination by an incident plane wave $[\mathbf{H}_{inc}, \mathbf{E}_{inc}] = [\mathbf{h}_{inc}, \mathbf{e}_{inc}]\exp(i\frac{\omega}{c}\boldsymbol{\eta}\cdot\mathbf{r})$ with the "directionality" vector $\boldsymbol{\eta}$ and the (real) frequency ω. In the scattered-field formalism used for the expansion, the scattered field is defined by a local change $\Delta\varepsilon(\mathbf{r},\omega)(\Delta\varepsilon \neq \text{for } \mathbf{r} \in V_{res})$ for a background permittivity ε_b so that $\varepsilon_b + \Delta\varepsilon$ is equal to the permittivity distribution of the grating geometry. Similarly, the background field $[\mathbf{h}_b, \mathbf{e}_b]\exp\left(i\frac{\omega}{c}\boldsymbol{\eta}\cdot\mathbf{r}\right)$ is defined as the electromagnetic field that is solution of Maxwell's equations for the background permittivity distribution $\varepsilon_b(\mathbf{r},\omega)$ upon illumination by the incident plane wave. From the orthonormality condition, it is straightforward [30] to derive closed-form expressions for the excitation coefficients α_m of the QNM expansion of the scattered field $\boldsymbol{\Psi}_{sca}(\mathbf{r},\omega,\boldsymbol{\eta}) = \sum_{m=1}^{M}\alpha_m(\omega)\boldsymbol{\Psi}_{\eta,m}$:

$$\alpha_m = -\frac{\omega}{\omega-\widetilde{\omega}_m}\int_{V_{res}}\Delta\varepsilon(\mathbf{r},\omega)\mathbf{e}_d\cdot\widetilde{\mathbf{e}}_{-\eta}d^3\mathbf{r} = 1. \tag{4.14}$$

Reflection coefficient and modal contributions to reflectance

The scattered Bloch field is given by $[\mathbf{h}_s, \mathbf{e}_s] = [\mathbf{h}_{tot}, \mathbf{e}_{tot}] - [\mathbf{h}_d, \mathbf{e}_d]$ and can be expanded into a sum of $\boldsymbol{\eta}$-QNMs:

$$[\mathbf{h}_s, \mathbf{e}_s] = \sum_{m=1}^{M}\alpha_m(\omega)\left[\widetilde{\mathbf{h}}_{m,\eta}, \widetilde{\mathbf{e}}_{m,\eta}\right] \tag{4.15}$$

In the case of a one-dimensional grating, periodic along the x-axis and infinite along the z-axis, illuminated by a TM-polarized plane wave(the azimuthal angle $\varphi = 0$), the total magnetic field above the grating can be expressed as a sum of plane waves[75] similarly to 4.1:

$$H_{z,I}(\mathbf{r},\omega) = H_{inc,z}(\mathbf{r},\omega) + H_0\sum_i r_i\exp\left(-i\left(k^r_{i,x}x + k^r_{i,y}y + k^r_{i,z}z\right)\right). \tag{4.16}$$

Due to the polarization of the incident plane wave and the structure of the grating, the magnetic field has only one non-null component on z. In the scattered field formulation, the total field can be rewritten as such:

$$H_{z,I}(\mathbf{r},\omega) = H_{d,z}(\mathbf{r},\omega) + H_{s,z}(\mathbf{r},\omega) = H_{inc,z}(\mathbf{r},\omega) + H_{\uparrow,z}(\mathbf{r},\omega) + H_{s,z}(\mathbf{r},\omega), \tag{4.17}$$

where $H_{s,z}(\mathbf{r},\omega)$ is the z-component of the scattered field, $H_{\uparrow,z}(\mathbf{r},\omega)$ is the z-component of the portion of the driving field that is reflected upwards off of the background medium (which will be a flat air-metal interface). Taking 4.16 and 4.17, we have the following relationship between the scattered magnetic field and the amplitudes of the reflected waves:

$$\sum_j r_j \exp\left(-i\left(k^r_{j,x}x + k^r_{j,y}y + k^r_{j,z}z\right)\right) = \frac{1}{H_0}\left(H_{\uparrow,z}(\mathbf{r},\omega) + H_{s,z}(\mathbf{r},\omega)\right). \tag{4.18}$$

$H_{s,z}$ can be expanded into a sum of its Fourier harmonic since it's a pseudo-periodic function. $H_{\uparrow,z}$ only oscillates at the excitation frequency so only its 0^th order Fourier Harmonic is non-null. Eq. 4.18 is rewritten as:

$$\sum_j r_j \exp\left(-i\mathbf{k}_{r,j}\cdot\mathbf{r}\right) = \frac{1}{H_0}\sum_j \int_{x=0}^{a}\left[H_{\uparrow,z}(\mathbf{r},\omega) + H_{s,z}(\mathbf{r},\omega)\right]\exp\left(-i\mathbf{k}_{r,j}\cdot\mathbf{r}\right)dx, \tag{4.19}$$

where $\mathbf{k}_{r,j} = k^r_{j,x}\widehat{\mathbf{x}} + k^r_{j,y}\widehat{\mathbf{y}} + k^r_{j,z}\widehat{\mathbf{z}}$ is the wavevector of the j^{th} diffraction order. In this instance, the x-component of the wavevector can be expressed as $k^r_{j,x} = \frac{\omega}{c}\sin(\theta) + j\frac{2\pi}{a}$ and $k^r_{j,x} = \sqrt{\left(\frac{\omega}{c}\right)^2 - \left(k^r_{j,x}\right)^2}$. In the case of the reflectivity in the specular direction, computing the amplitude of the 0^{th} diffraction order is required and using Bloch's theorem we obtain:

$$r_0(\omega) = \frac{1}{H_0}\int_{x=0}^{a}\left[h_{\uparrow,z}(\mathbf{r},\omega) + h_{s,z}(\mathbf{r},\omega)\right]dx. \tag{4.20}$$

We can expand $h_{s,z}$ onto the QNM basis using Eq. 4.15 to rewrite the reflectivity as a sum of individual modal contributions interfering with the plane wave reflected off the air-metal interface.

$$r_0(\omega) = \frac{1}{H_0}\left[\int_{x=0}^{a} h_{\uparrow,z}(\mathbf{r},\omega)dx + \sum_{m=1}^{M}\alpha_m(\omega)\int_{x=0}^{a}\widetilde{h}_{m,z,\eta}(\mathbf{r})dx\right]. \tag{4.21}$$

$\frac{1}{H_0}\int_{x=0}^{a} h_{\uparrow,z}(\mathbf{r},\omega)dx = r_{metal}(\omega)e^{i\phi}$ where r_{metal} is the Fresnel reflection coefficient of the air-metal interface and $e^{i\phi}$ the phase the reflected plane wave has accumulated at a distance l_0 from the interface, on the period where the integral is computed. While the value of the reflectance should not depend on this distance [79], it will be shown in the next chapter that it can cause the computed values to vary noticeably.

The complex normalized amplitude of an excited QNM in the specular direction will be denoted by

$$q_m(\mathbf{r},\omega) = \frac{1}{H_0}\alpha_m(\omega)\int_{x=0}^{a}\widetilde{h}_{m,z,\eta}(\mathbf{r})dx \tag{4.22}$$

where the integral $\int_{x=0}^{a}\widetilde{h}_{m,z,\eta}(\mathbf{r})$ is the complex amplitude of the plane wave scattered by a QNM into the far field [79]. The reflectivity in the specular direction

can thus be written as the interference of the reflected plane wave and the plane wave decomposition of the of the excited QNMs of the system:

$$r_0(\omega) = r_{metal}(\omega)e^{i\phi} + \sum_{m=1}^{M} q_m(\omega). \tag{4.23}$$

The specular reflectance is obtained with

$$R_0(\omega) = |r_0(\omega)|^2. \tag{4.24}$$

4.3 Numerical results

4.3.1 Reconstruction of the reflectance on a One-dimensional lamellar grating

To demonstrate the effectiveness of the method, we consider a gold grating that efficiently absorbs light over the visible (we have optimized the groove depth for that purpose) and near infrared spectral range. The grating is composed of tiny rectangular air grooves which are $w = 60$ nm wide and $h = 350$ nm deep.The grating has a period of $a = 600$nm. In this section, we will compute the specular Reflectance computed with the Rigorous Coupled Wave Analysis (RCWA) [80, 81]. Since 401 Fourier harmonics are retained in the computation, the computed data are highly accurate and be used as reference data hereafter. Using COMSOL Multiphysics, we build a model of the grating unit cell. The periodicity along the x-direction is enforced with periodic boundary conditions, and the outgoing-wave condition is fulfilled in the upper y-direction using PMLs. Due to the damping in the substrate, there is no need to put PMLs under the finite layer of gold.

We then compute the eigenmodes with the built-in eigensolver of COMSOL using the augmented field formulation of Eq. (1). The computational time per eigenmode is a few seconds with a standard desktop computer. We then normalized the QNMs using Eq. 4.11.

We perform a first scattering experiment with a limited number of modes to test the viability of the different background medium. We will compare the air slits perturbation to the metal perturbation as pictured in figure 4.5. Both perturbation schemes will yield different driving fields $\mathbf{E}_d$ and perturbation volume V_res, which will give a different perturbation coefficient α_m computed according to 4.14. We compute 20 modes and excite them with different driving fields. The eigenfrequencies and the values of the excitation coefficients are plotted on the left side of figure 4.6. The value of the excitation coefficient can vary significantly with the change in resonator domain and background field. We have plotted the specular reflectance computed according to Equations 4.21 and 4.24 on the right side of figure with the 20 modes. We can see that the "air slit" perturbation domain computation correctly reconstructs the two resonance deeps with 20 modes, while the "metal" perturbation domain computation does not: the peak at 0.77 μm is slightly shifted. The "metal" perturbation also creates some non-physical results, like the reflectance reaching values superior to 1. With the "air slit" perturbation, we also plot the reflectance with only the resonant mode at .77 μm in

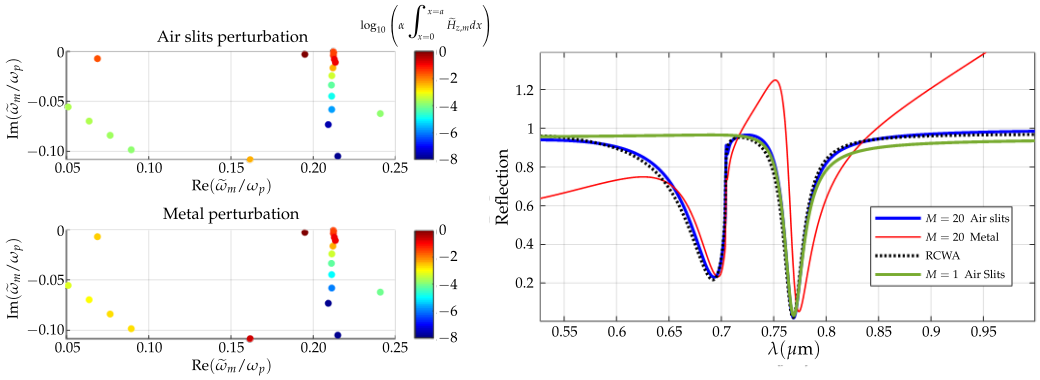

Figure 4.6: Complex plane representation of 20 η-Modes of a 1D lamellar grating for an incidence angle of $\theta = 10°$. The circles are colored according to the maximum value of the excitation coefficient in the spectrum plotted on the right. We plot the specular reflection spectra of this grating for an incident angle of $\theta = 10°$, with $M = 20$ modes for both perturbation domain. For the slit perturbation, we also plot the reconstruction with one resonance mode.

the expansion. We can see that the resonance deep is correctly reconstructed at near the resonance with some gap at higher wavelengths between this response and the RCWA reference due to the lack of modes in the expansion. This preliminary computation has shown that the "air slit" perturbation is seemingly more accurate for this particular structure and we will adopt that perturbation in the rest of the chapter.

We then reconstruct the spectrum accurately over a large spectrum using the QNM expansion. The grating is illuminated by a plane wave impinging from air with an angle of incidence $\theta = 30°$, and polarized with a magnetic-field parallel to the grooves (TM polarization). Like before, we compute the eigenmodes with the built-in eigensolver of COMSOL using the augmented field formulation of Eq. 4.12. The magnetic fields of the 7 dominant QNMs, labelled A, B, ... G, which dictate the positions and widths of the 7 main resonance dips, are displayed in the upper panel of Fig. 4.7. A total of 6000 modes were computed, with the resonant frequencies of the modes within the range $\mathrm{Re}(\tilde{\omega}_m) \in [-3\omega_p, 3\omega_p]$.

First we only consider the seven dominant QNMs in the expansion ($m = 1, \ldots 7$). The specular reflectance computed for $M = 7$ is shown with the blue curve. Qualitative agreement with the RCWA data is achieved, particularly for resonance features. We then sort the computed QNMs according to their decreasing value of the plane wave amplitude q_m [30] and reconstruct the scattered field with the first $M = 200$ most impactful ones, see the red curve. Now a quantitative agreement is achieved. Thanks to computational results obtained with the real frequency solver of COMSOL Multiphysics, we have additionally verified that the small residual difference with the RCWA data is primarily due to a numerical dispersion between the Fourier and finite-element methods, rather than to the specific choice of the truncation rank $M = 200$.

These 200 modes are plotted in Figure 4.8. We can see that the modes retained in the expansion range from beyond the considered spectrum on which we reconstruct the reflectance. Not only that but both numerical and QNM modes are used in the expansion. In Figure 4.11, we plot the reconstruction for different

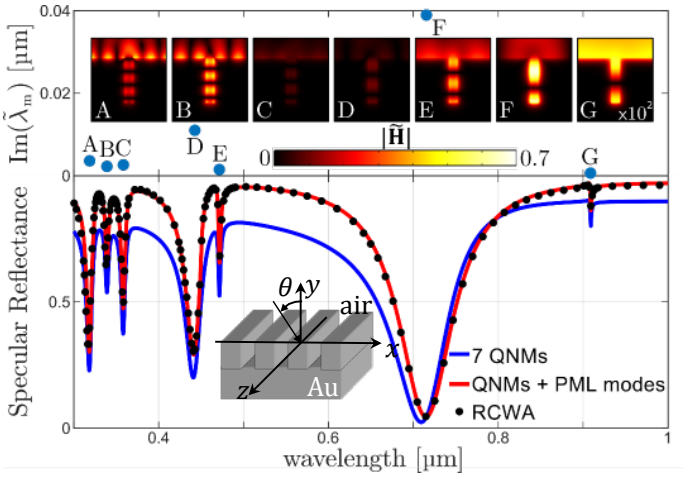

Figure 4.7: Reconstruction of the reflectance spectrum of a gold grating composed of tiny rectangular air grooves (see the inset) illuminated by a plane wave with an angle of incidence $\theta = 30°$ in the x-y plane and TM-polarized. The reconstructed specular reflectance spectra with $M = 7$ and 200 modes retained in the expansion are shown with the blue and red curves, respectively, and are compared with reference data obtained with the RCWA (black dots). The magnetic-field moduli of the $M = 7$ dominant normalized QNMs, labelled A, B, ... G, dictate the positions and widths of the 7 main resonance dips.

values of M, showing the correspondence between individual modes and resonance deeps but also the broad, cumulative effects of non-resonant modes on the spectrum. We can see that when only the resonant modes are included in the expansion, that the corresponding deeps are not only slightly shifted compared to the reference, but also asymmetric. Adding a resonant mode into the expansion creates a Fano-type resonance pattern, since the narrow-band QNM resonance interferes in the far-field with the background field. As more modes are added into the expansion, the deeps are shifted back into their correct position, as can be seen from the transition from $M = 8$ modes to $M = 25$ modes to $M = 100$. With $M = 25$ modes, we can see that the reflectance reaches values above 1 which is erroneous.

The addition of numerical modes, like those from the branch cuts or on the "PML veil", which bear no physical meaning, does help convergence but can create some unusual results due to the truncated basis of modes. Physical modes in this example,which localize electromagnetic energy in the grating's grooves or on the metallic surface, decrease the overall reflection over the whole spectrum as can be seen from the transition from 7 to 8 modes. In this instance, the addition of the fundamental mode of the grating, whose resonant frequency lies in the infrared at $\lambda = 1.1\,\mu m$, where the light is localized in the grooves, greatly decreases the reflectance computation over the whole spectrum. The plethora of plasmonic modes, among others, added between the 25^{th} and the 100^th modes reduce the overall reflectance to bring it back under 1. The modes added between $M = 100$ and $M = 215$ finely refine the spectrum allowing a quantitative reconstruction of the reflectance over a large spectrum. The mean error computed over

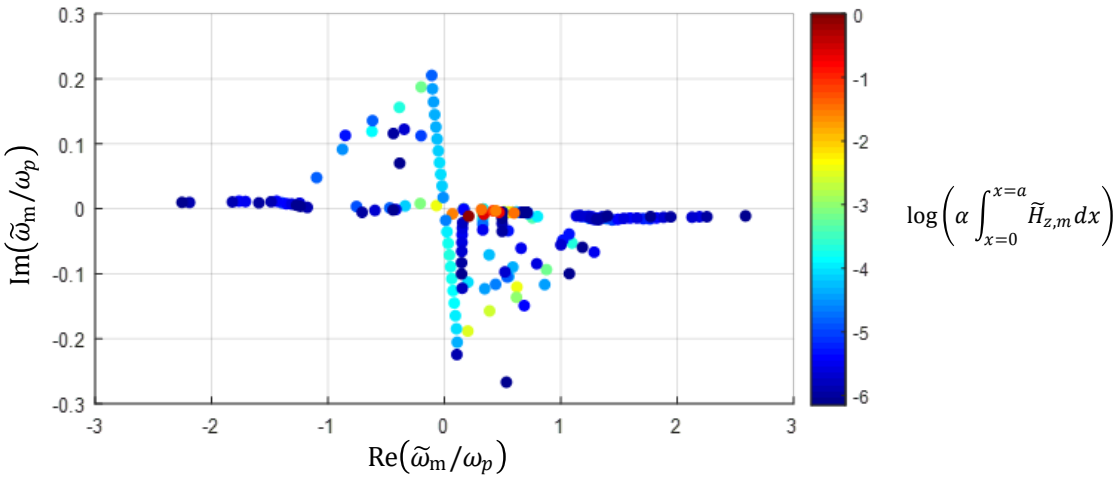

Figure 4.8: Complex plane representation of the sample of the modes used in the expansion for $M = 200$. Modes are colored according to the amplitude of the plane waves the QNM creates in the specular direction in the far field.

the spectrum is

$$\text{error} = \frac{1}{\lambda_2 - \lambda_1} \int_{\lambda_1}^{\lambda_2} \left| R_{QNM}(\lambda) - R_{RCWA}(\lambda) \right| d\lambda, \tag{4.25}$$

where R_{QNM} is the reflectance reconstructed with QNMs while R_{RCWA} is computed using RCWA and used as reference. We can also compute the mean relative error over the spectrum with

$$\text{relative error} = \frac{1}{\lambda_2 - \lambda_1} \int_{\lambda_1}^{\lambda_2} \frac{\left| R_{QNM}(\lambda) - R_{RCWA}(\lambda) \right|}{R_{RCWA}} d\lambda. \tag{4.26}$$

In Figure 4.9c, we plot both of these errors as a function of the number of modes in the expansion M. For $M = 212$ modes, the lowest value of the mean relative error is reached at 0.0112. However, the mean relative error rises with the addition of additional modes and converges at a value of 0.0255. There could be multiple reasons for why the error converges at this early with no improvement with the addition of more modes. The reason for this could be that the mesh is too coarse to reach lower error values so it stagnates. Another could be that we are still missing important modes that would greatly help the expansion, modes that could be found at higher frequencies.

We have shown in this section that the modes can be classified in terms of their relevance in the reconstruction of the reflectance. Out of 4000+ modes, the lowest error is reached with about 200 modes. The error could be further lowered if we were to search for additional modes in a broader spectral range. We've shown that both QNMs and PML modes had great influence on the convergence of the reflectance spectra.

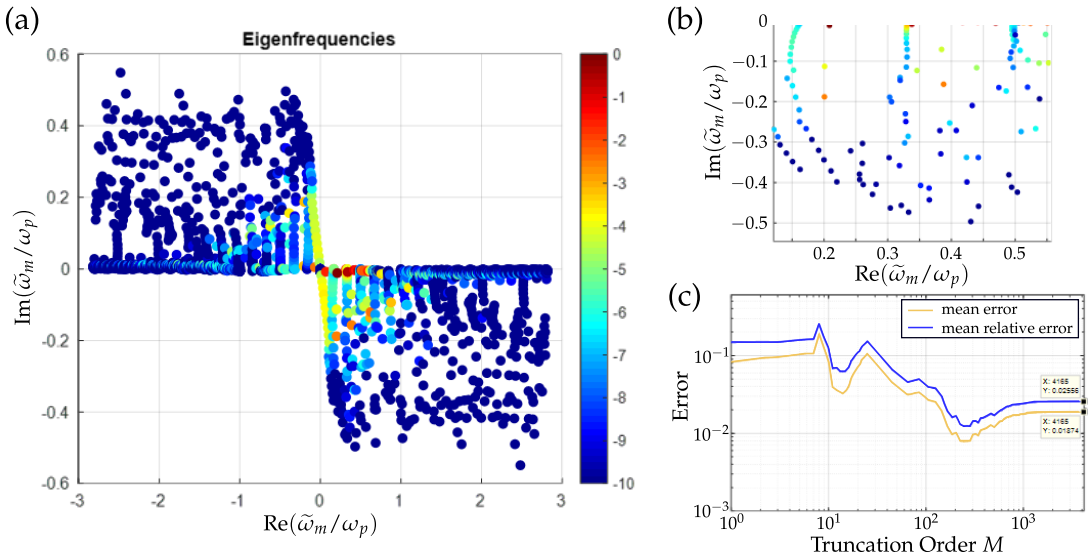

Figure 4.9: (a) Complex mode spectrum of the 6000 modes included in the expansion. Modes are colored according to $|q_m|$. The modes who resonate within the evaluation spectrum $\lambda \in [300\text{nm}, 1000\text{nm}]$ are plotted in (b). (c) Error curve when the modes are ranked according to $\max_\omega |q_m(\omega)|$. A minimum mean relative error of 0.0112 is reached for $M = 212$ modes but the error rises as more modes are added into the expansion.

4.4 Implementation with MAN freeware

In this section, we will detail the implementation of the computation of the $\boldsymbol{\eta}$-modes into the MAN freeware. The freeware uses both COMSOL MULTIPHYSICS software and COMSOL-MATLAB-Livelink. The computation of modes is done within a COMSOL MULTIPHYSICS model, while the computation of the overlap integrals are performed on MATLAB after the eigenmodes are extracted using Livelink.

QNMs are intrinsic to the resonator [14] which means that their computation through the solving of the source-free Maxwell's equations should not depend on any possible excitation. However, in the case of periodic structures, whose periodicity translates into an infinite computation domain, we use the Bloch Theorem to truncate the computation domain to a unit cell and instead compute Bloch modes as stated in section 4.2. However, this leads to Maxwell's Equations for the Bloch modes to be parameterized by the in-plane wavenumber of the incident plane wave k_p [32], or in the case of $\boldsymbol{\eta}$-modes, by the vector $\boldsymbol{eta}$ giving the direction of the incident plane wave. Computing $\boldsymbol{\eta}$-modes fixes the direction of the excitation wave but not the frequency.

The Maxwell's can be written in COMSOL in weak formulation for either TM or TE polarization. In the case studied that was presented in the previous section, they were written for a TM polarized plane wave. This reduces the number of variables that we need to compute. In the case of TM polarization, we only compute the x- and y-components of a mode's electric field.

In order to normalize the $\boldsymbol{\eta}$-modes, we need to compute the modes $\widetilde{\mathbf{e}}_{m,-\eta}$ with the opposite incident direction $-\boldsymbol{\eta}$. For structures with a symmetries along the x-

direction, with the symmetry plane $x = 0$, we can compute those from the modes $\widetilde{\mathbf{e}}_{m,\eta}$ with the following relation:

$$\widetilde{\mathbf{e}}_{m,-\eta}(x,y) = \begin{bmatrix} \widetilde{e}_{x;m,\eta}(-x,y) \\ -\widetilde{e}_{y;m,\eta}(-x,y) \end{bmatrix}, \tag{4.27}$$

where $\widetilde{e}_{x;m,\eta}(x,y)$ and $\widetilde{e}_{y;m,\eta}(x,y)$ are respectively the x- and y- component of the η-mode $\widetilde{\mathbf{e}}_{m,\eta}$. The modes have the same eigenfrequency $\widetilde{\omega}_m$.

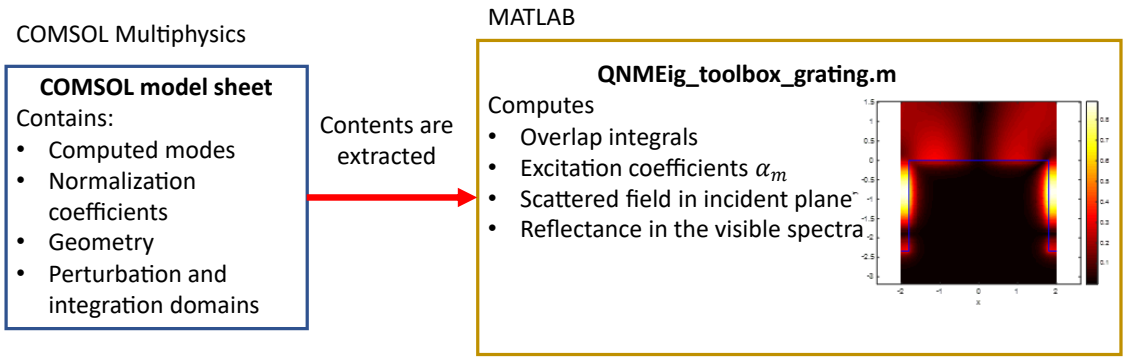

Figure 4.10: QNMEig implementation and work-arround

Once the modes are computed, the modes can be extracted using Livelink and MATLAB. We define selections in the COMSOL model in order to extract the modes in relevant domains, such as in the regions of space where the permittivity perturbation $\Delta\varepsilon$ is not null, in order to compute the excitation coefficient or on a line above the resonator in order to compute the reflectance. The extracted fields' components are stored in a vector and the coordinates of the mesh nodes from which the field was extracted from as well. These vectors have the same size. The coordinates are useful in defining the incident field on the mesh coordinates to perform the overlap integral. Overlap integrals are performed with Matrix multiplication in MATLAB using a matrix containing the values of the integration variable δS or δl for each mesh node coordinate, depending on whether a surface or linear integral respectively. The integral of a function $f(x,y)$ over the surface Σ is thus performed over a number N_{mesh} of discrete points with that area such that:

$$\iint_{\Sigma} f(x,y)dS \approx \sum_{p}^{N_{mesh}} f(x_p,y_p)\delta S, \tag{4.28}$$

where x, p and y_p are the x and y coordinates of the p^{th} node point of the inside the surface Σ. The same approximation exists for linear integrals over one-dimensional segments in space and is used to compute the integral

$$\int_{x=0}^{x=a} \widetilde{H}_{z,m}(x,y)dx.$$

This allows for swift computation of integrals and enables quick and subsequent computations of the excitation coefficient $\alpha(\omega)$ over a great number of frequencies.

An example script that extracts the modes from a COMSOL model and computes the excitation coefficient coefficient and the corresponding reflection of the grating is included in the QNMEig package of MAN [47].

4.5 Conclusion

In this chapter, we have introduced a method with which to compute and normalize the eigenmodes of open, periodic structures. We have shown that some of these modes correspond to grating anomalies and they allow us to qualitatively reconstruct the spectral response of gratings. However, in order to accurately reconstruct the spectral response, not only are a great number of modes required, but also modes whose origins are numerical and contain no physical meaning.

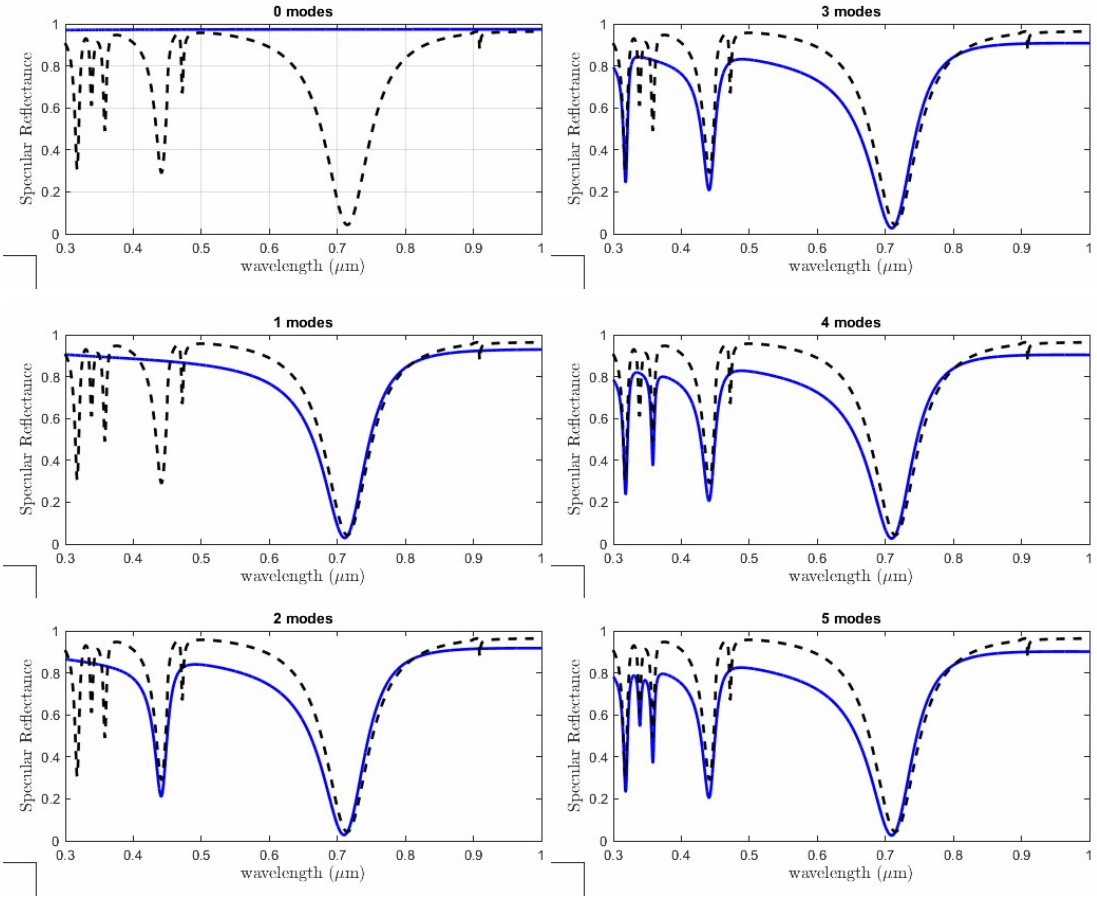

Figure 4.11: Reflectance spectrum for $M = 0, 1, 2, 3, 4, 5, 6, 7, 8, 25, 100, 215$ modes included in the expansion. The first 7 modes are the seven resonances of the spectrum, the other modes are added according to the value of the amplitude of the corresponding plane wave they spawn in the specular direction q_m.

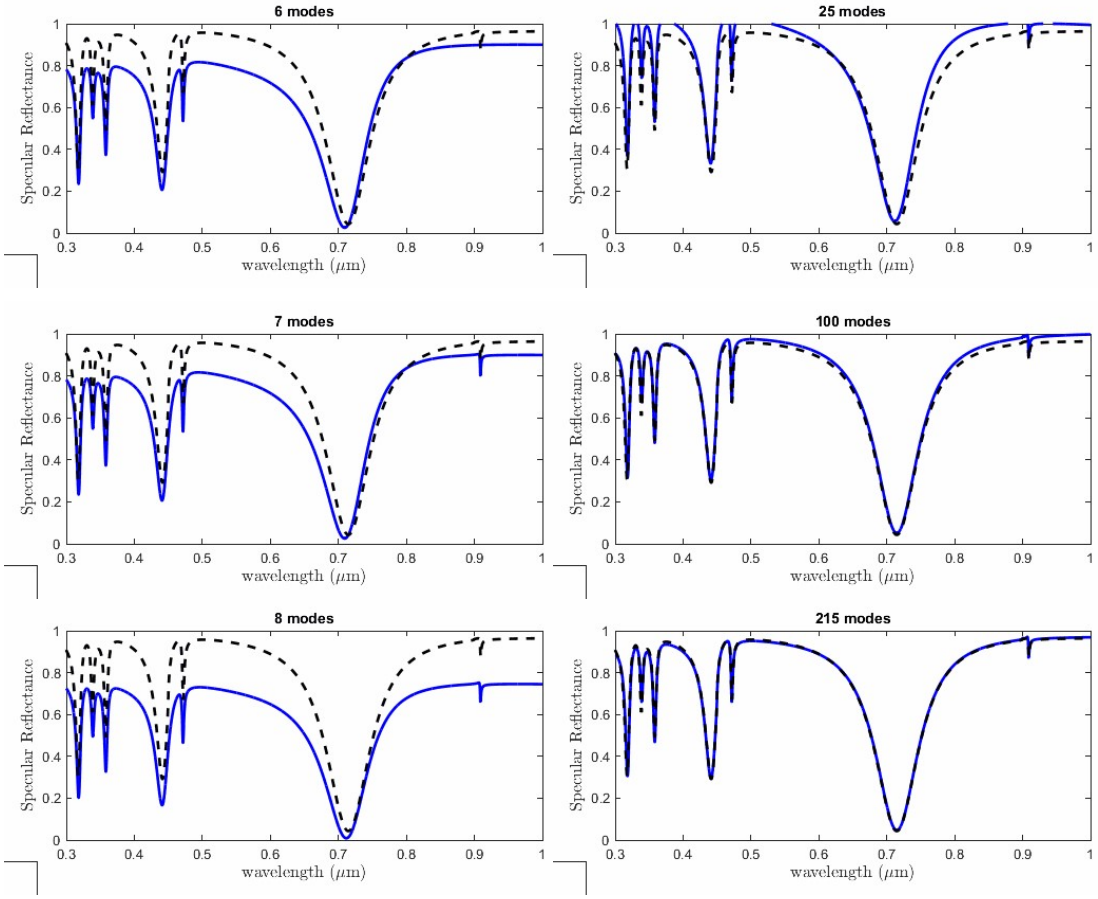
6 modes
25 modes
7 modes
100 modes
8 modes
215 modes
Specular Reflectance
wavelength (μm)
0
0.2
0.4
0.6
0.8
1
0.3
0.4
0.5
0.6
0.7
0.8
0.9
1

Chapter 5

Numerical limitations of the Quasinormal mode expansion

In the previous chapters, we have used the QNM expansion to compute the field or a related quantity. In order to obtain convergent results, hundreds or thousands of modes have been computed and included in the expansion.

An overview of the literature shows two paradigms under which the expansion is used to reconstruct physical quantities. The first fashion of use of the expansion employs usually around or under 10 modes, with each mode often corresponding to a resonance of the reconstructed quantity [38, 39, 40, 41, 42, 43]. In these articles the QNMs reconstruct the resonant features with a seemingly "good agreement" [44, 45] between the reference curve and the QNM reconstruction at resonance. The error varies from experiment to experiment, but is rarely quantified. Analysis of the various plots would generally yield the idea that near the resonance frequency of the mode, the relative error would fall within the single percent range and below [40, 82, 83] and rises expectedly outside of resonance [40]. Some of the methods used to compute the modes are usually limited to one mode per computation, such as pole-searching mode solvers [46] or FDTD methods [39].

The second paradigm arises from the development in recent years of numerical tools to perform the "wholesale" computation of the modes of resonators made of dispersive materials. These tools which either employ eigenvalue solvers that use auxiliary fields [30, 47, 42, 48] or nonlinear eigenvalue solvers [34, 49]. It is usually with the exploitation of these tools that the computation of purely numerical modes(sometimes referred to as PML modes) becomes either coincidental or voluntary as is their inclusion into the expansion. With the use of hundreds of modes and a wide eigenvalue spectrum [30, 34, 50], the convergence is attained to varying degrees of accuracy. The supplementary information of [30] currently resides at the state of the art for the convergence of the modal expansion of the extinction cross-section of many dispersive structures, such as a silver sphere and a bowtie antenna. The relative error on the extinction cross-section spectra, which contains multiple resonant peaks, reaches a value of 10^{-5} and under when thousands of modes are added into the expansion. The modes are added into the expansion after being sorted according to their impact on the spectra. The error tends to decrease as the total number M of modes in the expansion increases. The variation is not monotonous but the average error seems to trend towards a

value of $10/M^2$, as can be seen in figures SI-5, SI-6, and SI-7. These error values are dependent on mesh finesse as figure SI-5 of the same document shows that the error reaches different values for different mesh finesses. In [34], the L^2 error of the field in a single point in space is just over 1% over a wide frequency spectrum. These types of work show that we can expect the modal expansion to converge in space and for all frequencies if we have all the modes of a structure, both physical and purely numerical. The work presented in Chapter 3 and 4 falls within this category. Some other works in the literature detail other methods to make the QNM expansion converge. In [36], 8 modes are computed and a contour integral is used to obtain a relative error on the spectra with values ranging from 10^{-4} to 10^{-7}. In [63], "perfect agreement" with a reference computation is reached using the QNM expansion for a one-dimensional resonator when the modes are calculated with causality considerations. The trend is moving to find ways to improve the overall convergence of the expansion while employing as few modes as necessary instead of converging through the use of the complete basis of modes.

In this chapter, we will describe some of the numerical factors that may impact the accuracy and the speed of the convergence of the QNM expansion. We will first look into the influence of the single Perfectly Matched Layer (PML) in the computation of the modes of the grating studied in the previous chapter. We will then analyze the convergence of the field in space and of the reflectance spectra of the grating. Lastly, we will try to define criteria to sort the modes with in order to find ways to optimize the convergence speed of the expansion.

5.1 Influence of the PML

In this section, we will expose how the PML is implemented in the grating model used to compute the η-modes, how the modes are influenced by this parameter and how the variations of this parameter can be used to find the physical modes among the thousands of modes that are computed in bulk. This section uses the sign convention $\exp(-i\omega t)$ for time-harmonic fields.

5.1.1 Implementation of the PML in the QNMEig Grating model

The Perfectly Matched Layer is an artificial absorbing layer used to simulate systems with open boundaries. In the case of the grating studied in the last chapter, a single PML is placed above the grating, to emulate an air superstrate. The PML has a finite thickness of 300 nm and is placed 275 nm above the top of the grating.

Compared to every other model in the QNMEig package in MAN [47] which are implemented in COMSOL, the model does not use the built-in Electromagnetic Waves Physics package to compute the η-modes. Instead Maxwell's equations for the η-modes are rewritten with the "weak formulation" syntax employed by the Finite Element solver of COMSOL. The materials' permittivity tensor's components in this example are all individual variables defined for each material. In the case of homogeneous and isotropic materials, only the diagonal terms of the permittivity tensor $\bar{\bar{\varepsilon}}$ are non zero.

The PML also is defined differently compared to the rest of the catalog of

models included in MAN. The PML in the grating model is defined via the permittivity tensor. In this example, complex-valued coordinate transformations are applied to the background media. We define a complex PML coefficient σ that is applied differently to the different components of the PML's permittivity tensor depending on which directions the PML is stretching into an open boundary. In the case of the PML in the grating model, as shown in Fig. 5.1, the PML is there to create an open boundary in the y direction. The permittivity tensor of the PML is thus:

$$\bar{\bar{\varepsilon}}_{PML} = \begin{pmatrix} \varepsilon_b\sigma & 0 & 0 \\ 0 & \varepsilon_b/\sigma & 0 \\ 0 & 0 & \varepsilon_b\sigma \end{pmatrix}. \tag{5.1}$$

The permeability tensor of the materials and the PML are also defined in the same manner.

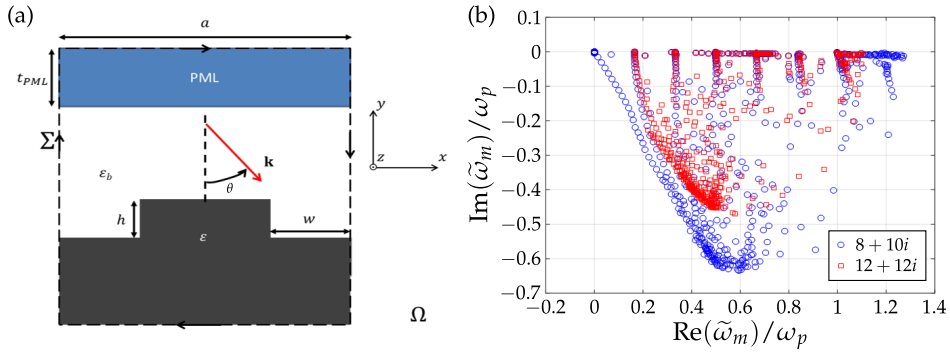

Figure 5.1: (a) Schematic of the unit cell. (b) Influence of the PML coefficient on the computations of modes. In both of these simulations, we searched for 1000 modes around the central frequency $\omega_c = \dfrac{\omega_p}{2}$ with two different complex PML coefficients parameters $\sigma = 8 + 10i$ and $\sigma = 12 + 12i$.

5.1.2 Influence of the PML coefficient and identification of QNM modes

In order to gauge the importance of the PML coefficient, we launch several computations to compute 1000 modes around the central frequency $\dfrac{\omega_p}{2}$ with two PML coefficients. This allows us to discern the numerical modes from the physical modes since numerical modes are more "sensitive" to most slight changes in numerical parameters. In Fig. 5.1, we plot the eigenfrequencies for two separate eigenmode computations with different PML coefficients and we can see that both computations have yielded mostly different results, with many modes not having the same eigenfrequency between the two simulations. We can notice that the modes computed with the PML parameter $\sigma = 12 + 12i$ do not extend as far away from the central frequency ω_c in the complex plane as the modes computed with the parameter $\sigma = 8 + 10i$. We can see that the QNMs which are close to the real axis have the same eigenfrequencies with both computations. We can see that modes with a relatively high imaginary part ($\mathrm{Im}(\tilde{\omega}_m/\omega_p) < -0.05$) have widely

different eigenvalues and form clusters in different ways. The cluster of numerical modes shifts along the imaginary axis. The larger $\mathrm{Re}(\sigma)$ is, the closer to the real axis the cluster is. The solver only computes a set number of modes closest to the central frequency ω_c. For $\sigma = 12 + 12i$, this cluster of numerical modes has moved close enough to the central frequency such that the fundamental QNM with the eigenfrequency $\widetilde{\omega}_m = (0.0688 - 0.00784i)\omega_p$ was not computed because the solver computed the number of modes it needed to before reaching it.

Due to the discontinuities of the Maxwell operator for the grating because of its periodicity, there are branch cuts in the complex plane near the real frequencies where diffraction orders become propagative. These branch cuts manifest themselves as evenly spaced patterns of modes as seen in Fig. 5.1b for $\mathrm{Re}(\widetilde{\omega}/\omega_p) \approx \{0.16, .33, 0.5, ...\}$. These patterns of modes orient themselves differently with different values of the ratio $\dfrac{\mathrm{Im}(\sigma)}{\mathrm{Re}(\sigma)}$. In particular, the "veil" of numerical modes, as coined by Vial in [32], that spawn from the origin of the complex plane, arrange themselves along the line $y = -\dfrac{\mathrm{Im}(\sigma)}{\mathrm{Re}(\sigma)}x$ [50, 84] before meeting the cluster of numerical modes described previously.

Using two different mode searches with different PML parameters, we find two different sets of modes : $\{\widetilde{\omega}_m\}_m$ with $\sigma = 8 + 10i$ and $\{\widetilde{\omega}'_m\}_m$ with $\sigma = 6 + 8i$. To identify the QNMs of one set, we compare the eigenfrequencies between the two sets. We consider that if the minimum difference between a mode $\widetilde{\omega}_m$ from the first set and any mode from the second set is inferior to a threshold value $\Delta\widetilde{\omega}$, then $\widetilde{\omega}_m$ is a QNM. In this case, the threshold value is equal to $10^{-3}\dfrac{\omega_p}{2\pi}$ for the simple reason that it is the lowest value that allows all 7 resonant QNMs featured in Fig. 4.7 to be identified by out criteria as QNMs. This is due to one QNM mode whose eigenfrequency is close to one of the branch cuts at $\mathrm{Re}(\widetilde{\omega}_m) \approx 0.165\omega_p$, where numerical modes aggregate close to the real axis. In Fig. 5.2a, we plot the complex mode spectra of the grating for a 30° incidence angle with $\sigma = 8 + 10i$ where the QNM as defined by the previous criteria are boxed in red. We can see that most of the modes we identify as QNMs have very low imaginary parts and are close to the real axis. The purpose of finding the QNMs is to single out the modes which represent the physical resonances of the system and which would yield a resonant peak or deep if they were to be excited. The previous chapters have shown that QNMs are not sufficient in order to reconstruct the field on a wide spectrum of frequencies, but identifying which modes are physical or purely numerical can be a way to get an idea of where QNMs might appear in general and where branch cuts modes might interfere with finding a QNM due to their accumulation.

In Fig. 5.2b, we plot the real part of the eigenfrequency of these modes and notice that the modes accumulate at frequencies where the permittivity takes particular values. The first accumulation point is at $\omega \to \omega_p/\sqrt{2}$ where the grating's Drude metal permittivity has the value $\varepsilon(\omega) \to -1$. These modes would correspond to the Surface Plasmon Resonance [22] of a plane air-Drude metal interface. The second accumulation point is at $\omega \to \omega_p$ where the permittivity $\varepsilon \to 0$. The permittivity remains complex with small imaginary parts.

The third accumulation point is at the pole $\omega = -i\gamma$ where the permittivity diverges. For these modes, the auxiliary field $\widetilde{\mathbf{p}}_\eta = (\varepsilon(\mathbf{r}, \widetilde{\omega}_m) - \varepsilon_\infty)\widetilde{\mathbf{e}}_m$ is divergent.

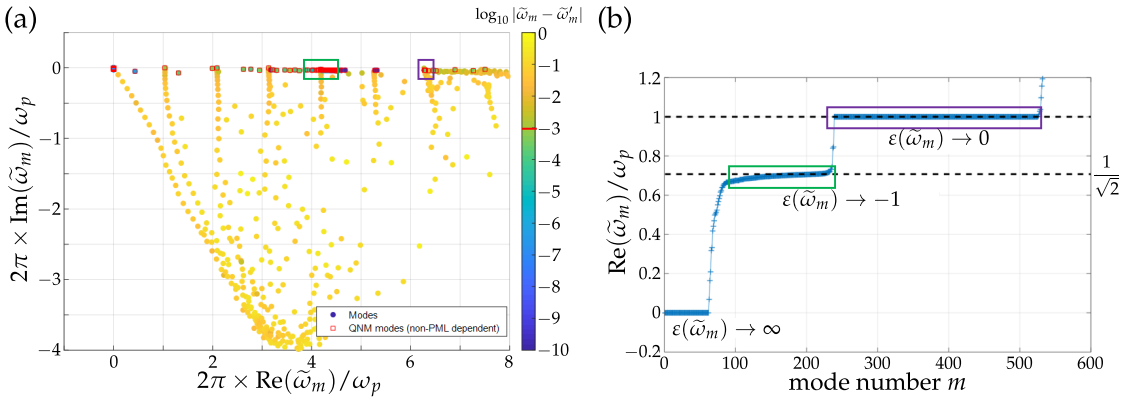

Figure 5.2: (a) Differentiation of QNM and numerical modes through two computations with different PML coefficients σ. We compute one set of modes $\{\widetilde{\omega}_m\}_m$ with $\sigma = 8 + 10i$ and the other set $\{\widetilde{\omega}'_m\}_m$ with $\sigma = 6 + 8i$. We consider QNM modes to be the modes whose eigenfrequencies verify $|\widetilde{\omega}_m - \widetilde{\omega}'_m| < 10^{-3}\dfrac{\omega_p}{2\pi}$. Accumulation points are circled. (b) Real part of $\widetilde{\omega}_m$ of the QNM modes. We can see several accumulation points at specific values of $\mathrm{Re}(\widetilde{\omega}_m)$.

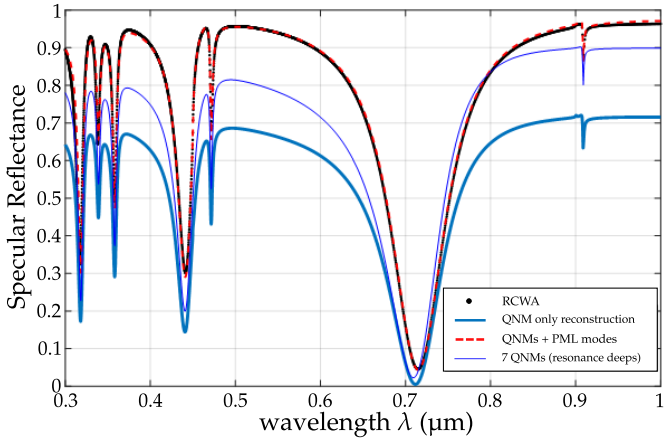

Figure 5.3: Influence of QNM modes on the reconstruction of the reflectance.

The fields of these modes are almost completely localized within the metal.

The accumulation points show a flaw in our approach to identify the QNM modes. Since the modes accumulate en masse at these specific points, the distance between two modes from two different mode searches could potentially be lower than the threshold value that we have chosen. These could potentially be "false positives" for QNM modes. Nevertheless, we choose to classify them as QNM modes in this instance.

We reconstruct the specular reflectance with all the newly identified QNM modes. In Fig. 5.3, we can see the influence of the additional QNM modes compared to the seven resonant peaks in the spectra. The additional QNMs have lowered the overall reconstructed reflectance of the spectra. This is to be expected since the modes that have been added are surface plasmon modes and Fabry-Pérot-type modes where the light is either confined on the surface of the metal or within the grooves. In this example, the overall inclusion of the QNM modes has confined light, while the addition of all the numerical modes such as

the PML modes on the branch cuts have overall scattered light into the far-field, raising the value of the specular reflectance. We can see that in this example, performing a reconstruction with more than 500 QNM modes has widened the gap between the reconstruction and the reference computation. This is a case where adding more modes has increased the error on the reconstruction overall.

In this section, we explored the influence of a single numerical parameter on the computation of the modes. We've shown that confirmed physical modes seldom saw a change in the value of their computed eigenfrequencies when the numerical parameter was changed slightly. We've tried to determine which modes are QNMs by seeing which modes do not see a significant change in their eigenfrequency when the parameter is changed. However, the existence of accumulation points and the accumulation of numerical modes at branch cuts could potentially hurt this criterion to identify QNM modes.

5.2 Spatial convergence of the field with the modal expansion

Eigenmodes are the solutions of the source-free Maxwell's equations at the complex frequency $\widetilde{\omega}_m$, where the eigenvector or the eigenfield is a purely spatial quantity. In the previous chapter, due to the periodic nature of the problem, we used the Fourier series of the reconstructed field above the grating to compute the specular reflectance; the latter is computed at a specific height h_0 above the top of the grating. Ideally, this quantity should not vary at all with the height where the Fourier coefficient is evaluated [75]. However, we will show that due to an incomplete or truncated basis of modes in the expansion, the reconstructed specular reflectance does vary significantly with this height. This section uses the same sign convention as the previous section for time-harmonic fields.

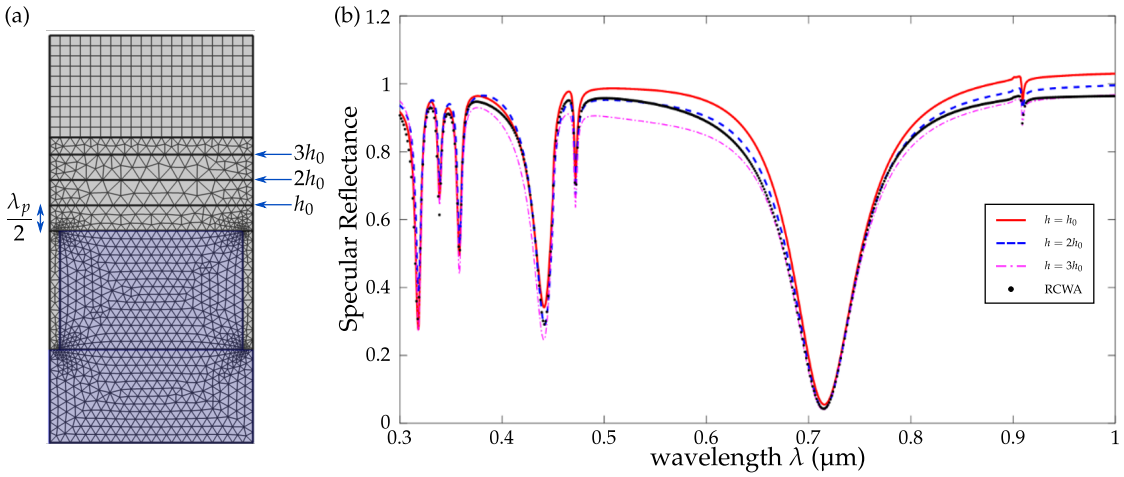

Figure 5.4: Variation of the reconstructed reflectance with M = 200 modes with different integration heights.

We modify our geometry slightly in order to verify the effect of the integration height. As pictured on the left side of Fig. 5.4, we add 3 lines in the geometry above the grating. The edges of triangular elements of the Finite Element mesh

will line up on these 3 lines that span the period of the grating. The first line is placed at a height $h_0 = \lambda_p/2 = 74.8\,\text{nm}$ above the grating, the second line is placed at a height of $2h_0$, and the third line at $3h_0$.

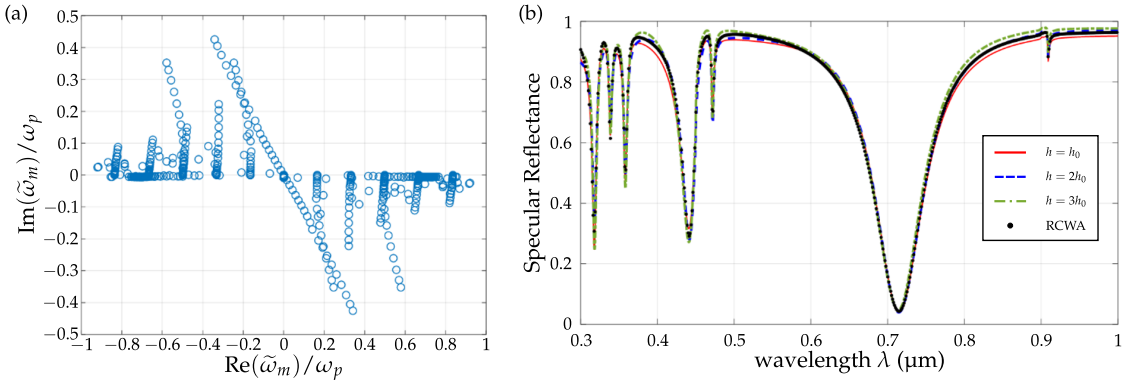

Figure 5.5: Variation of the reconstructed reflectance with M = 2000 modes with different integration heights.

In Fig. 5.4b, we plot the reconstructed specular reflectance spectra from all three computation heights with $M = 200$ modes, sampled from a single computation with a central frequency $\omega_c = 0.2\omega_p$. This small sample of mode contains all 7 resonant modes in the desired spectra as well as some PML modes from the rotated continuous spectrum and the first two branch cuts corresponding to the diffraction orders. We can see that with this truncated basis of modes, there is a lot of variance between the reflectance spectra computed at different heights, whether it be in or out of resonance. It would seem that the closer the integration height is to the top of the grating, the higher the computed reflectance when out of resonance. The resonance deeps seem to have the same depth from one computation to the next and seem offset by the non-resonant signal. The widest and deepest peak at 710 nm seems to be the one that is reconstructed with the most accuracy by all simulations.

In Fig. 5.5, we plot the spectra of the grating for all three integration heights with $M = 2000$ modes, sampled from both sides of the spectrum with $\text{Re}(\tilde{\omega}_m) \in [-\omega_p, \omega_p]$. Compared to the previous simulation, the variance between the different computations has lessened with the addition of modes in the expansion. This would seem to indicate that the expansion has converged in space to some degree as the number of modes increased.

In Fig. 5.6, we plot the modulus of the reconstructed scattered magnetic field in the unit cell plane for an illumination wavelength of $\lambda = 500\,\text{nm}$. The modal field reconstruction with 500 modes and beyond is plagued with numerical singularities that tarnish the field reconstruction on the metal's surface, not present in the real frequency simulations performed with COMSOL. The singularities correspond to select modes whose electromagnetic energy is confined intensely on the metal's surface.

In Fig. 5.7, we compare the normalized eigenfields of one of the resonant modes and one of the singularity modes. We can see that the fields have similar levels of intensity at different points in space. We can also see that the electric field for both modes is also intense at the top of the air groove. This is significant because the excitation coefficient is computed with an overlap integral evaluated

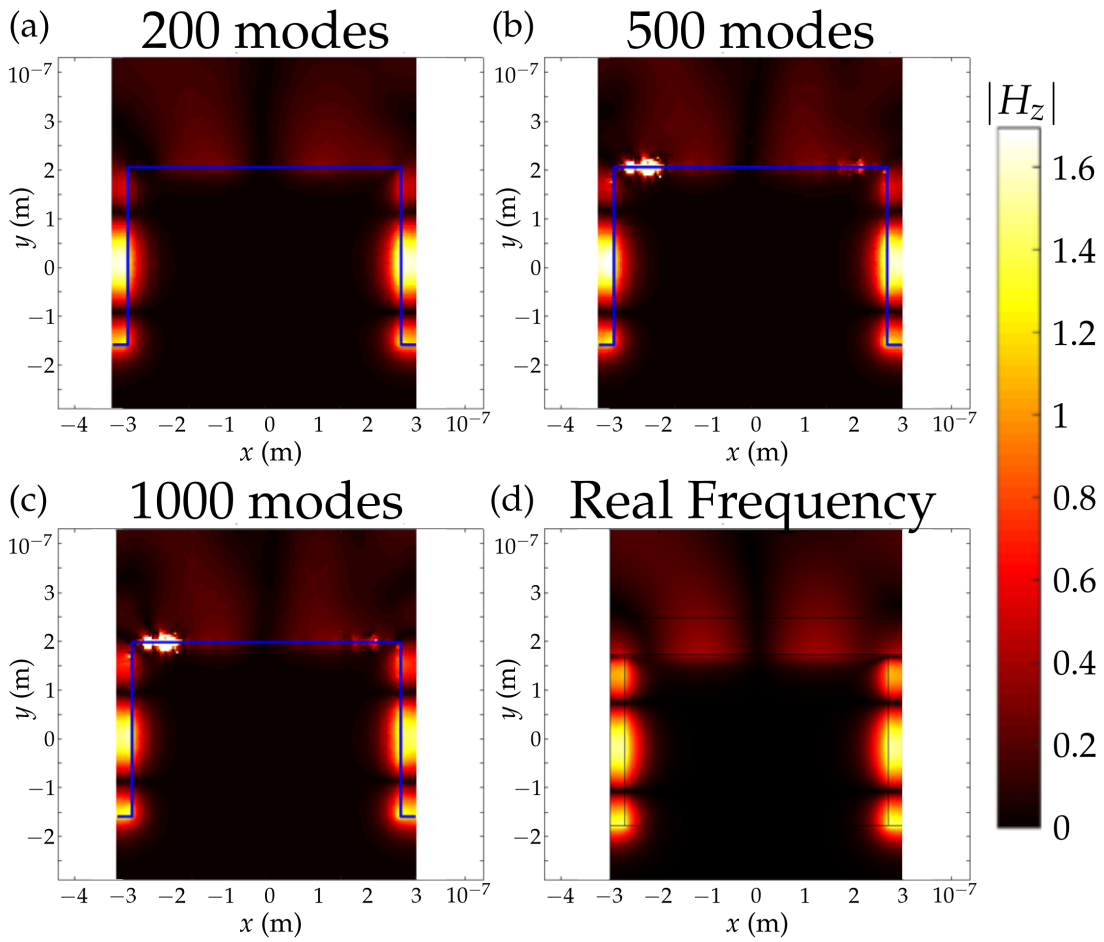

Figure 5.6: Modulus of the scattered magnetic field's z-component H_z computed at $\lambda = 500\,\text{nm}$ with the modal expansion using $M = 200, 500, 1000$ modes and a real frequency simulation using COMSOL.

within this region, and the overlap integral is between the normalized electric field of the mode and a plane wave that is exponentially decreasing as it dives deep into the groove. Thus, the value of the overlap integral is determined mostly by the eigenfield at the top of the groove. We evaluate the overlap integral and the excitation coefficient for both of these modes in Table 5.1. We can see that the modes have similar levels of excitation at $\lambda = 500\,\text{nm}$, which explains the visible hot spots on the grating's surface when we reconstruct. These singularities, which are not present in the real frequency simulation, indicate that if we were to compute the reflection at heights closer to the grating's surface, that the results would be affected by these hot spots.

	$\widetilde{\lambda}_m$[nm]	$\iiint_{V_{res}} \mathbf{e}_b \cdot \widetilde{\mathbf{e}}_{m,-\eta} d^3\mathbf{r}$	α_m	$\lvert\alpha_m\rvert$
Singularity mode	205.9 + 1.5i	-0.0011 - 0.0009i	-0.0042 - 0.0161i	0.0166
Resonant mode	714.1 + 38.7i	0.0334 + 0.7844i	0.0174 - 0.0294i	0.0342

Table 5.1: Eigenwavelength and excitation coefficient at an excitation wavelength $\lambda = 500\,\text{nm}$ for the two modes displayed in Fig. 5.7

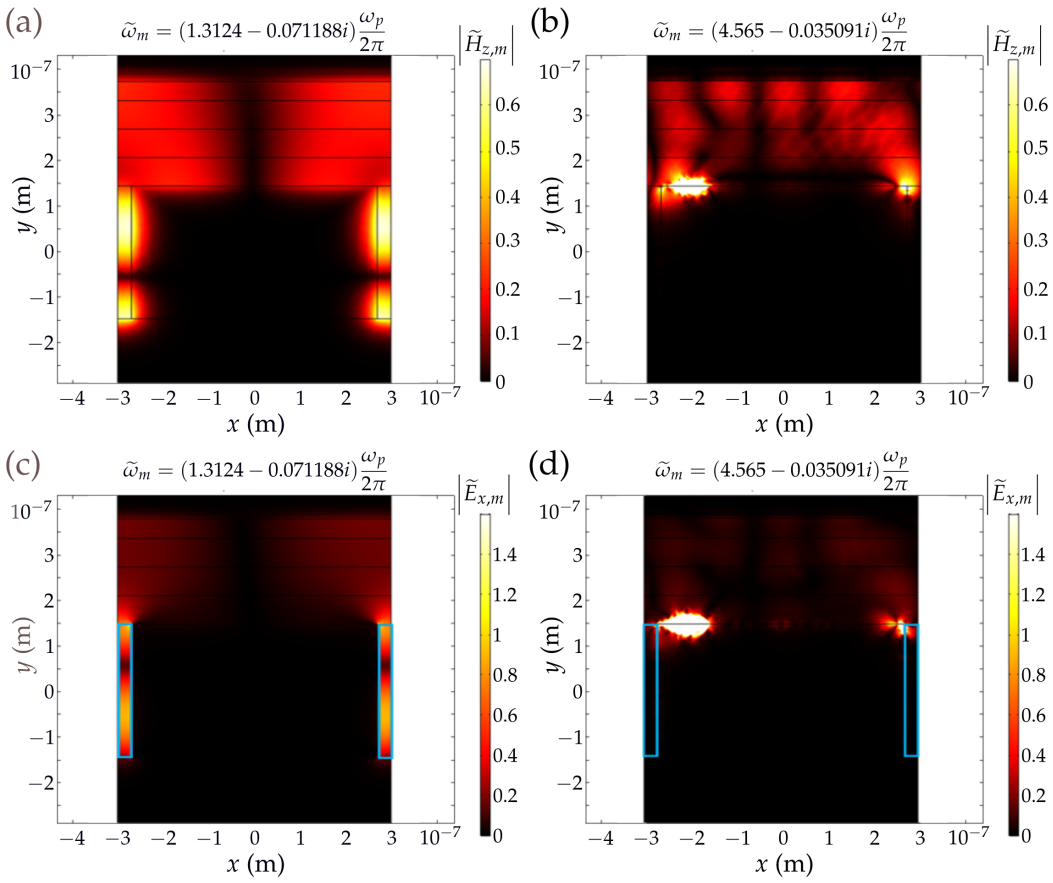

Figure 5.7: (a) Modulus of the normalized magnetic field of the QNM resonant at $\lambda = 714\,\text{nm}$ and (c) normalized modulus of the mode's electric field's x component. (b) Modulus of the normalized magnetic field of the singularity mode and (d) modulus of the electric field's x component of a singularity mode. In the bottom pictures, we contour the resonator volume V_{res} with blue boxes.

In order to measure, the effects of these hot spots, we decide to add a line to the geometry that is closer than the previous ones. We place a line at a height $\lambda_p/20 = h_0/10$ above the top of the grating. This forces the mesh to employ smaller triangular elements between the line and the top of the grating. Since the mesh has changed, we must perform the mode searching computation again.

However the change in the mesh, in particular the refinement of the mesh at the surface of the grating, has modified the catalog of modes we have computed. We reconstruct the scattered magnetic field with the 2000 modes we have computed this time and we can observe in Fig. 5.8 that the singularity modes are less prominent. The hot spots that were present in the previous simulations have greatly diminished. We suspect that these modes were purely numerical and linked to the finesse of the mesh near the metal's surface.

In Fig. 5.9, we plot the difference between the modulus of the reconstructed magnetic field and the magnetic field computed directly by COMSOL. We can see that the major differences between the two fields are localized mainly on the metal's surface. Lesser errors are found in the grooves, where the field is generally more potent. Relatively low errors are located above the grating, but these

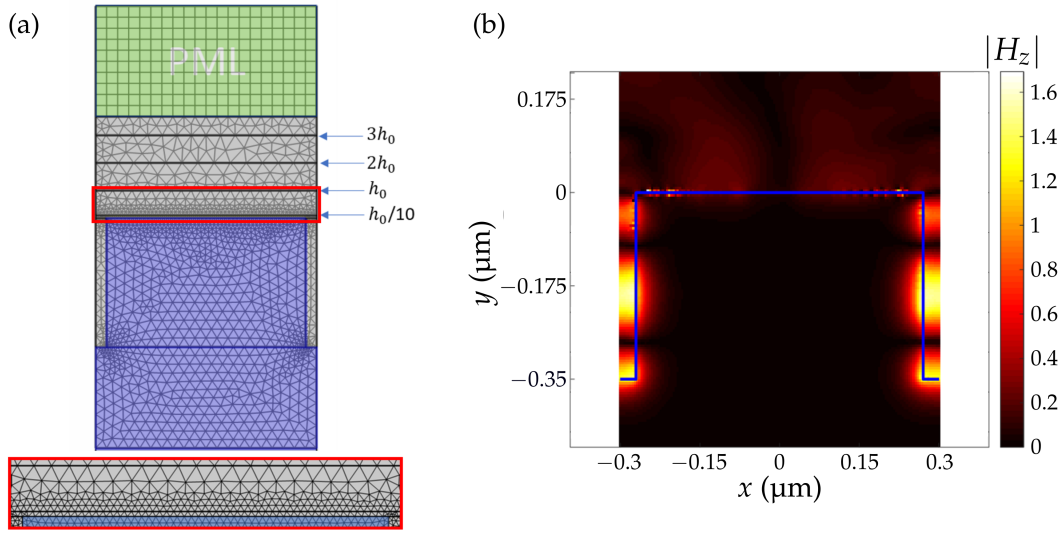

Figure 5.8: We added a line to the mesh that's close to the surface of the metal. We compute 2000 modes with this new mesh and reconstruct the field with those modes. We see that adding this line to the mesh has removed, or rather, minimized the computation of the potentially spurious modes like the one show in Fig 5.7.

errors have a more substantial effect on the reconstruction of quantities such as the specular reflection, because of the lowered intensity of the field in that area. The relative error in the grooves is low while the local relative error above the grating is rather high, in the order of 10%.

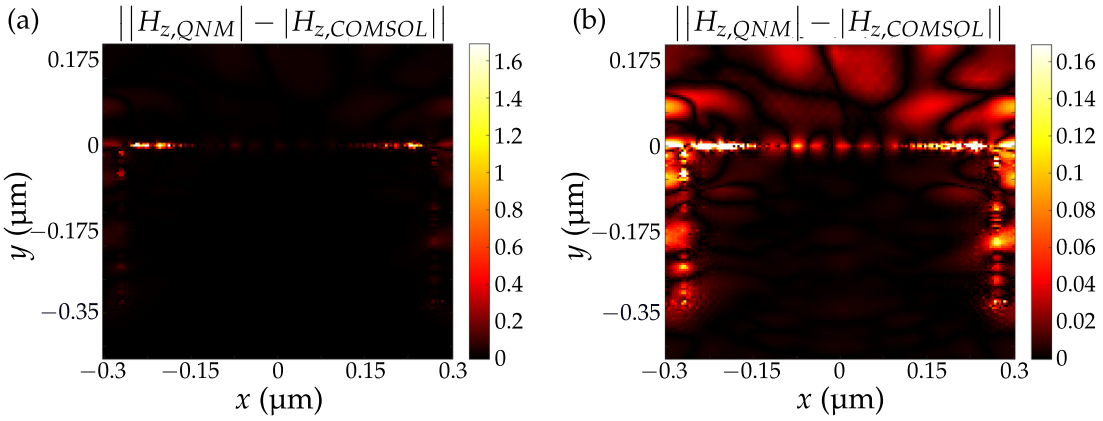

Figure 5.9: Difference between the scattered magnetic field directly computed with COMSOL and the modal reconstruction with 2000 modes. The color scale changes between (a) and (b). In the groove, the magnetic field can reach values of 1.6 as shown in Fig. 5.8b.

In this section, we have seen how the reconstructed field is not reconstructed to the same degree of precision in all points in space, using the quality of the reconstructed reflectance as a measure of the quality of the reconstruction. The convergence of the reconstructed field in space depends on the number of modes in

the expansion, provided that the modes in the expansion are computed correctly. We've shown that choices when meshing the structure lead to the computation of numerical modes, which can greatly affect the quality of the reconstructed field, especially, in this example, near the surface of the Drude-metal material. While the local error is high in some places, in some points reaching 10% or more, the overall error on the reflectance spectra averages to 2%.

5.3 Convergence speed of the modal expansion: finding the good sorting mechanism for modes

In this section, we will analyze the convergence speed of the modal expansion of the scattered electric field of a three-dimensional structure, the cylinder pictured in Fig. 5.10 with the aim of deciphering which components of the modal expansion and the modes' characteristics could be useful in determining the "fastest path to convergence", a way to reach a certain degree of convergence with the least modes necessary. While true convergence would require all the modes to be included in the expansion, identifying the few modes which are the most influential in order to accurately reconstruct the field could prove useful in analyzing resonator dynamics.

The cylinder is 400 nm high, has a radius of 240 nm and is made out of AlGaAs. The permittivity of this material is modeled with a Lorentz-pole model in the infrared:

$$\varepsilon(\omega) = \varepsilon_\infty - \frac{\omega_p^2}{\omega^2 - \omega_0^2} \tag{5.2}$$

with $\omega_p = 1.6910^{16}\text{rad} \cdot \text{s}^{-1}$, $\omega_0 = 5.5510^{15}\text{rad} \cdot \text{s}^{-1}$, and $\varepsilon_\infty = 1$. The cylinder is placed in an air background and the model is bounded by Perfectly Matched Layers. In this section, the sign convention has changed to $\exp(+i\omega t)$ for time-harmonic fields.

In this scattering experiment, we aim to define different mode sorting criteria in order to ascertain which modes are useful in the expansion and how many modes it takes to obtain a satisfactory value of the error. In the following section, we will define all the sorting criteria, give their advantages and disadvantages, and then compare their efficiency.

5.3.1 Criterion 1

Criterion 1 consists in ranking the modes according to the value of their excitation coefficient $\alpha_m(\omega)$. The modes will thus be ranked according to:

$$\beta_{1,m}(\omega) = |\alpha_m(\omega)| = \left| \left(\varepsilon_b - \varepsilon_\infty + \frac{\widetilde{\omega}_m}{\omega - \widetilde{\omega}_m} \Delta\varepsilon(\widetilde{\omega}_m) \right) \iiint_{V_{res}} \mathbf{E}_d \cdot \widetilde{\mathbf{E}}_m dV \right|. \tag{5.3}$$

The modes would be sorted according to the decreasing value of the criterion $\beta_{1,m}$ where the most influential mode according to this criterion would be the one with the highest value of $\beta_{1,m}$, the most excited mode, and so on.

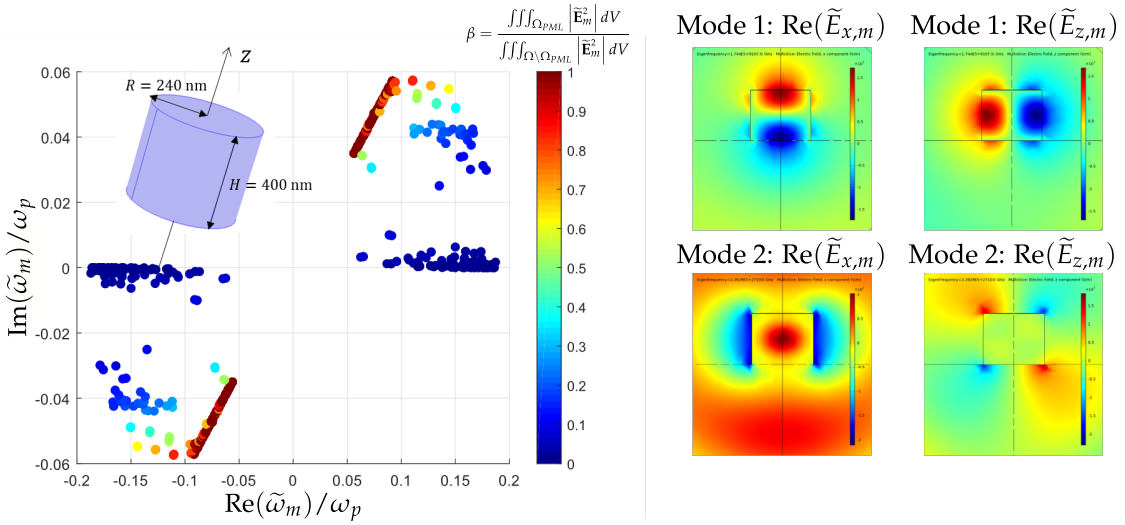

Figure 5.10: (a) Cylinder system and computed eigenmode spectra. The modes are colored according to how intense the field in the PML (inside the domain Ω_{PML}) is compared to everywhere else ($\Omega \setminus \Omega_{PML}$). (b) Normalized eigenfield of two QNMs.

This criterion is logical because it is a direct indicator of the mode's level of excitation. However, its flaws are that it's not a ranking that is universally valid for all excitation frequencies and polarizations. Not only that, but for isolated structures, like this cylinder in air, it would only take into account the field inside the resonator. For more complicated structures, it would depend on the choice of background permittivity and its corresponding background field which is logical since modes that aren't excited by the background field would correspondingly not be important to the reconstruction of the field.

In order to relieve ourselves of the dependency on the polarization of the background field $\mathbf{E}_d$, we will consider this alternative version of the criterion, where we replace the overlap integral from Eq. 5.3:

$$\beta'_{1,m}(\omega) = \frac{1}{3}\left|\left(\varepsilon_b - \varepsilon_\infty + \frac{\tilde{\omega}_m}{\omega - \tilde{\omega}_m}\Delta\varepsilon(\tilde{\omega}_m)\right)\right| \left(\left|\iiint_{V_{res}} \tilde{E}_{m,x} dV\right| + \left|\iiint_{V_{res}} \tilde{E}_{m,y} dV\right| + \left|\iiint_{V_{res}} \tilde{E}_{m,z} dV\right|\right). \tag{5.4}$$

This modified criterion should take into account all of the components of the mode's normalized eigenfield.

5.3.2 Criterion 2

Criterion 2 consists in comparing the fields inside the PML to the field outside the PML in order to distinguish the QNMs from the PML modes. Modes whose fields carry physical meaning like QNMs are damped inside the PML. PML modes have no such restrictions and the field in the PML is usually just as potent as the one in the physical domains, if not more.

We evaluate this criteria with the following formula:

$$\beta_{2,m} = \frac{\iiint_{\Omega_{PML}} |\widetilde{\mathbf{E}}_m|^2 dV}{\iiint_{\Omega \setminus \Omega_{PML}} |\widetilde{\mathbf{E}}_m|^2 dV}, \tag{5.5}$$

where Ω_{PML} is the PML domain, and Ω is the entire model's domain; $\Omega \setminus \Omega_{PML}$ thus corresponds to the physical domain.

The advantage of this criterion is that it does not depend on the incident plane wave in any way. It does not depend on its polarization nor its excitation frequency and only uses the modal fields. It also distinguishes the PML modes from the physical modes. However, it comes with a number of drawbacks. For one, we run the risk of deprioritizing PML modes that are beneficial in the reconstruction of the field. There could also potentially not be any useful sorting of the QNMs amongst themselves.

The criterion as defined in Eq. 5.5 does not consider the resonant nature of the modes. It thus could be potentially beneficial to modify the criterion so it takes the lineshape of a mode's resonance into account:

$$\beta'_{2,m}(\omega) = \left| \frac{\omega - \widetilde{\omega}_m}{\omega} \right| \frac{\iiint_{\Omega_{PML}} |\widetilde{\mathbf{E}}_m|^2 dV}{\iiint_{\Omega \setminus \Omega_{PML}} |\widetilde{\mathbf{E}}_m|^2 dV}. \tag{5.6}$$

With Eq. 5.6, we have weighted $\beta_{2,m}$ with an inverse Lorentzian lineshape that corresponds to the mode's eigenfrequency $\widetilde{\omega}_m$. This should allow us to distinguish which QNMs are resonant at the evaluation frequency ω.

5.3.3 Criterion 3

This criteria serves to evaluate the level of polarization of the resonator by a mode. The modal polarization vector $\widetilde{\mathbf{P}}_m = (\varepsilon(\widetilde{\omega}_m) - \varepsilon_\infty)\widetilde{\mathbf{E}}_m$ and the scattered polarization vector can be written:

$$\mathbf{P}_s(\mathbf{r}, \omega) = \sum_m^M \alpha_m(\omega) \widetilde{\mathbf{P}}_m. \tag{5.7}$$

A possible criterion to incorporate this idea could be:

$$\beta_{3,m} = |\alpha_m(\omega)| \iiint_{V_{res}} \left| \widetilde{\mathbf{P}}_m \right| dV. \tag{5.8}$$

This criterion would inherit the advantages and disadvantages of the first criterion in Eq. 5.3 with the added information that comes with the polarization vector. We also can make an alternative criterion like $\beta'_{1,m}$ in Eq. 5.4 which would not depend on the driving field:

$$\beta'_{3,m} = \beta'_{1,m} \iiint_{V_{res}} |\widetilde{\mathbf{P}}_m| dV. \tag{5.9}$$

5.3.4 Numerical Results and Comparison

We compute a total of 2000 modes and reconstruct the scattered field with the modal expansion. The truncated modal expansion includes a total of M mode,

sorted from 1 to M according to the previously defined criteria. The truncated scattered field is thus written:

$$\mathbf{E}_{s,M}(\mathbf{r},\omega) = \sum_{m=1}^{M} \alpha_m(\omega)\widetilde{\mathbf{E}}_m(\mathbf{r}). \tag{5.10}$$

We will evaluate the scattered field at the excitation wavelength $\lambda = 1550\,\text{nm}$. The error will be computed at a single frequency and we will compute the error on the scattered field of the modal reconstruction using a direct computation as a reference. We will compute the error value for a truncated basis of M modes as:

$$\text{Error}(\omega, M) = \frac{\iiint_{V_{res}} |\mathbf{E}_{s,M}(\mathbf{r},\omega) - \mathbf{E}_{s,ref}(\mathbf{r},\omega)|dV}{\iiint_{V_{res}} |\mathbf{E}_{s,ref}(\mathbf{r},\omega)|dV}. \tag{5.11}$$

We undertake to compute the error inside the cylinder since it is a domain that is not bordering a PML and that has finite dimensions.

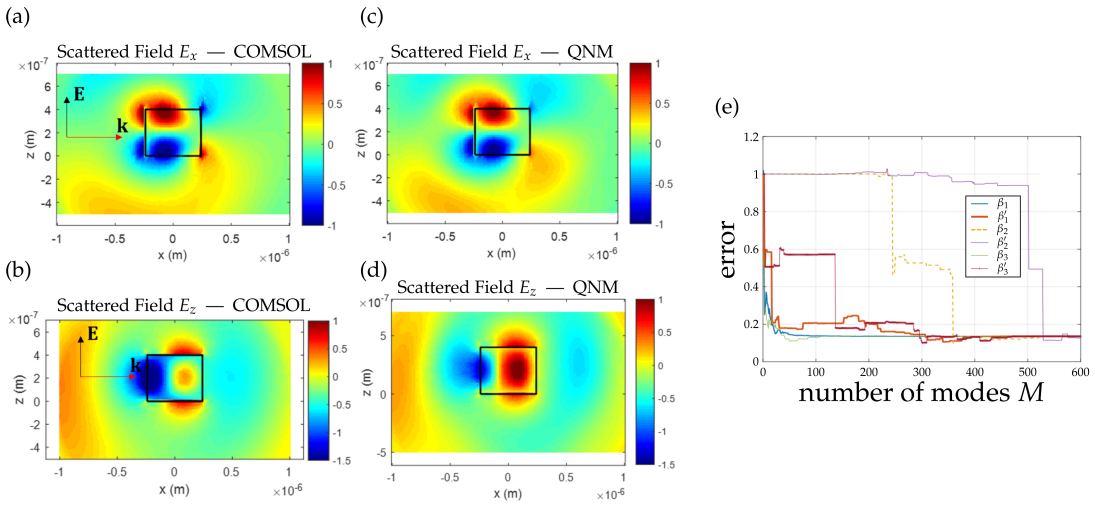

Figure 5.11: Real frequency simulation with COMSOL and modal reconstruction with 2000 modes of the scattered field for an incident plane wave propagating along x and polarized along z at $\lambda = 1550\,\text{nm}$. We plot the error as a function of the number of modes in the expansion using the sorting criteria $\beta_{1,m}, \beta'_{1,m}, \beta_{2,m}, \beta'_{2,m}, \beta_{3,m}, \beta'_{3,m}$.

We use two COMSOL models to perform the numerical experiment. The first model is used to compute the QNMs, and the reconstructed field at the $\lambda = 1550\,\text{nm}$ is computed using MATLAB-Livelink based on the MAN package[47]. The second is used to compute the scattered field directly using COMSOL.

Both models use the same mesh, meaning that extracting the scattered field or a QNM field in a particular domain yields matrices with the same dimensions. The overlap integrals and the computation of the excitation coefficients are performed in MATLAB using these matrices. We also compute the sorting criteria and the error values using those extracted matrices.

In Fig. 5.11 and 5.12, we plot the scattered field in the x-z plane for two different polarizations using the direct computation and the modal expansion with M = 2000 modes. On the right side of both figures, we plot the error value computed

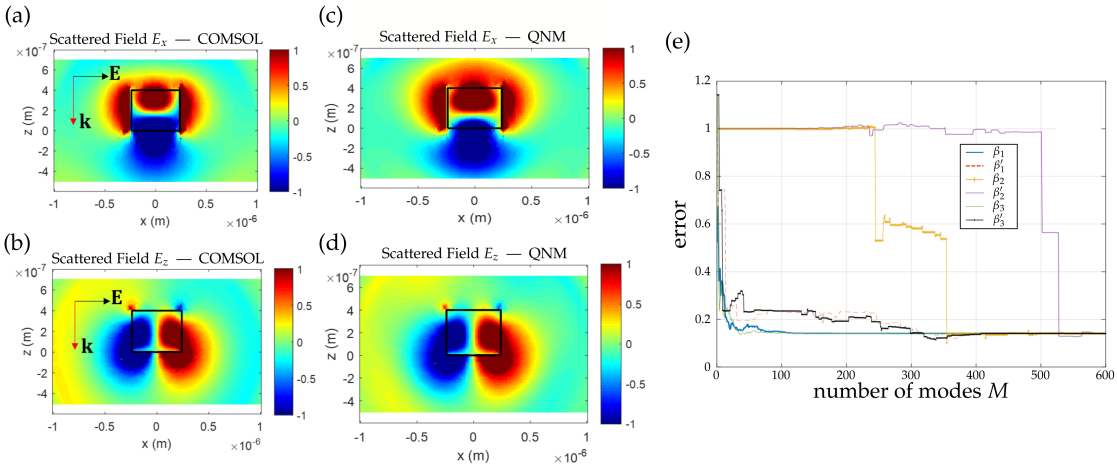

Figure 5.12: Real frequency simulation with COMSOL and modal reconstruction with 2000 modes of the scattered field for an incident plane wave propagating along z and polarized along x at $\lambda = 1550\,\text{nm}$. We plot the error as a function of the number of modes in the expansion using the sorting criteria $\beta_{1,m}, \beta'_{1,m}, \beta_{2,m}, \beta'_{2,m}, \beta_{3,m}, \beta'_{3,m}$.

as a function of the number of the modes in the expansion as sorted by all the different sorting criteria. The fastest convergence is obtained with $\beta_{1,m}$ and $\beta_{3,m}$ with about 40 modes out of 2000. The slowest convergence is obtained with the $\beta_{2,m}$ and $\beta'_{2,m}$ which we expected since they are the only criteria that did not take the excitation of the mode into account. All criteria converge towards the same value with less than 600 modes, beyond which there is little variation. From the huge spikes in the error value on some of the curves, we can see that about 10 or so modes have a large effect on the error, with 2 specific modes consistently creating huge spikes in the error value. When we try to sort modes without considering the driving field's characteristics, it inevitably slows down the convergence of the expansion.

We conclude that the reconstruction, for this example at least, is mostly carried by a minority of modes which inflicts macroscopic levels of change into the reconstructed field with their addition into the expansion. The most effective way of sorting modes for this purpose is to compute their levels of excitation, since it directly translates their effect on a spectrum or on the field as discussed in the supplementary information of [30]. Important modes that were not computed because they lie further within the complex plane, be they QNMs or numerical modes, could potentially reduce the error to lower levels. The main obstacle to convergence is not the number of modes but rather whether we have included the right modes into the expansion, and this requires a thorough and long exploration of the complex plane. Since we compute modes in bulk according to their proximity to a central frequency instead of their importance to the reconstruction, like it can be shown to be done [83], we end up spending computation time finding and spending storage to store them. For more computationally intensive electromagnetic simulations, like this three-dimensional example, storage and computational time stacks up quickly if we wish to simulate systems with a

reasonable level of accuracy.

5.4 Conclusion

In this chapter, we have highlighted some of the numerical issues that arise when reconstructing the scattered field with the modal expansion with many numerical modes, unlike most of the literature. Although we achieve accurate results over a large spectrum, the simulations are extremely sensitive to numerical parameters. PML modes, which have been shown to be relevant to the accuracy of the modal expansion vary widely with the parametrization of the PML. For the grating example, the reconstruction of the spectra depends heavily on the numerical modes. We have also shown that the convergence of the field of the QNM expansion is not uniform in space: the field converges better in some areas than others. The mesh of the finite element model changes the modes we compute and these modes can reach levels of excitation similar to physical modes which actually hold physical significance. These spurious modes can affect the reconstruction of the field spatially and their computation is prevented by finer meshing around the surface of metallic domains. The convergence curves that we have drawn show that the modes that are most important to the convergence of the expansion are the ones that are the most excited. In these examples, a very low proportion of modes lowered the error significantly.

Chapter 6

Interpolation-supplemented Quasinormal mode expansion

The optical response of micro- and nano-resonators is usually described by the excitation of a few resonant modes [14]. The quasinormal mode expansion consists in reconstructing that response from modal contributions. However, numerical simulations have shown that the expansion converges if a great number of modes are included in the expansion, some of them purely numerical in nature, as discussed in the literature [30, 34, 50] and the previous chapters. However, while the main resonant features of a spectra are reconstructed with few select modes that bear physical meaning, a broadband and effective convergence is conditioned by the addition of non-resonant physical modes and purely numerical modes [30, 35]. These additional modes usually act as a fine, broadband offset on the measured spectra when they are added in bulk. These and out-of-resonance modes greatly outnumber the resonant contribution and most articles in the literature usually only include the few essential modes [41, 38, 39, 40, 42, 43, 85, 86, 87], which allows for a clear modal analysis of physical phenomena.

The latter approach represents the expectations that a uninitiated user of the QNM expansion has. With that mindset, a user would expect each excited mode to represent a resonance that could be located on a spectrum, and the resonator response would then be described as a superposition of resonances with clear, documented origins, like Fabry-Pérot modes [63, 35], Bragg resonances [32], surface plasmon modes [35, 34], and dipolar, quadripolar modes [42]. It breaks down the resonator response as a competition between different engendered resonances whose resonance frequencies, spectral widths, and lifetimes are given by their complex frequencies. However, the accuracy of the reconstruction and the necessity of numerical modes hamper its overall usefulness. Methods to overcome these limitations are being investigated. For example, causality considerations can be used to offset the divergence of the field of Fabry-Pérot modes as they leave the cavity [63]. This allows the field for the 1D cavity to be reconstructed accurately inside and outside the cavity. In [36], the use of contour integrals in the complex plane allows for the computation of modes and very precise reconstructions with few modes.

We propose to overcome the convergence difficulty while considering a small number of modes. Here, the combined contribution of the many non-resonant and numerical modes is interpolated using a limited number of real frequency

computations of the field. Owing to the low variation within a given frequency range of the non-resonant contribution, it is easily interpolated from few interpolation points. In this chapter, we will present a method that uses the interpolation of a limited number of direct computations to achieve a convergent reconstruction of the field while employing the Quasinormal mode expansion, allowing for a modal analysis of the response. We will first present the interpolation schemes we use then put the interpolation into practice on a three-dimensional example.

Our system is described by a permittivity distribution $\varepsilon(\mathbf{r}, \omega)$. The modes of the system are the modes $\widetilde{\mathbf{E}}_m$ which solve the source-free Maxwell's equations at the complex frequency $\widetilde{\omega}_m$. With a finite number of modes, we can reconstruct the scattered field $\mathbf{E}_s^M$ at the real frequency ω:

$$\mathbf{E}_s^M(\mathbf{r}, \omega) \approx \sum_m^M \alpha_m(\omega) \widetilde{\mathbf{E}}_m(\mathbf{r}) \tag{6.1}$$

The expansion of the scattered field should converge towards the exact solution $\mathbf{E}_s$ as the number of modes $M \to \infty$ due to completeness [31]. This particular result has been demonstrated numerically [30] and a great number of the modes included in the expansion in those results bear no physical meaning. They are modes created from the use of Perfectly Matched Layers to satisfy the scattering boundary condition at $|\mathbf{r}| \to \infty$, oftentimes labelled PML modes [30, 32, 35], or other numerical modes spawned from the discretization of the continuous problem. While a resonant feature can usually be attributed to the excitation of a single mode, hundreds, if not thousands, of modes are necessary in order to converge towards the exact solution. In that sense, few physical modes can qualitatively reconstruct the sharper variations of a spectrum while an amalgamation of non-resonant physical modes [62], PML modes and other numerical modes build a generally monotone, smooth function of the frequency.

6.1 Interpolation scheme

In this chapter, the sign convention $\exp(+i\omega t)$ is used for time-harmonic fields. We denote $\mathbf{u}(\mathbf{r}, \omega)$ the difference between the exact solution and the Quasinormal mode expansion:

$$\mathbf{u}(\mathbf{r}, \omega) = \mathbf{E}_s(\mathbf{r}, \omega) - \mathbf{E}_s^M(\mathbf{r}, \omega) = \mathbf{E}_s(\mathbf{r}, \omega) - \sum_{m=1}^M \alpha_m(\omega) \widetilde{\mathbf{E}}_m(\mathbf{r}). \tag{6.2}$$

We consider real frequencies ω within the range $[\omega_i, \omega_f]$. If we include M quasinormal modes such that all the resonances within the spectra are accounted for, then the difference $\mathbf{u}(\mathbf{r}, \omega)$ is a slowly varying function within $[\omega_i, \omega_f]$. It can thus be conveniently approximated by a polynomial over the frequency spectra.

We choose N interpolation points scattered within $[\omega_i, \omega_f]$:

$$\omega_k = \omega_i + \frac{1 + x_k}{2}(\omega_f - \omega_i), \tag{6.3}$$

where x_k are points over the interval $[-1, 1]$. Many set of interpolation points can be used for an efficient interpolation, we have investigated three families of points:

- Chebyshev points [88]: $x_k = \cos\left(\frac{2k-1}{2N}\pi\right)$, $k = 1..N$
- Clenshaw-Curtis points [89]: $x_k = \cos\left(\frac{k-1}{N-1}\pi\right)$, $k = 1..N$
- Leja points defined recursively as (see [90]):

$$x_k = \text{argmax}_{x\in[-1,1]} \prod_{i=1}^{k-1} |x - x_i|,\ k > 1$$

  with $x_1 = 0$.

All these points avoid the Runge phenomenon [91] such that the interpolation of a smooth function, of class C^1 or higher, will converge exponentially without oscillating at the edges of the interpolation interval. Leja points have the advantage to constitute a nested sequence of points, such that a sequence of n Leja points would be included in the sequence of $n+1$ Leja points, meaning that increasing the number of interpolation points from n to $n+1$ would require only one new computation. For the other points, there exists a nested sequence with $N = 1, 3, 9, 27, \cdots$ for Chebyshev, and $N = 1, 3, 5, 9, 17, 33, \cdots$ for Clenshaw-Curtis points. $u(\mathbf{r}, \omega)$ can be approximated by the following polynomial:

$$\mathbf{u}(\mathbf{r}, \omega) \approx \sum_{k=1}^{N} \mathbf{u}_k(\mathbf{r})\varphi_k(\omega), \tag{6.4}$$

with $\mathbf{u}_k(\mathbf{r}) = \mathbf{u}(\mathbf{r}, \omega_k)$ and the Lagrange polynomials $\varphi_k(\omega) = \frac{\prod_{j=1,j\neq k}^{N} \omega - \omega_j}{\prod_{j=1,j\neq k}^{N} \omega_k - \omega_j}$.
The scattered field can thus be approximated as :

$$\mathbf{E}_s^I(\mathbf{r}, \omega) = \sum_{m=1}^{M} \alpha_m(\omega)\widetilde{\mathbf{E}}_m(\mathbf{r}) + \sum_{k=1}^{N} \mathbf{u}_k(\mathbf{r})\varphi_k(\omega). \tag{6.5}$$

The polynomial $\mathbf{u}(\mathbf{r}, \omega)$, composed of a sum of Lagrange polynomials, forces $\mathbf{E}_s^I(\mathbf{r}, \omega_k) = \mathbf{E}_s(\mathbf{r}, \omega_k)$ at all the interpolation frequencies ω_k: the interpolated field is thus equal to the reference field at the interpolation frequencies and will tend towards the value of the reference field near the interpolation frequencies, due to the continuity of the interpolated vector in frequency.

This interpolation method is linear meaning that it is scalable with the number of spatial points of the field. Meaning that the interpolation can be used for a complex-valued, multiple component vector, as well as values in space of that same vector. All the fields can be decomposed on their respective spatial components on the x-,y-, and z-axis: $\mathbf{E} = E_x\widehat{\mathbf{x}} + E_y\widehat{\mathbf{y}} + E_z\widehat{\mathbf{z}}$ and the same is true of $\mathbf{u}_k$:

$$\begin{aligned} \mathbf{u}_k &= u_{k,x}\widehat{\mathbf{x}} + u_{k,y}\widehat{\mathbf{y}} + u_{k,z}\widehat{\mathbf{z}} \\ &= (E_{s,x} - E_{s,x}^M(\mathbf{r}, \omega_k))\widehat{\mathbf{x}} + (E_{s,y} - E_{s,y}^M(\mathbf{r}, \omega_k))u_y\widehat{\mathbf{y}} + \\ &\quad (E_{s,z}(\mathbf{r}, \omega_k) - E_{s,z}^M(\mathbf{r}, \omega_k))u_z\widehat{\mathbf{z}}. \end{aligned} \tag{6.6}$$

We can thus write the interpolated function $\mathbf{u}$ as a sum of its interpolated spatial components: the interpolated field is a sum of the interpolation of the different spatial components of the field. Taking Eq. 6.4 and 6.6, we can write:

$$\begin{aligned} u(\mathbf{r},\omega) \approx \sum_{k=1}^{N} u_k \varphi_k(\omega) &= \sum_{k=1}^{N} (u_{k,x}\widehat{\mathbf{x}} + u_{k,y}\widehat{\mathbf{y}} + u_{k,z}\widehat{\mathbf{z}})\varphi_k(\omega) \\ &= \left(\sum_{k=1}^{N} u_{k,x}\varphi_k(\omega)\right)\widehat{\mathbf{x}} + \left(\sum_{k=1}^{N} u_{k,y}\varphi_k(\omega)\right)\widehat{\mathbf{y}} + \\ &\quad \left(\sum_{k=1}^{N} u_{k,z}\varphi_k(\omega)\right)\widehat{\mathbf{z}}. \end{aligned} \tag{6.7}$$

In the same way, we can interpolate the real and imaginary parts of the fields separately because the frequency ω is real and the Lagrange polynomial is thus a real function. Using Eq. 6.4, we can write:

$$u(\mathbf{r},\omega) \approx \sum_{k=1}^{N} u_k \varphi_k(\omega) = \sum_{k=1}^{N} \mathrm{Re}(u_k)\varphi_k(\omega) + i\sum_{k=1}^{N} \mathrm{Im}(u_k)\varphi_k(\omega). \tag{6.8}$$

6.2 Numerical Results

We call reference solution, the solution $\mathbf{E}_s$ computed directly by the finite element method with COMSOL Multiphysics software. We call the modal solution, the solution $\mathbf{E}_s^M$ computed with the modal expansion. The reference solution and the modes are computed with the same finite element mesh. We call the interpolated solution, the solution $\mathbf{E}_s^I$ computed with the equation (6.5). For the expression of α_m, we use the following formula

$$\alpha_m = \frac{\omega}{(\tilde{\omega}_m - \omega)} \int_\Omega (\varepsilon(\omega,\mathbf{r}) - \varepsilon_b)\, \mathbf{E}_{\mathrm{inc}}(\mathbf{r}) \cdot \mathbf{E}_m(\mathbf{r}) d\mathbf{r}. \tag{6.9}$$

The choice of formula will not matter in the following section because the resonator's materials is non-dispersive. The set of interpolation points we will use in the next section are the Chebyshev points.

6.2.1 Dielectric cylinder

We place a dielectric cylinder in an air background. The permittivity of the cylinder is non-dispersive with $\varepsilon = 12.25$. The cylinder is 400 nm high and has a radius of 240 nm, as pictured in Fig. 6.1a.

We first observe the field and the performance of the interpolation method on two points in space, A and B, in the x-z plane, as pictured in Fig. **??**. The driving field is a plane wave propagating downwards along the z-axis, polarized along the x-axis.

We compute a total of 50 modes. The real parts of the eigenwavelengths of the modes fall between 1500 nm and 2000 nm. In Fig. 6.1, we plot the eigenwavelengths in the complex plane as well as the electric field at position A computed with a real frequency simulation and with the modal expansion. We can see that the shape of the curves are similar and that the reference computation results seem offset by a almost constant amount compared to the modal reconstruction.

The difference between the two methods is plotted as well, and is a smooth function, with some slight variations around 1800 nm due to the slight shift in the peaks and dips of the modal reconstruction compared to the reference results. On the right side of Fig. 6.1, we plot the fields of 5 excited QNM modes. The sum of these modes reconstruct the main variations in the spectrum of interest. The addition of the other 45 modes has only slightly shifted the value of the electric field without modifying the overall variation of the electric field over the spectra. This is reminiscent of most demonstrations of the QNM expansion such as the modal reconstruction of the specular reflectance of the grating as shown in Fig. 4.11 in Chapter 4. The main seven resonances of the grating example corresponded to 7 dips in the reflectance, and remaining modes had mostly broadband effects on the reflectance spectrum. These modes were either numerical or with a resonance frequency outside of the frequency spectra of interest. If the spectra were wider than more modes be necessary in order to capture the variations.

In the next section, we will first focus on the convergence performance at the positions A and B.

6.2.2 Results at 2 specific points in the Geometry

Due to the smooth difference between the two different methods, it could be accurately interpolated with a few interpolation points. We plot in Figs. 6.1 and 6.2 the interpolated electric field using 15 interpolation points. The electric field is fairly well reconstructed on point A but not on point B, where the QNM reconstruction without interpolation differs greatly from the direct computation results. The x-component of the electric field is reconstructed with a shifted peak with the modal expansion, yet the error is still somewhat smooth and flat. For the z-component, the shape of the modal reconstruction spectra is missing a sharp variation compared to the direct computation. This major difference could be due to a missing mode that is resonant inside the spectral interval and relatively intense at point B, which we could attribute to a failure of the solver to find the necessary mode due to the coarse mesh or because the Perfectly Matched Layers prevent the mode from being discovered by the solver because the mode's eigenfrequency lies beyond the rotated continuous spectra of PML modes [32, 50]. Nevertheless, the interpolation has corrected this discrepancy between the two methods.

We can define the average relative error on an interpolated complex quantity X, which could be a component of the electric field for example, sampled over $N_{tot} = 100$ regularly paced points in the wavelength spectra $[1500\,\text{nm}, 2000\,\text{nm}]$ as

$$\langle \text{Error}_X \rangle = \frac{1}{N_{tot}} \sum_{p=1}^{N_{tot}} \frac{\left| X_S(\lambda_p) - X_S^I(\lambda_p) \right|}{\left| X_S(\lambda_p) \right|}, \tag{6.10}$$

where X_S represents the reference of the quantity X, and X^I the interpolated quantity. The superscript "I" will be used to designate interpolated quantities. The relative error on the scattered field vector is thus defined similarly to Eq.

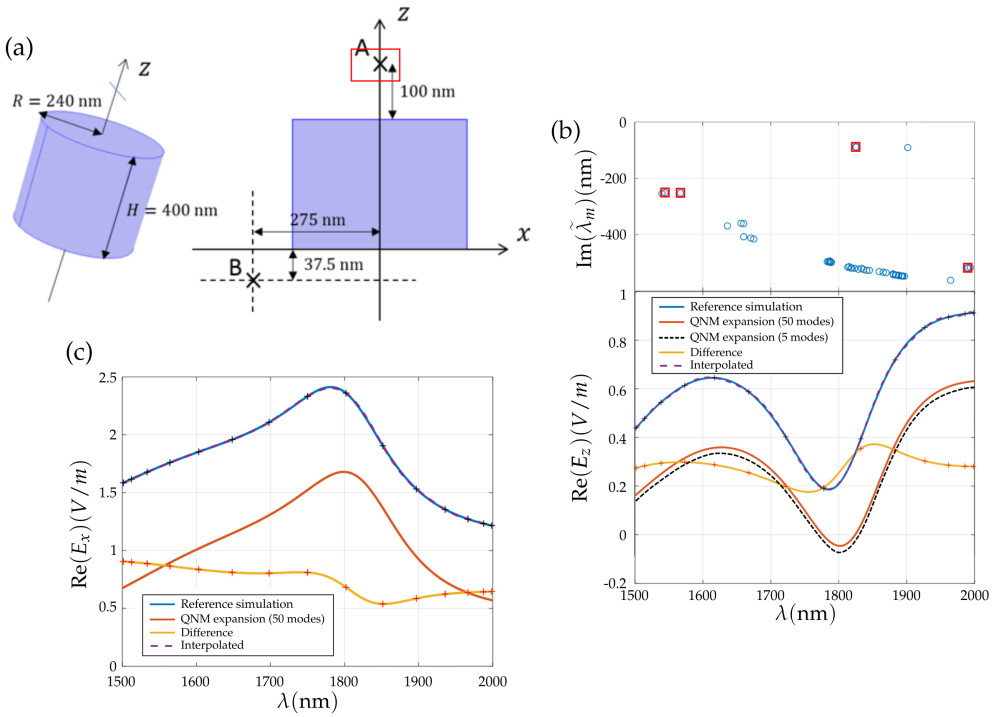

Figure 6.1: (a) Schematic of the cylinder geometry. Points A and B are two points in space on which the field will be computed. (b) (top panel) Complex mode spectra of the cylinder. The red squares indicate the 5 modes which contribute most to the expansion. (bottom panel) Interpolation of the real part of the x-component of the electric field at point A obtained with the modal expansion and with the direct computation (labeled "Reference simulation"). The difference between the two is also plotted. Modal reconstruction of the real part of x-component of the electric field with $M = 5, 50$ modes and for 5 modes for which the value of $|\alpha_m|$ were highest in the spectral interval $[1500\,\text{nm}, 2000\,\text{nm}]$. The black dotted lines denote the resonance wavelengths of the 5 modes. (c) Interpolation of the real part of the z-component of the electric field with 15 interpolation points at evaluation point A. The red crosses represent the location of the interpolation points. The crosses represent the interpolation points.

6.10:

$$\langle \text{Error}_E \rangle = \frac{1}{N_{tot}} \sum_{p=1}^{N_{tot}} \frac{\left|\left|\mathbf{E}_S(\lambda_p) - \mathbf{E}_S^I(\lambda_p)\right|\right|}{\left|\left|\mathbf{E}_S(\lambda_p)\right|\right|}. \tag{6.11}$$

The relative error on the spectra evaluated on point A and B and computed for $N = 5, 10, 15$ interpolation points over a spectrum. These values are displayed in Tables 6.1 and 6.2.

For point A, due to the general agreement in the variations of the two methods and the smoothness of the difference between the two methods, the field is well interpolated with at least 5 interpolation points. The relative error on the electric field falls to around 0.05 with 5 interpolation points. By doubling the number of interpolation points from 5 to 10, the relative error on the spectrum has been reduced threefold and going from the 10 to 15 interpolation points, the relative

X	$\langle \text{Error}_{E_x} \rangle$	$\langle \text{Error}_{E_z} \rangle$	$\langle \text{Error}_{\mathbf{E}} \rangle$
5 interpolation points	0.052	0.050	0.033
10 interpolation points	0.018	0.0065	0.011
15 interpolation points	0.0042	0.0027	0.0030

Table 6.1: Average relative error on the interpolated electric field at the evaluation point A. The spectra is plotted in Fig. 6.1

error value has been reduced by another factor 3. For point A, the error is quite low even with only 5 interpolation points due to the smooth value of the error across the spectrum. With 5 interpolation points, we reach an average error on the spectrum of 0.033 with only 50 modes, comprised only within the spectrum of interest which somewhat matches the error on the grating with 200 modes.

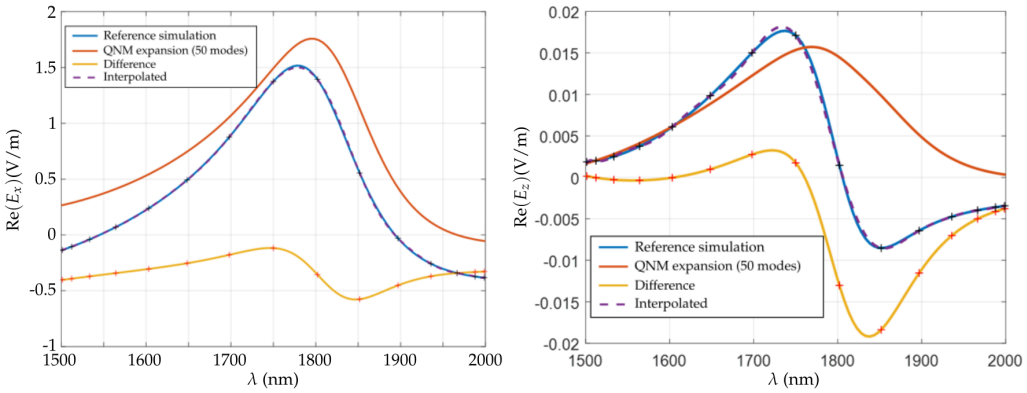

Figure 6.2: (Left) Interpolation of the real part of the x-component of the electric field with 15 interpolation points at evaluation point B. (Right) Interpolation of the real part of the z-component of the electric field with 15 interpolation points at evaluation point B. The red crosses represent the location of the interpolation points.

X	$\langle \text{Error}_{E_x} \rangle$	$\langle \text{Error}_{E_z} \rangle$	$\langle \text{Error}_{\mathbf{E}} \rangle$
5 interpolation points	0.11	0.53	0.11
10 interpolation points	0.043	0.16	0.043
15 interpolation points	0.0082	0.042	0.0082

Table 6.2: Average relative error on the interpolated electric field at the evaluation point B. The spectra is plotted in Fig. 6.2

The QNM expansion being less effective on point B in reconstructing the field, the error is much greater than on point A. Nevertheless, the interpolation has bridged the gap between the modal expansion and the direct computation, despite the very different results for the z-axis at this particular point in space. While the error on the vector is somewhat high, the average relative error fall below 0.01 with 15 interpolation points and the error on the z-component is below 0.05 with 15 interpolation points. The interpolation procedure was able to correct the high inaccuracy on the field at this point in space. The interpolation method has

shown that it could drastically reduce the errors on the spectra. As we have seen for point B, even when the reconstruction was somewhat inaccurate, the error was somewhat lessened by the interpolation method.

The error would surely decrease further as more interpolation points are used to interpolate the field. Previously, in order to make the modal expansion converge, we simply added more modes into the expansion. However, adding more modes does not guarantee that the reconstruction will be more accurate by simply adding a mode or two. The convergence curves found in the supplementary information of [30] show that the evolution of the error as more modes are added into the expansion is not monotonous. The error does trend towards decreasing as the number of modes in the expansion rises but not at a set speed. The same could be observed in the reconstruction of the specular reflectance of the grating in Chapter 4 of this thesis.

6.2.3 Convergence of the Interpolated QNM Expansion inside and outside the cylinder

In this section, we will explore the convergence in space of the interpolated QNM expansion inside a volume instead of single points in space and estimate the rate of convergence of the interpolation method. Since the interpolation method is scalable, we can just as easily interpolate a single point in space as we can multiple points. Numerically, this means that we interpolate each element of a matrix of points separately. We compute the electric field over the spectra $\lambda \in [1500\,\text{nm}, 2000\,\text{nm}]$ with the direct method and the modal expansion. Like in the previous section, we interpolate the field, this time for 279 points inside the cylinder. The number of points depends on the finesse of the mesh.

In Fig. 6.3, we plot the relative error:

$$\text{relative error}_{Ex}(\lambda) = \frac{\left|\text{Re}(E_x(\mathbf{r},\lambda)) - \text{Re}(E_x^I(\mathbf{r},\lambda))\right|}{\left|\text{Re}(E_x(\mathbf{r},\lambda))\right|} \tag{6.12}$$

for each of the 279 points in space when the interpolated field is constructed using 15 interpolation points. For most of the positions where the field is reconstructed, the error varies between 10^{-2} and 10^{-4}. The error rises for most points between 1800 and 1900 nm since that where the sharp variations of the difference between the modal expansion and the direct computation are usually located. For some wavelengths and some points in space, the error reaches relatively high values like $6\ 10^{-1}$.

We can integrate the relative error over the volume of the cylinder for a single frequency:

$$\text{Error}_{Vol} = \frac{1}{V_{cyl}} \iiint \frac{\left|\left|\mathbf{E}_S(\lambda) - \mathbf{E}_S^I(\lambda)\right|\right|}{||\mathbf{E}_S(\lambda)||} dV, \tag{6.13}$$

and we compute the mean integrated relative error like in the previous section with the following formula:

$$\langle \text{Error}_{Vol} \rangle = \frac{1}{V_{cyl}} \frac{1}{N_{tot}} \sum_{p=1}^{N_{tot}} \iiint \frac{\left|\left|\mathbf{E}_S(\lambda_p) - \mathbf{E}_S^I(\lambda_p)\right|\right|}{\left|\left|\mathbf{E}_S(\lambda_p)\right|\right|} dV. \tag{6.14}$$

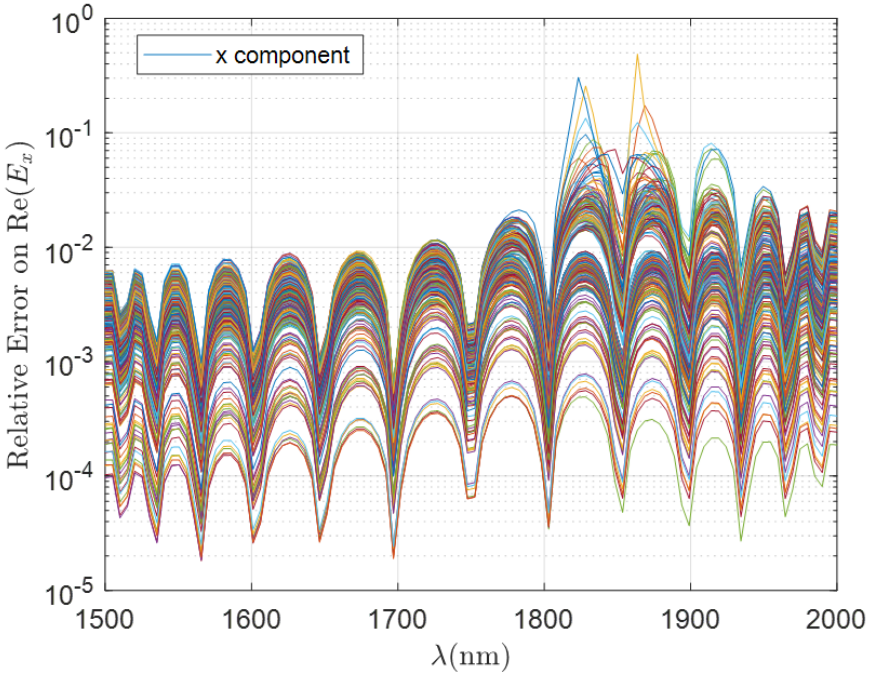

Figure 6.3: Relative error on the interpolation of the real part of the electric field's x-component with 15 interpolation points. Each curve corresponds to a different point in space.

We plot the mean integrated relative error on the spectra as a function of the number of interpolation points on Fig. 6.4. This error on the spectra falls below 10^{-2} for 11 interpolation points and keeps falling beyond that. This error is reduced by a factor of 10 for every 7 interpolation points added onto the expansion.

In Fig. 6.5, we show how the interpolation can be used to reconstruct the field in a matrix of points. We can see that the error is localized on the surface of the cylinder and above the cylinder and that the interpolation of the field has seemingly fixed most of these errors.

The interpolation method has supplemented the modal expansion and permitted it to converge on a great number of points in space on a wide frequency spectrum with comparable levels of accuracy to some of the results in the literature while keeping the number of modes in the expansion relatively low.

With the interpolation, we are sure to get a more precise reconstruction as more interpolation points are used. Like previously stated,including more modes does not necessarily assure that the error will decrease. However, this method only fixes the reconstructed field from a limited number of reference computation. Since we do not propose a method of analysis, more insight into the resonator dynamics is not gained. Users interested by the QNM expansion will have to gauge whether computing more modes is worth the time and computational effort. The out-of-resonance modes that the interpolation substitutes have been shown in previous chapters to be very influential, like the fundamental grating mode for the grating example in chapter 4 (see the 9th panel of Fig. 4.11) which visibly lowers the reflectance over the whole spectrum. This is the current trade off of the interpolation method. Perhaps the analysis of the interpolated difference between the modal expansion and reference computation could unearth res-

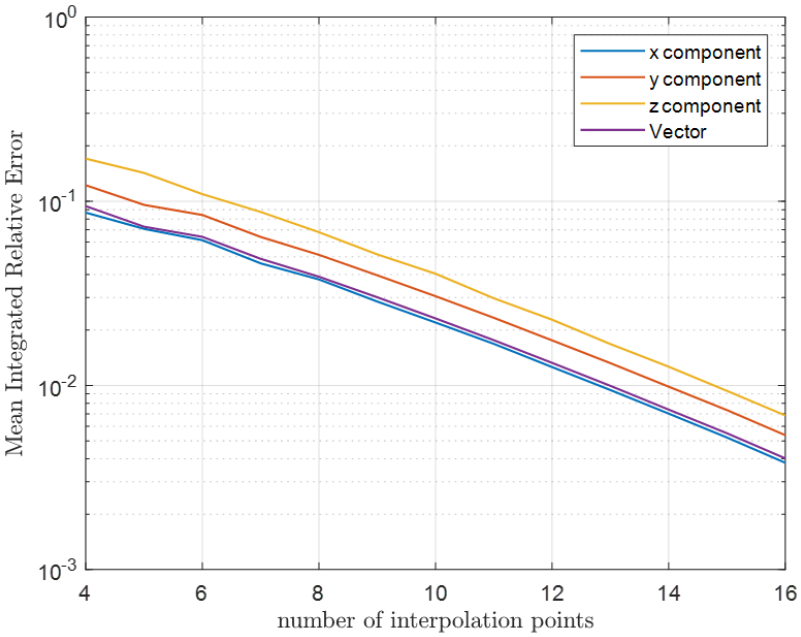

Figure 6.4: Mean Integrated Relative error of the interpolated scattered field computed across the spectrum, integrated inside the cylinder as a function of the number of interpolation points.

onator dynamics that the modal expansion has not captured?

6.3 Conclusion

In this chapter we've employed the use of direct computations on a few frequencies as a means to interpolate the reconstructed field with the modal expansion. In the case where the variations in a given spectrum are accurately reconstructed with very few modes, this could be a viable method to reduce the error on QNM reconstruction, successfully approximating the contribution from numerical modes and non-resonant contributions. However, this comes at a price, this method sacrifices the non-reliance of the modal expansion on the excitation. However, the increased accuracy gain is well worth the additional time spent on the direct computations, especially in the case of high-Q resonances, which are spectrally very fine and would require appropriate an adequate amount of direct computations to properly resolve while the computations of these sharp variations would be analytic with the modal expansion.

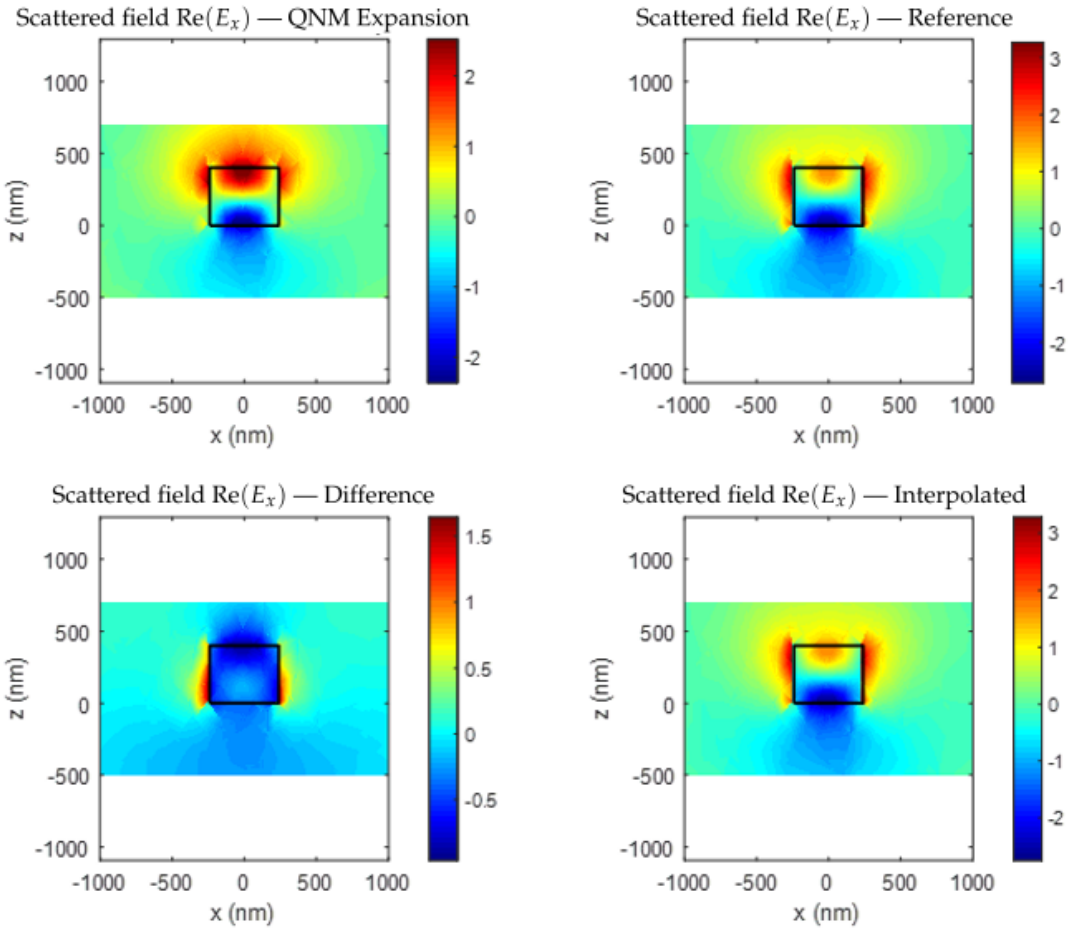

Figure 6.5: We reconstruct the field at $\lambda = 1828\,\text{nm}$. (Top left) Reconstructed scattered electric field x-component in the xz-plane. (Top right) Scattered electric field x-component in the xz-plane using a real frequency computation. (Bottom left) Difference between the scattered field computed with the direct computation and the modal expansion. (Bottom right) Interpolated Scattered field with 15 interpolation points.

Appendix A

Completeness of the Fabry-Pérot Cavity

This demonstration will be considering the one-dimensional case of the Fabry-Pérot cavity. The goal of the demonstration is to show that the Green's function, which describes the interaction between a light source and the inhomogenous medium, can be expressed as a sum of its modes, which are the poles of the Green's function.

We consider here a semi-infinite domain $\Omega = [0, +\infty[$ with a Dirichlet boundary condition at 0, and acts as a symmetry plane. The Sommerfeld condition is applied at infinity:

$$\lim_{x \to +\infty} \frac{\partial \mathbf{u}}{\partial \mathbf{n}} - i\omega \mathbf{u} = 0, \tag{A.1}$$

where $\mathbf{u}$ is a field and $\mathbf{n}$ is the unit vector along x pointing outwards from the resonator, ω is a normalized dimensionless frequency and the demonstration assumes that the celerity $c = 1$.

The scalar Green's function in this one-dimensional case in the time harmonic domain is described as:

$$(-\omega^2 \rho - \frac{\partial^2}{\partial x^2}) \widetilde{G}(x, y; \omega) = \delta(x - y), \tag{A.2}$$

where y is a position in space, δ is the Dirac function and $\rho(x) = n(x)^2$, where $n(x)$ is the refractive index. A practical way to compute Green's function in 1-D is to find two intermediate functions $f(\omega, x)$ and $g(\omega, x)$ that satisfy the following requirements:

$$\begin{cases} (-\omega^2 \rho - \dfrac{\partial^2}{\partial x^2}) f(\omega, x) = 0, \text{ for } x \in [0, +\infty[\\ (-\omega^2 \rho - \dfrac{\partial^2}{\partial x^2}) g(\omega, x) = 0, \text{ for } x \in [0, +\infty[\\ f(\omega, x = 0) = 0 \\ \lim\limits_{x \to +\infty} g(\omega, x) = e^{i\omega x}. \end{cases} \tag{A.3}$$

f and g are not unique. We define the wronskian as:

$$W(\omega) = g(\omega, x) \frac{\partial}{\partial x} f(\omega, x) - f(\omega, x) \frac{\partial}{\partial x} g(\omega, x). \tag{A.4}$$

It can be shown that the Wronskian is independent of x by computing its derivative along x and showing that it is null using Eq. A.3 and that the Green's function is equal to:

$$\widetilde{G}(x,y:\omega)\begin{cases} f(\omega,x)g(\omega,x)/W(\omega), & 0<x<y, \\ g(\omega,x)f(\omega,x)/W(\omega), & 0<y<x. \end{cases} \tag{A.5}$$

By construction, this expression of the Green's function satisfies both the Dirichlet condition through f and the Sommerfeld condition at infinity through g. The zeros of the wronskian $W(\omega)$ are the resonant frequencies $\widetilde{\omega}_m$. When $\omega = \widetilde{\omega}_m$, we have:

$$g(\widetilde{\omega}_m,x)\frac{\partial}{\partial x}f(\widetilde{\omega}_m,x) = f(\widetilde{\omega}_m,x)\frac{\partial}{\partial x}g(\widetilde{\omega}_m,x). \tag{A.6}$$

When we divide by fg and integrate, we obtain:

$$g(\widetilde{\omega}_m,x) = Cf(\widetilde{\omega}_m,x) \tag{A.7}$$

meaning that f and g are proportianal with C being a constant. We can choose f such that $C = 1$ and:

$$g(\widetilde{\omega}_m,x) = f(\widetilde{\omega}_m,x). \tag{A.8}$$

Let us assume that $\widetilde{\omega}_m$ is a zero of multiplicity 1 of W, then we have using the Taylor-expansion:

$$W(\omega) = \frac{dW}{d\omega}(\widetilde{\omega}_m)(\omega-\widetilde{\omega}_m) + ... \tag{A.9}$$

And we can deduce the residue of $\widetilde{G}$ arounf the pole $\widetilde{\omega}_m$:

$$R_m = f(\widetilde{\omega}_m,x)g(\widetilde{\omega}_m,x)/\frac{dW}{d\omega}(\widetilde{\omega}_m) \tag{A.10}$$

In section II.C of [31], this quantity is equal to :

$$R_m = \frac{f_m(x)f_m(x)}{2\widetilde{\omega}_m\langle\langle f_m|f_m\rangle\rangle}, \tag{A.11}$$

where $f_m(x) = f(\widetilde{\omega}_m,x)$ and

$$\langle\langle f_m|f_m\rangle\rangle = \int_0^{+\infty}\rho(x)f_m^2(x)dx. \tag{A.12}$$

To prove the completeness of QNM modes, we perform an inverse Fourier transform of the time-harmonic Green's function:

$$G(x,y,t) = \frac{1}{2\pi}\int_{-\infty}^{+\infty}\widetilde{G}(x,y,\omega)e^{-i\omega t}dt. \tag{A.13}$$

This integral can be computed using a contour $\mathcal{C}$ shaped like the half disk:

$$\mathcal{C} = [-R,R]\cup\{Re^{i\theta},\theta\in[-\pi,0]\}. \tag{A.14}$$

with $R \to \infty$. The residue theorem for this contour gives us:

$$\int_{\mathcal{C}} \widetilde{G}(x,y,\omega)e^{-i\omega t}dt = 2i\pi \sum_{\widetilde{\omega}_m \in \mathcal{C}} R_m e^{-\widetilde{\omega}_m t}. \tag{A.15}$$

Provided that are no branch cuts in the area of the complex plane enclosed by the contour and that

$$\lim_{|\mathrm{Im}(\omega)|\to+\infty} \widetilde{G}(x,y,\omega) = 0, \tag{A.16}$$

we can show that for $R \to \infty$:

$$G(x,y,t) = -i\sum_m R_m e^{-i\widetilde{\omega}_m t} = \frac{i}{2}\sum_m \frac{f_m(x)f_m(y)}{\widetilde{\omega}_m \langle\langle f_m | f_m \rangle\rangle} e^{-i\widetilde{\omega}_m t}, \tag{A.17}$$

The Green's function satisfies the initial condition

$$\rho(x)\frac{\partial G}{\partial t}(x,y,t=0^+) = \delta(x-y). \tag{A.18}$$

Using Eq. A.17 and A.18, we obtain the relation proving completeness:

$$\frac{1}{2}\sum_m \rho(x)\frac{f_m(x)f_m(y)}{\langle\langle f_m | f_m \rangle\rangle} = \delta(x-y), \tag{A.19}$$

showing that the field can be written as a sum of the resonant contributions, the quasinormal modes of the structure defined by the permittivity distribution $\rho(x)$, which make the field diverge when evaluated at their eigenfrequency. In the case of the Fabry-Pérot cavity, where the permittivity distribution $\rho(x)$ is defined as :

$$\rho(x) = \begin{cases} n_1^2 = 1, & |x| > a, \\ n_2^2, & |x| < a. \end{cases} \tag{A.20}$$

In this example, the functions f and g that satisfy the requirements are:

$$f(\omega,x) = \begin{cases} \alpha_f(\omega)sin(\omega x) + \beta_f(\omega)cos(\omega x),\ x > a, \\ sin(\omega n_2 x),\ x < a, \end{cases} \tag{A.21}$$

$$g(\omega,x) = \begin{cases} e^{i\omega x},\ x > a, \\ \alpha(\omega)sin(n_2\omega x) + \beta(\omega)cos(n_2\omega x),\ x < a, \end{cases} \tag{A.22}$$

with

$$\alpha_f(\omega) = \sin(\omega n_2 a)\sin(\omega a) + n_2\cos(\omega n_2 a)\cos(\omega a), \tag{A.23}$$

$$\beta_f(\omega) = \sin(\omega n_2 a)\cos(\omega a) + n_2\cos(\omega n_2 a)\sin(\omega a), \tag{A.24}$$

$$\alpha(\omega) = e^{i\omega a}\left(\sin(\omega n_2 a) + \frac{i}{n_2}\cos(\omega n_2 a)\right), \tag{A.25}$$

$$\beta(\omega) = e^{i\omega a}\left(\cos(\omega n_2 a) + \frac{i}{n_2}\sin(\omega n_2 a)\right). \tag{A.26}$$

f and g are found by considering them as a sum of sine and cosine functions on each interval. The wronskian can thus be expressed as

$$W(\omega) = \omega n_2 \beta(\omega). \tag{A.27}$$

For $x < y < a$, the Green function can be expressed as:

$$\widetilde{G}(x, y, \omega) = sin(\omega n_2 x) \frac{\alpha(\omega)\sin(\omega n_2 y) + \beta(\omega)\cos(\omega n_2 y)}{\omega n_2 \beta(\omega)}. \tag{A.28}$$

$\beta(\omega)$ and $\alpha(\omega)$ can be written with exponentials:

$$\beta(\omega) = e^{i\omega a}\left[e^{i\omega n_2 a}\left(\frac{1}{2} - \frac{1}{2n_2}\right) + e^{-i\omega n_2 a}\left(\frac{1}{2} + \frac{1}{2n_2}\right)\right], \tag{A.29}$$

$$\alpha(\omega) = e^{i\omega a}\left[e^{i\omega n_2 a}\left(-\frac{i}{2} + \frac{1}{2n_2}\right) + e^{-i\omega n_2 a}\left(\frac{i}{2} + \frac{1}{2n_2}\right)\right]. \tag{A.30}$$

We can express the Green function using exponentials as well:

$$\begin{aligned}\widetilde{G}(x, y; \omega) = &\frac{e^{i\omega n_2(-a+y+x)}\left(\frac{1}{4i} + \frac{1}{4in_2}\right) + e^{i\omega n_2(a+x-y)}\left(\frac{1}{4i} - \frac{1}{4in_2}\right)}{n_2\omega\left[e^{i\omega n_2 a}\left(-\frac{1}{2} - \frac{1}{2n_2}\right) + e^{-i\omega n_2 a}\left(\frac{1}{2} + \frac{1}{2n_2}\right)\right]} \\ &+ \frac{e^{i\omega n_2(-a-x+y)}\left(-\frac{1}{4i} - \frac{1}{4in_2}\right) + e^{i\omega(a-x-y)}\left(-\frac{1}{4i} + \frac{1}{4in_2}\right)}{n_2\omega\left[e^{i\omega n_2 a}\left(\frac{1}{2} - \frac{1}{2n_2}\right) + e^{-i\omega n_2 a}\left(\frac{1}{2} + \frac{1}{2n_2}\right)\right]}\end{aligned} \tag{A.31}$$

We consider here a complex frequency $\omega = \omega_R + i\omega_I$ with $\omega_I < 0$. The denominator of $\widetilde{G}$ is equivalent at large $|\omega_I|$ and $n_2 \neq 1$ to :

$$|\text{Denominator}(\widetilde{G})| \equiv \frac{1}{n_2\omega}\left|\frac{1}{2} - \frac{1}{2n_2}\right| e^{-\omega_I n_2 a}. \tag{A.32}$$

Whereas, the numerator will increase less quickly than the denominator for large $|\omega_I|$ due to the condition $x < y < a$. For large enough $|\omega_I|$, we obtain:

$$|\widetilde{G}| \leq \left|\frac{C}{n_2\omega}\right| \tag{A.33}$$

with C a constant. The limit of $|\widetilde{G}|$ is thus equal to 0 and thus the completeness of the QNM basis is proven inside the cavity (a similar computation can be conducted for $y < x < a$).

Now, we consider the case x<a, y>a. We have

$$\widetilde{G}(x, y; \omega) = \frac{\sin(\omega n_2 x)e^{i\omega y}}{n_2\omega\left[e^{i\omega n_2 a}\left(\frac{1}{2} - \frac{1}{2n_2}\right) + e^{-i\omega n_2 a}\left(\frac{1}{2} + \frac{1}{2n_2}\right)\right]} \tag{A.34}$$

For large ω_I, we get

$$|\widetilde{G}(x,y;\omega)| \equiv C\frac{1}{n_2\omega}\frac{e^{-\omega_I(n_2x+y)}}{e^{-\omega_I(n_2a+a)}}. \tag{A.35}$$

As soon as $n_2x + y > n_2a + a$, the limit of $\widetilde{G}$ is infinite instead of 0 and there is no completeness outside of the cavity.

Bibliography

[1] M. Shimomura and T. Sawadaishi, "Bottom-up strategy of materials fabrication: a new trend in nanotechnology of soft materials," *Current Opinion in Colloid and Interface Science*, vol. 6, no. 1, pp. 11 – 16, 2001.

[2] D. Rizzo, D. Prezzi, A. Ruini, V. Nagyte, A. Keerthi, A. Narita, U. Beser, F. Xu, Y. Mai, X. Feng, K. Müllen, E. Molinari, and C. Casiraghi, "Multiwavelength raman spectroscopy of ultranarrow nanoribbons made by solution-mediated bottom-up approach," *Phys. Rev. B*, vol. 100, p. 045406, Jul 2019.

[3] H.-D. Yu, M. D. Regulacio, E. Ye, and M.-Y. Han, "Chemical routes to top-down nanofabrication," *Chem. Soc. Rev.*, vol. 42, pp. 6006–6018, 2013.

[4] Y. A. Diaz Fernandez, T. A. Gschneidtner, C. Wadell, L. H. Fornander, S. Lara Avila, C. Langhammer, F. Westerlund, and K. Moth-Poulsen, "The conquest of middle-earth: combining top-down and bottom-up nanofabrication for constructing nanoparticle based devices," *Nanoscale*, vol. 6, pp. 14605–14616, 2014.

[5] D. K. Armani, T. J. Kippenberg, S. M. Spillane, and K. J. Vahala, "Ultra-high-q toroid microcavity on a chip," *Nature*, vol. 421, pp. 925–928, Feb 2003.

[6] B.-S. Song, T. Asano, S. Jeon, H. Kim, C. Chen, D. D. Kang, and S. Noda, "Ultrahigh-q photonic crystal nanocavities based on 4h silicon carbide," *Optica*, vol. 6, pp. 991–995, Aug 2019.

[7] A. Klinkova, H. Thérien-Aubin, A. Ahmed, D. Nykypanchuk, R. M. Choueiri, B. Gagnon, A. Muntyanu, O. Gang, G. C. Walker, and E. Kumacheva, "Structural and optical properties of self-assembled chains of plasmonic nanocubes," *Nano Letters*, vol. 14, no. 11, pp. 6314–6321, 2014. PMID: 25275879.

[8] M. N. M. N, U. Hashim, M. K. Md Arshad, A. R. Ruslinda, S. F. A. Rahman, M. F. M. Fathil, and M. H. Ismail, "Top-down nanofabrication and characterization of 20 nm silicon nanowires for biosensing applications," *PLOS ONE*, vol. 11, pp. 1–21, 03 2016.

[9] F. Vollmer, D. Braun, A. Libchaber, M. Khoshsima, I. Teraoka, and S. Arnold, "Protein detection by optical shift of a resonant microcavity," *Applied Physics Letters*, vol. 80, no. 21, pp. 4057–4059, 2002.

[10] D. R. Smith, J. B. Pendry, and M. C. K. Wiltshire, "Metamaterials and negative refractive index," *Science*, vol. 305, no. 5685, pp. 788–792, 2004.

[11] L. Jiang, S. Zeng, Z. Xu, Q. Ouyang, D.-H. Zhang, P. H. J. Chong, P. Coquet, S. He, and K.-T. Yong, "Multifunctional hyperbolic nanogroove metasurface for submolecular detection," *Small*, vol. 13, no. 30, p. 1700600, 2017.

[12] H. Altug, D. Englund, and J. Vučković, "Ultrafast photonic crystal nanocavity laser," *Nature Physics*, vol. 2, pp. 484–488, Jul 2006.

[13] E. Optics, "Photonic-electronic integrated circuits," *Trending in optics*, September 2018.

[14] P. Lalanne, W. Yan, K. Vynck, C. Sauvan, and J.-P. Hugonin, "Light interaction with photonic and plasmonic resonances," *Laser & Photonics Reviews*, vol. 12, no. 5, p. 1700113, 2018.

[15] E. M. Purcell, H. C. Torrey, and R. V. Pound, "Resonance absorption by nuclear magnetic moments in a solid," *Phys. Rev.*, vol. 69, pp. 37–38, Jan 1946.

[16] M. R. Foreman, J. D. Swaim, and F. Vollmer, "Whispering gallery mode sensors," *Adv. Opt. Photon.*, vol. 7, pp. 168–240, Jun 2015.

[17] W. Chen, Ş. Kaya Özdemir, G. Zhao, J. Wiersig, and L. Yang, "Exceptional points enhance sensing in an optical microcavity," *Nature*, vol. 548, pp. 192–196, Aug 2017.

[18] A. M. Armani, R. P. Kulkarni, S. E. Fraser, R. C. Flagan, and K. J. Vahala, "Label-free, single-molecule detection with optical microcavities," *Science*, vol. 317, no. 5839, pp. 783–787, 2007.

[19] Y. nan Zhang, Y. Zhao, and R. qing Lv, "A review for optical sensors based on photonic crystal cavities," *Sensors and Actuators A: Physical*, vol. 233, pp. 374 – 389, 2015.

[20] P. Lalanne, S. Coudert, G. Duchateau, S. Dilhaire, and K. Vynck, "Structural slow waves: Parallels between photonic crystals and plasmonic waveguides," *ACS Photonics*, vol. 6, no. 1, pp. 4–17, 2019.

[21] H. Walther, B. T. H. Varcoe, B.-G. Englert, and T. Becker, "Cavity quantum electrodynamics," *Reports on Progress in Physics*, vol. 69, pp. 1325–1382, apr 2006.

[22] L. Novotny and B. Hecht, *Principles of Nano-Optics*, p. 378–418. Cambridge University Press, 2006.

[23] J. Homola, "Surface plasmon resonance sensors for detection of chemical and biological species," *Chemical Reviews*, vol. 108, no. 2, pp. 462–493, 2008. PMID: 18229953.

[24] E. Popov, "II light diffraction by relife gratings: A macroscopic and microscopic view," vol. 31 of *Progress in Optics*, pp. 139 – 187, Elsevier, 1993.

[25] S. Zeng, K.-T. Yong, I. Roy, X.-Q. Dinh, X. Yu, and F. Luan, "A review on functionalized gold nanoparticles for biosensing applications," *Plasmonics*, vol. 6, p. 491, Apr 2011.

[26] P. Kuppusamy, M. Y. Mashitah, G. P. Maniam, and N. Govindan, "Biosynthesized gold nanoparticle developed as a tool for detection of hcg hormone in pregnant women urine sample," *Asian Pacific Journal of Tropical Disease*, vol. 4, no. 3, p. 237, 2014.

[27] S. Jain, D. G. Hirst, and J. M. O'Sullivan, "Gold nanoparticles as novel agents for cancer therapy," *The British Journal of Radiology*, vol. 85, no. 1010, pp. 101–113, 2012. PMID: 22010024.

[28] L. Novotny, "Effective wavelength scaling for optical antennas," *Phys. Rev. Lett.*, vol. 98, p. 266802, Jun 2007.

[29] J. Zhang, Q. Ying, and Z. Ruan, "Time response of plasmonic spatial differentiators," *Opt. Lett.*, vol. 44, pp. 4511–4514, Sep 2019.

[30] W. Yan, R. Faggiani, and P. Lalanne, "Rigorous modal analysis of plasmonic nanoresonators," *Phys. Rev. B*, vol. 97, p. 205422, May 2018.

[31] P. T. Leung, S. Y. Liu, and K. Young, "Completeness and orthogonality of quasinormal modes in leaky optical cavities," *Phys. Rev. A*, vol. 49, pp. 3057–3067, Apr 1994.

[32] B. Vial, F. Zolla, A. Nicolet, and M. Commandré, "Quasimodal expansion of electromagnetic fields in open two-dimensional structures," *Phys. Rev. A*, vol. 89, p. 023829, Feb 2014.

[33] J. Zimmerling, L. Wei, P. Urbach, and R. Remis, "A lanczos model-order reduction technique to efficiently simulate electromagnetic wave propagation in dispersive media," *Journal of Computational Physics*, vol. 315, pp. 348 – 362, 2016.

[34] F. Zolla, A. Nicolet, and G. Demésy, "Photonics in highly dispersive media: the exact modal expansion," *Opt. Lett.*, vol. 43, pp. 5813–5816, Dec 2018.

[35] A. Gras, W. Yan, and P. Lalanne, "Quasinormal-mode analysis of grating spectra at fixed incidence angles," *Opt. Lett.*, vol. 44, pp. 3494–3497, Jul 2019.

[36] L. Zschiedrich, F. Binkowski, N. Nikolay, O. Benson, G. Kewes, and S. Burger, "Riesz-projection-based theory of light-matter interaction in dispersive nanoresonators," *Phys. Rev. A*, vol. 98, p. 043806, Oct 2018.

[37] C. Sauvan, J. P. Hugonin, I. S. Maksymov, and P. Lalanne, "Theory of the spontaneous optical emission of nanosize photonic and plasmon resonators," *Phys. Rev. Lett.*, vol. 110, p. 237401, Jun 2013.

[38] M. Kamandar Dezfouli and S. Hughes, "Regularized quasinormal modes for plasmonic resonators and open cavities," *Phys. Rev. B*, vol. 97, p. 115302, Mar 2018.

[39] R.-C. Ge and S. Hughes, "Design of an efficient single photon source from a metallic nanorod dimer: a quasi-normal mode finite-difference time-domain approach," *Opt. Lett.*, vol. 39, pp. 4235–4238, Jul 2014.

[40] M. Perrin, "Eigen-energy effects and non-orthogonality in the quasi-normal mode expansion of maxwell equations," *Opt. Express*, vol. 24, pp. 27137–27151, Nov 2016.

[41] C. Gigli, T. Wu, G. Marino, A. Borne, G. Leo, and P. Lalanne, "Quasinormal-mode non-hermitian modeling and design in nonlinear nano-optics," *ACS Photonics*, vol. 7, no. 5, pp. 1197–1205, 2020.

[42] T. Wu, A. Baron, P. Lalanne, and K. Vynck, "Intrinsic multipolar contents of nanoresonators for tailored scattering," *Phys. Rev. A*, vol. 101, p. 011803, Jan 2020.

[43] S. Franke, J. Ren, S. Hughes, and M. Richter, "Fluctuation-dissipation theorem and fundamental photon commutation relations in lossy nanostructures using quasinormal modes," *Phys. Rev. Research*, vol. 2, p. 033332, Aug 2020.

[44] R. Colom, R. McPhedran, B. Stout, and N. Bonod, "Modal expansion of the scattered field: Causality, nondivergence, and nonresonant contribution," *Phys. Rev. B*, vol. 98, p. 085418, Aug 2018.

[45] G. Rosolen, B. Maes, P. Y. Chen, and Y. Sivan, "Overcoming the bottleneck for quantum computations of complex nanophotonic structures: Purcell and förster resonant energy transfer calculations using a rigorous mode-hybridization method," *Phys. Rev. B*, vol. 101, p. 155401, Apr 2020.

[46] Q. Bai, M. Perrin, C. Sauvan, J.-P. Hugonin, and P. Lalanne, "Efficient and intuitive method for the analysis of light scattering by a resonant nanostructure," *Opt. Express*, vol. 21, pp. 27371–27382, Nov 2013.

[47] "MAN (Modal Analysis of Nanoresonators) open-source software." https://www.lp2n.institutoptique.fr/en/equipes-de-recherche-du-lp2n/light-complex-nanostructures.

[48] M. Duruflé, "Montjoie webpage." http://montjoie.gforge.inria.fr, 2018.

[49] V. Hernandez, J. E. Roman, and V. Vidal, "SLEPc: A scalable and flexible toolkit for the solution of eigenvalue problems," *ACM Trans. Math. Software*, vol. 31, no. 3, pp. 351–362, 2005.

[50] M. D. Truong, A. Nicolet, G. Demésy, and F. Zolla, "Continuous family of exact dispersive quasi-normal modal (dqnm) expansions for dispersive photonic structures," *Opt. Express*, vol. 28, pp. 29016–29032, Sep 2020.

[51] M. B. Doost, W. Langbein, and E. A. Muljarov, "Resonant-state expansion applied to three-dimensional open optical systems," *Phys. Rev. A*, vol. 90, p. 013834, Jul 2014.

[52] Y. Akahane, T. Asano, B.-S. Song, and S. Noda, "High-q photonic nanocavity in a two-dimensional photonic crystal," *Nature*, vol. 425, pp. 944–947, Oct 2003.

[53] J. Homola, S. S. Yee, and G. Gauglitz, "Surface plasmon resonance sensors: review," *Sensors and Actuators B: Chemical*, vol. 54, no. 1, pp. 3 – 15, 1999.

[54] V. Giannini, A. I. Fernández-Domínguez, S. C. Heck, and S. A. Maier, "Plasmonic nanoantennas: Fundamentals and their use in controlling the radiative properties of nanoemitters," *Chemical Reviews*, vol. 111, no. 6, pp. 3888–3912, 2011. PMID: 21434605.

[55] M. Agio, "Optical antennas as nanoscale resonators," *Nanoscale*, vol. 4, pp. 692–706, 2012.

[56] A. J. Shields, "Semiconductor quantum light sources," *Nature Photonics*, vol. 1, pp. 215–223, Apr 2007.

[57] P. Lalanne, "Mode volume of electromagnetic resonators: let us try giving credit where it is due," 2020.

[58] R. Faggiani, A. Losquin, J. Yang, E. Mårsell, A. Mikkelsen, and P. Lalanne, "Modal analysis of the ultrafast dynamics of optical nanoresonators," *ACS Photonics*, vol. 4, no. 4, pp. 897–904, 2017.

[59] E. A. Muljarov and W. Langbein, "Resonant-state expansion of dispersive open optical systems: Creating gold from sand," *Phys. Rev. B*, vol. 93, p. 075417, Feb 2016.

[60] T. Wu, A. Baron, P. Lalanne, and K. Vynck, "Intrinsic multipolar contents of nanoresonators for tailored scattering," *Phys. Rev. A*, vol. 101, p. 011803(R), Jan 2020.

[61] C. Baum, "Emerging technology for transient and broad-band analysis and synthesis of antennas and scatterers," *Proceedings of the IEEE*, vol. 64, no. 11, pp. 1598–1616, 1976.

[62] R. Colom, R. McPhedran, B. Stout, and N. Bonod, "Modal expansion of the scattered field: Causality, nondivergence, and nonresonant contribution," *Phys. Rev. B*, vol. 98, p. 085418, Aug 2018.

[63] M. I. Abdelrahman and B. Gralak, "Completeness and divergence-free behavior of the quasi-normal modes using causality principle," *OSA Continuum*, vol. 1, pp. 340–348, Oct 2018.

[64] P. Lalanne, W. Yan, A. Gras, C. Sauvan, J.-P. Hugonin, M. Besbes, G. Demésy, M. D. Truong, B. Gralak, F. Zolla, A. Nicolet, F. Binkowski, L. Zschiedrich, S. Burger, J. Zimmerling, R. Remis, P. Urbach, H. T. Liu, and T. Weiss, "Quasinormal mode solvers for resonators with dispersive materials," *J. Opt. Soc. Am. A*, vol. 36, pp. 686–704, Apr 2019.

[65] M. Duruflé, *Intégration numérique et éléments finis d'ordre élevé appliqués aux équations de Maxwell en régime harmonique.* PhD thesis, Université Paris IX-Dauphine, 2006.

[66] E. Anderson, Z. Bai, C. Bischof, S. Blackford, J. Demmel, J. Dongarra, J. Du Croz, A. Greenbaum, S. Hammarling, A. McKenney, and D. Sorensen, *LAPACK Users' Guide*. Philadelphia, PA: Society for Industrial and Applied Mathematics, third ed., 1999.

[67] U. Fano, "The theory of anomalous diffraction gratings and of quasi-stationary waves on metallic surfaces (sommerfeld's waves)," *J. Opt. Soc. Am.*, vol. 31, pp. 213–222, Mar 1941.

[68] A. Hessel and A. A. Oliner, "A new theory of wood's anomalies on optical gratings," *Appl. Opt.*, vol. 4, pp. 1275–1297, Oct 1965.

[69] D.Maystre, *General study of grating anomalies*. Chichester, UK: Wiley, electromagnetic surface modes, a. d. boardman ed., 1982.

[70] "See the collection of original articles gathered in Selected papers on Diffractin Gratings, D. Maystre, ed., SPIE Milestone series, Vol. MS 83.," 1993.

[71] S. Collin, "Nanostructure arrays in free-space: optical properties and applications," *Rep Prog Phys*, vol. 77, p. 126402, Dec. 2014.

[72] B. Vial, G. Demésy, F. Zolla, A. Nicolet, M. Commandré, C. Hecquet, T. Begou, S. Tisserand, S. Gautier, and V. Sauget, "Resonant metamaterial absorbers for infrared spectral filtering: quasimodal analysis, design, fabrication, and characterization," *J. Opt. Soc. Am. B*, vol. 31, pp. 1339–1346, Jun 2014.

[73] T. Weiss, M. Mesch, M. Schäferling, H. Giessen, W. Langbein, and E. A. Muljarov, "From dark to bright: First-order perturbation theory with analytical mode normalization for plasmonic nanoantenna arrays applied to refractive index sensing," *Phys. Rev. Lett.*, vol. 116, p. 237401, Jun 2016.

[74] T. Weiss, M. Schäferling, H. Giessen, N. A. Gippius, S. G. Tikhodeev, W. Langbein, and E. A. Muljarov, "Analytical normalization of resonant states in photonic crystal slabs and periodic arrays of nanoantennas at oblique incidence," *Phys. Rev. B*, vol. 96, p. 045129, Jul 2017.

[75] M. G. Moharam, E. B. Grann, D. A. Pommet, and T. K. Gaylord, "Formulation for stable and efficient implementation of the rigorous coupled-wave analysis of binary gratings," *J. Opt. Soc. Am. A*, vol. 12, pp. 1068–1076, May 1995.

[76] A. L. Fehrembach, "Réseaux résonnants à bande interdite photonique, nouveaux filtres pour le D.W.D.M.," 2003.

[77] "COMSOL Multiphysics ®." www.comsol.com. COMSOL AB, Stockholm, Sweden.

[78] P. Yeh, *Optical waves in layered media*. Wiley, 2005.

[79] J. Yang, J.-P. Hugonin, and P. Lalanne, "Near-to-far field transformations for radiative and guided waves," *ACS Photonics*, vol. 3, no. 3, pp. 395–402, 2016.

[80] P. Lalanne and G. M. Morris, "Highly improved convergence of the coupled-wave method for tm polarization," *J. Opt. Soc. Am. A*, vol. 13, pp. 779–784, Apr 1996.

[81] G. Granet and B. Guizal, "Efficient implementation of the coupled-wave method for metallic lamellar gratings in tm polarization," *J. Opt. Soc. Am. A*, vol. 13, pp. 1019–1023, May 1996.

[82] J. Ren, S. Franke, A. Knorr, M. Richter, and S. Hughes, "Near-field to far-field transformations of optical quasinormal modes and efficient calculation of quantized quasinormal modes for open cavities and plasmonic resonators," *Phys. Rev. B*, vol. 101, p. 205402, May 2020.

[83] J. Zimmerling and R. Remis, "Modal analysis of photonic and plasmonic resonators," *Opt. Express*, vol. 28, pp. 20728–20737, Jul 2020.

[84] K. Nguyen, F. Treyssède, and C. Hazard, "Numerical modeling of three-dimensional open elastic waveguides combining semi-analytical finite element and perfectly matched layer methods," *Journal of Sound and Vibration*, vol. 344, pp. 158 – 178, 2015.

[85] W. Yan, P. Lalanne, and M. Qiu, "Shape deformation of nanoresonator: A quasinormal-mode perturbation theory," *Phys. Rev. Lett.*, vol. 125, p. 013901, Jul 2020.

[86] K. Cognee, *Hybridization of open photonic resonators*. PhD thesis, 2020. Thèse de doctorat dirigée par Lalanne, Philippe et Koenderink, Femius. Lasers, Matière et Nanosciences Bordeaux 2020.

[87] J. Yang, H. Giessen, and P. Lalanne, "Simple analytical expression for the peak-frequency shifts of plasmonic resonances for sensing," *Nano Letters*, vol. 15, no. 5, pp. 3439–3444, 2015. PMID: 25844813.

[88] L. N. Trefethen, *Approximation Theory and Approximation Practice (Other Titles in Applied Mathematics)*. USA: Society for Industrial and Applied Mathematics, 2012.

[89] W. M. Gentleman, "Implementing clenshaw-curtis quadrature, i methodology and experience," *Commun. ACM*, vol. 15, p. 337–342, May 1972.

[90] P. Jantsch, C. G. Webster, and G. Zhang, "On the Lebesgue constant of weighted Leja points for Lagrange interpolation on unbounded domains," *IMA Journal of Numerical Analysis*, vol. 39, pp. 1039–1057, 06 2018.

[91] J. F. Epperson, "On the Runge example," *The American Mathematical Monthly*, vol. 94, no. 4, pp. 329–341, 1987.

Acknowlegements

I hope you learned something while reading this thesis and if you skipped here out of curiosity, that's fine too. My only wish is that my work be of some use to somebody who will eventually come into contact with QNMs. It is with many sighs of relief that I am writing this section. It feels like the end of a long and tiring journey.

I'll be giving out my honest thanks to the numerous people that have helped me on this odyssey.

I'd like to extend a first round of gratitude to everyone I had the pleasure of working with during this experience as a PhD student at LP2N and at INRIA.

I'd first like to thank my advisor Philippe for his thoughtful direction throughout these 3 years. You take extremely rigorous care in your work and have always strived to bring the best quality work to the scientific community. Even though things haven't always been easy, I have learned a lot from you and owe you a debt of gratitude. I know, with certainty, that your future work will be useful and innovative and I'll certainly be curious enough to check what you produce in the coming years.

I like to thank my other advisor, Marc, with whom I worked very closely during those three years. I learned a lot of things from you during those three years and you've always been very knowledgeable and reliable and someone who always gave pertinent and helpful advice. It's been a pleasure working with you and I know you will be a invaluable member in any project you might find yourself a part of.

To Kevin C., I want to say that I'm happy you chose me as your paranymph and to be your friend. From our impassioned arguments about whatever topic on our way to get lunch to the way I criticize your appreciation for **certain movies**, I hope that you can tolerate my bad jokes for as long as you possibly can. I hope to meet you somewhere soon, so we can celebrate whatever we would need to at that time. Thank you for being a source of advice and support, both technical and moral, throughout these 3 years.

To Louis, I want to thank you for mentoring me at the very start of my tenure at LP2N. It was always nice seeing you both inside and outside of the lab and I want to thank you for your assistance, especially during the writing of the manuscript. Thank you for supporting me and for your help correcting the manuscript.

To Wei, thank you for your help and tutelage at the beginning of this thesis which was the groundwork of the whole endeavor. To Kévin V., thank you for always being a positive presence at the lab during those 3 years and for all the interesting conversations. Maxime, I hope you're finishing your thesis in good spirits as well. I had fun these last few years working with you. Tong, I'd like to thank you for your help these last two years. I hope your work on QNMs will

bear its bounty soon. Denis, thank you for your technical assistance in this last year that actually enabled the whole team to work comfortably from home. But I'm very grateful for the faith you gave me in my work. I hope this thesis will serve as a compendium of information that you will be able to use. Armel, thank you for giving me your perspective on things, be it physics or other things, and for the many pleasant conversations around the coffee machine. To Juliette and Hélène, thank you for making feel like a part of the team at Magique 3D. I wish I could have made a short trip to Pau so I could have presented my work to the rest of the team. I'd also like to thank all the other members of the ANR project Resonance, with whom I had the pleasure to interact during these three years. I'd also like to extend my sincere thanks to the the members of the administration of the LP2N and INRIA. A special mention goes to Stéphanie who helped me so much over these 3 years.

I'd like to extend my gratitude to my personal circle of family and friends in the next section. Honestly, I don't think I would have made it this far without them. First and foremost, I'd like to give my highest regards to my mother, father and sister who have relentlessly cheered me on throughout these three years and have been on the front lines the myriad times where I've needed to vent and complain about my life and work. I love you all.

Then comes my friends who have continued to support me over the years. Benjamin and Clémence, you've always welcomed with open arms into your home whenever I wanted to take a short break and you've always been able to take me out of whatever foul mood I'd just happen to be in. Adrien, you're always so much fun to be around and you're a very caring friend. I hope your thesis is wrapping us nicely as well. Nicolas, I hope I can see you soon again so we can have more stupid fun. Antoine, thank you for reminding me to think about what I've accomplished instead of what I've failed to do. It's kinda hard to get out of this negative mindset sometimes but you've allowed me to break free from that kind of thinking. Thank you for the moral support and being there when I needed someone to vent to. Thank you Loïc for the support during this whole period. Thank you Briseis for always being someone fun to talk to. Thank you Jess for always checking up on me and hanging out with me. Sylvain, thank you for being an excellent person to have around for a conference. Hope your thesis is also finishing nicely. Thank you Paul for always going along with my silly conversation topics and for generally being a similarly-cultured individual. And finally, thank you Killian for being someone I can talk to about my problems without worry. I hope you can count on me as well.

Without these people in my life, things would indeed be infinitely less fun and this journey would have simply been much less pleasant. And so once again, I say "Thank you". You're super special and that's why you're here with me. Honestly, it's a wonder you can even stand all the complaining I do. I've very grateful for your presence in my life.

I'd also like to thank the unnamed who have been cheering me on, to whom I want to say "がんばれ! We're all gonna make it!"

At the end of it all, I guess what I feel right now is a sort of relief and some sort of joy. I don't really know how to describe it but the single "あれから" by 大槻ケンヂと絶望少女達 that came out this year sums up my feelings from this past year quite well.

絶望それだけが
僕らに教えた
幸せの日々は
今ここにある
絶望それこそが
君に教えた
生きてればGood job

あれから僕らにも
いろいろあった
いろいろあったけど
生きてればGood job
あれからみんなにも
いろいろあった
元気ならGood
In any case, all I want to say is, if you're doing well, that's good.

Reconstruction des champs électromagnétiques avec les Modes Quasinormaux : une approche numérique

Résumé :

La réponse des résonateurs optiques ouverts suite à leur excitation peut se décrire par la superposition de leurs résonances intrinsèques, leurs modes quasinormaux (QNM), qui sont excités par un champ incident et qui s'atténuent exponentiellement dans le temps à cause de fuites d'énergie et l'absorption. Les QNMs sont les vecteurs propres des équations de Maxwell harmoniques et permettent d'obtenir plus d'informations sur la dynamique du résonateur. Cependant, la complexité de la modélisation des résonateurs et du calcul des modes amènent à l'utilisation d'outils numériques pour résoudre ces systèmes équations linéaires afin de trouver les modes. La discrétisation du problème et certaines méthodes utilisées pour vérifier les conditions d'onde sortantes se manifestent à travers des modes numériques qui complètent la base des QNMs et qui permettent à la superposition de modes de converger si un grand nombre de modes, physiques et numériques, sont pris en compte. Nous vérifions que les formules qui existent pour la méthode des champs auxiliaires appliquée aux QNMs ont une origine commune et produisent des résultats similaires. Nous calculons les modes de structures périodiques afin de reconstruire le champs sur un spectre fréquentiel large. Nous essayons de faire converger la superposition des QNMs en trouvant un moyen de classifier les modes et explorons ensuite la dépendance des modes à certains paramètres numériques. Nous faisons converger la reconstruction modale du champ avec peu de modes en interpolant.

Mots clés :

Nanophotonique, Interaction Matière-Rayonnement, Simulation numérique, Simulation électromagnétique, Résonance, Modes, QNM, Résonateur, Modes Quasinormaux

Reconstruction of Electromagnetic Fields with Quasinormal Modes: A Numerical Approach

Abstract :

The response of open optical resonators to excitation can be expressed as a superposition of their intrinsic resonances, their quasinormal modes (QNM), which are loaded by the driving field and decay exponentially in time due to power leakage or absorption. Quasinormal modes are the eigensolutions of the time-harmonic Maxwell's equations et complex eigenfrequencies and allow more physical insight to be brought into the analysis of resonator dynamics. However, due to the complexity in modeling the open resonators and computing their modes, numerical tools such as linear eigenmode solvers are frequently called upon. The numerical discretization of the problem and some of the methods used to satisfy boundary conditions manifest themselves in the form of numerical modes that bear no physical meaning but complete the QNM basis and allow it to converge if many modes are included in the expansion. We also verify that the multiple formulas that exist for the auxiliary-field formulation of the QNM expansion have a similar origin and produce the same results. We compute the modes of periodic resonator structures to reconstruct the spectra on a wide spectrum of frequencies. We try to make the expansion converge with the least amount of modes by finding a way to classify them then explore the dependence of the modes on numerical parameters. Finally, we devised a way to obtain convergent results with few modes by interpolating from a few real frequency computations.

Keywords : Nanophotonics, Light-matter interaction, Numerical Simulation, Computational Electromagnetics, Resonance, Modes, Quasinormal Modes, QNM, Resonator

---

Unité de recherche

LP2N, CRNS UMR 5298, Institut d'Optique d'Aquitaine, Rue François Mitterrand CS3000, 33400 Talence Cedex, France

Magique3D, CNRS UMR 5212, Inria Bordeaux Sud-Ouest, 200 Av. de la Vieille Tour, 33405 Talence